Investigations on the Localized Surface Plasmon Resonances of Nickel Sulfide Nanostructures

Von der Naturwissenschaftlichen Fakultät der

Gottfried Wilhelm Leibniz Universität Hannover

zur Erlangung des Grades

Doktor der Naturwissenschaften (Dr. rer. nat.)

genehmigte Dissertation

von

Rasmus Himstedt, M. Sc.

2022

Referent: apl. Prof. Dr. Dirk Dorfs

Korreferent: apl. Prof. Dr. Armin Feldhoff

Korreferent: apl. Prof. Dr. Nikolai Gaponik

Tag der Promotion: 23.03.2022

Kurzzusammenfassung

Das Hauptthema dieser Arbeit war die Untersuchung der optischen Eigenschaften von Nanopartikeln bestehend aus metallischen Nickelsulfid-Phasen. Dazu wurden neue Synthesen entwickelt, um kolloidale Dispersionen von Ni_3S_2-, Ni_3S_4- und α-NiS-Nanostrukturen sowie Kern-Schale-Partikel mit Goldkernen zu erhalten. Diese Materialien zeigen auffällige Extinktionsbanden im sichtbaren Teil des elektromagnetischen Spektrums, die lokalisierten Oberflächenplasmonenresonanzen (LOPRs) zugeordnet werden konnten. Da das Feld der in diesem Spektralbereich aktiven plasmonischen Materialien auf Edelmetall-Nanopartikel beschränkt ist, wurden die neuartigen Nickelsulfid-Partikel hinsichtlich ihres molaren Extinktionskoeffizienten untersucht. Ein Vergleich der Ergebnisse mit denen der häufig verwendeten Goldnanokristalle zeigte, dass Ni_3S_2-Nanostrukturen sehr ähnliche Werte erreichen können, während die für ihre Synthese notwendigen Vorstufen deutlich günstiger sind als die der Edelmetalle. Darüber hinaus wurden hohle Nickelsulfid-Nanopartikel synthetisiert, um die Vorteile hohler Nanostrukturen im Hinblick auf Anwendungen als Nanosensoren nutzen zu können. Dies wurde über den nanoskaligen Kirkendall-Effekt ausgehend von Nickel-Nanopartikeln erreicht. Die erhaltenen hohlen Nickelsulfid-Nanopartikel zeigten eine deutlich schärfere LOPR-Extinktionsbande, was sie zu einem vielversprechenderen Material für die Sensorik macht. Darüber hinaus wurden α-NiS-und Au-α-NiS-Nanopartikel hinsichtlich ihres Metall-Isolator Übergangs und dessen Einfluss auf ihre LOPR untersucht. Es konnte gezeigt werden, dass die optische Dichte der kolloidalen Dispersionen durch Variation der Temperatur eingestellt werden kann, was sie zu einem temperaturschaltbaren plasmonischen Material macht.

Schlagworte: Lokalisierte Oberflächenplasmonenresonanz, hohle Nanopartikel, Nickelsulfid

Abstract

The main topic of this thesis was the examination of the optical properties of nanoparticles consisting of metallic nickel sulfide phases. For this, new syntheses to obtain various colloidal dispersions of Ni_3S_2, Ni_3S_4, and α-NiS nanostructures as well as core-shell particles with gold cores were developed. These materials all exhibit prominent absorbance features in the visible part of the electromagnetic spectrum which were confirmed to be caused by localized surface plasmon resonances (LSPRs). Since the field of plasmonic materials active in this spectral region is otherwise confined to noble metal nanoparticles, the novel nickel sulfide particles were evaluated with regard to their molar extinction coefficient. An analysis of the results compared to commonly used gold nanocrystals showed that Ni_3S_2 nanostructures could achieve very similar values while the necessary precursors for their synthesis are much less expensive than the respective noble metal precursors.

Furthermore, hollow nickel sulfide nanoparticles were synthesized to be able to profit from the advantages of hollow nanostructures in regards to applications as nanosensors. This was achieved *via* the nanoscale Kirkendall effect starting from nickel nanoparticles. The obtained hollow nickel sulfide nanoparticles showed a much sharper LSPR absorbance band making them a more promising material for sensorics.

Additionally, α-NiS and Au-α-NiS nanoparticles were investigated regarding their metal-insulator type phase transition and its influence on their LSPR. It could be shown, that the optical density of the colloidal dispersions can be tuned by varying the temperature, resulting in a temperature-switchable plasmonic material.

Keywords: Localized Surface Plasmon Resonance, Hollow Nanoparticles, Nickel Sulfide

Preface

The results presented in this thesis were obtained between 2016 and 2021 during my time as part of the research group of apl. Prof. Dr. Dirk Dorfs at the Institute of Physical Chemistry and Electrochemistry of the Leibniz Universität Hannover. The thesis consists of 4 publications, which were written by me as the first author. In the following, the contributions of each author are mentioned.

The first article, *Localized Surface Plasmon Resonances of Various Nickel Sulfide Nanostructures and Au-Ni₃S₂ Core-Shell Nanoparticles* (Chapter 2.2), was written by me. I also conducted all syntheses as well as the optical, x-ray diffraction (XRD), and dynamic light scattering (DLS) characterization of the Ni_3S_2 and $Au-Ni_3S_2$ structures. The shared first author Pascal Rusch performed the synthesis and initial optical, XRD, and DLS characterization of the Au nanocrystals and the Ni_3S_4 nanorods. Dr. Dominik Hinrichs did transmission electron microscopy (TEM) analysis of the samples and created the table of content (TOC) graphic for the manuscript while Dr. Torben Kodanek performed the selected area electron diffraction (SAED) measurements. Dr. Jannika Lauth conducted transient absorption spectroscopy (TAS) experiments, the results of which were discussed with Dr. Sachin Kinge and Prof. Dr. Laurens D. A. Siebbeles. Apl. Prof. Dr. Dirk Dorfs provided helpful advice and discussions.

The second article, *Extinction Coefficient of Plasmonic Nickel Sulfide Nanocrystals and Gold-Nickel Sulfide Core-Shell Nanoparticles* (Chapter 2.3), was written by me. I also performed the synthesis and characterization of the Ni_3S_2 and $Au-Ni_3S_2$ nanoparticles. The shared first author Dr. Dominik Hinrichs conducted the synthesis and characterization of the Au nanocrystals. He also wrote the respective part of the

experimental section and did most of the TEM analysis. Apl. Prof. Dr. Dirk Dorfs provided helpful advice and discussions.

The third article, *Halide Ion Influence on the Formation of Nickel Nanoparticles and their Conversion into Hollow Nickel Phosphide and Sulphide Nanocrystals* (Chapter 3.2) was written by me. I also conducted all syntheses and characterizations except for the ones mentioned in the following. Dr. Dominik Hinrichs performed a fraction of the TEM and SAED analysis. Dr. Joachim Sann performed and analyzed the x-ray photoelectron spectroscopy (XPS) experiments while Dr. Anica Weller did the inductively-coupled plasma mass spectrometry (ICP-MS) measurements, which were discussed with Prof. Dr. Georg Steinhauser. Apl. Prof. Dr. Dirk Dorfs provided helpful advice and discussions.

The fourth article, *Nickel Sulfide Nanoparticles with Temperature-Switchable Plasmon Resonances* (Chapter 4.2), was written by me. I also performed all syntheses and characterizations except for the ones mentioned in the following. Dr. Dirk Baabe conducted the magnetic susceptibility experiments and also wrote the respective parts of the "methods" and "results & discussion" sections of the manuscript. Christoph Wesemann provided helpful discussions about the magnetic susceptibility results and worked on important side experiments which are not included in the manuscript. Patrick Bessel did a fraction of the TEM analysis, while Dr. Dominik Hinrichs synthesized and characterized the Au seed particles. Anja Schlosser performed additional TEM measurements and helped to create the TOC graphic. Prof. Dr. Nadja C. Bigall and apl. Prof. Dr. Dirk Dorfs provided helpful advice and discussions.

Acknowledgments

First of all, I want to thank my examiner and supervisor apl. Prof. Dr. Dirk Dorfs for giving me the opportunity to work on this subject in his research group and for his advice which was always very helpful. The great balance he established between providing me with challenging tasks and leaving me enough freedom to pursue my own ideas is something I really appreciated.

Furthermore, I am grateful to apl. Prof. Dr. Armin Feldhoff and apl. Prof. Dr. Nikolai Gaponik for investing their time in being the additional referees for this thesis as well as to Prof. Dr. Franz Renz for being the head of the board of examiners.

I would also like to thank all of my external collaboration partners who made it possible to achieve the shown scientific results and to publish them in this way. These are: Prof. Dr. Laurens D. A. Siebbeles, Prof. Dr. Georg Steinhauser, Prof. Dr. Nadja C. Bigall, Dr. Dirk Baabe, Dr. Joachim Sann, Dr. Jannika Lauth, Dr. Sachin Kinge, and Dr. Anica Weller.

Moreover, I am grateful to all the students who worked for me. These were: Tim Göpfert, Andreas Breuksch, Max Niemeyer, Patrick Bessel, Evelyn Becker, Jakob Schlenkrich, and Christoph Wesemann.

Additionally, I am thankful to Dr. Fritz Schulze-Wischeler and Dr. Dominik Hinrichs for teaching me how to use a transmission electron microscope as well as to Pascal Rusch for his extensive help with the temperature-dependent optical spectroscopy measurements.

Yvonne Gabbey-Uebe, Kerstin Janze, Christine Sabisch, Sigrid Guttner, and everyone from the PCI workshop have my gratitude for helping me with organizational or technical matters.

Table of Contents

1 Introduction

1.1 Motivation

Generally, particles with dimensions between 1-100 nm are considered nanoparticles.[1] This size domain is interesting and has been intensely investigated in the last decades since some material classes like semiconductors and metals show drastically different properties as nanomaterials when compared to their bulk form.[1–3]

In the case of nanoparticles consisting of materials displaying a large number of free charge carriers, there is an important change to their optical properties.[4,5] On the nanoscale, the free charge carriers of the particle can be collectively excited by light irradiation, leading to an oscillation of the charge carrier density.[5] This effect is called localized surface plasmon resonance (LSPR) and will be further elaborated upon in chapter 1.2.[4] In the past, plasmonic particles have been used by mankind to color glass structures such as drinking cups or church windows.[6] While the underlying physical and chemical causes for the obtained coloration were unknown to people in these cases, in the more recent past, since researchers were able to understand and explain the LSPR, several more applications for plasmonic nanoparticles have been discovered.[7–9] Today, they are used in sensing and bioimaging (*e.g.* in pregnancy or SARS-CoV-2 tests),[10–18] as optical antennas or waveguides,[19,20] in photovoltaic cells,[21,22] in photothermal therapy,[23–25] for plasmon-enhanced fluorescence (PEF),[15,26] as well as in surface-enhanced Raman spectroscopy (SERS).[27,28] Since these applications are almost exclusively based on the optical properties of the particles, the respective usefulness of a given plasmonic material depends a lot on the resonance frequency and therefore on the wavelength of the absorbed light. Here, the materials showing LSPRs differ

especially due to their free charge carrier density.[29] While the most intensely investigated and best known plasmonic materials are nanoparticle dispersions of the noble metals gold and silver, which show an LSPR in the visible part of the electromagnetic spectrum, semiconductors can also exhibit an LSPR which is then found at far longer wavelengths.[29] Degenerately doped semiconductors like some copper chalcogenides and tin-doped indium oxide (ITO) for example exhibit sufficient charge carrier densities, leading to LSPR maximum wavelengths in the near-infrared region of the electromagnetic spectrum.[29–35]

For most applications, especially in the case of sensorics, a resonance that is observable by the human eye is often preferable since additional systems or methods to alert the user to the reaction of the LSPR are unnecessary.[13,36] Because of this and their superior property relationship between conductivity and surface plasmon magnitude as well as due to the far greater knowledge about them and their chemical stability, nanoparticles consisting of noble metals are by far the most commonly used plasmonic materials.[37] However, they also have some obvious disadvantages, the most prominent of them being the high cost of the raw material or to be more precise – the cost of the precursors. It would therefore be important to find a less costly alternative that shows the same or similar optical properties and could therefore substitute the expensive noble metal nanoparticles in their applications. This is one of the main focuses of this thesis. The goal is to show that nanoparticles consisting of different metallic nickel sulfide phases can serve similar purposes when compared to noble metal nanoparticles since they show LSPRs with very similar resonance wavelengths and are additionally much cheaper in their synthesis. This will be the subject of chapter 2.

The optical properties of plasmonic nanostructures are furthermore dependent on their shape.[5] Especially hollow particles have been shown to exhibit very favorable

plasmonic properties for sensory applications.[38] Examples for this are a strongly tunable resonance wavelength as well as a high sensitivity of the LSPR maximum to changes in the particle surroundings.[39,40] Chapter 3 of this thesis will therefore focus on developing a way to obtain hollow nickel sulfide nanoparticles and to characterize their optical properties.

Lastly, employing nickel sulfide as plasmonic material allows the utilization of different special properties of some of its specific phases. α-NiS for example shows a metal-insulator type phase transition that drastically alters its electronic and optical properties when it is cooled below roughly -10 °C.[41] Using this, a novel temperature-switchable plasmonic material could be developed. This avenue will be explored in chapter 4 of this thesis.

1.2 The Localized Surface Plasmon Resonance (LSPR)

In this chapter, a few basic concepts about the movement of free charge carriers through conductive materials will be presented. Some of the shown models have been developed with the goal to describe the processes in bulk materials and need to be adapted in order to properly represent the behavior of free charge carriers in nanoparticles.

1.2.1 Theoretical Background

The Drude-Sommerfeld Model

The original purpose of this model, developed by Paul Drude in 1900, was to describe the charge transport in metals under an external electric field.[42] Here, the influence of the field on single electrons is examined. Unfortunately, the model assumes that all electrons in the metal are strongly coupled to each other and collectively take part in the charge transport of the material. This is not reflective of reality, as only the electrons close to the Fermi level are able to do that. To account for this, Arnold Sommerfeld improved the approach in 1933 by introducing quantum mechanics in the form of Fermi-Dirac statistics.[43] The thusly created Drude-Sommerfeld model can be used to describe the electrical conductivity of metals as well as their dielectric function which is needed in order to understand and predict the optical properties of the material. The conduction electrons are treated as an ideal electron gas and therefore as being able to move freely in relation to the fixed and positively charged cores of the metal atoms. Hence, interactions between electrons are neglected in this approach. The movement of a single electron in an alternating external electric field $E(t)$ can thus be described according to equation (1), where e corresponds to the elemental charge while m_{eff} denotes the effective mass of the electron and Γ a phenomenological damping constant which

represents the collision rate of the electron with other electrons as well as with lattice phonons and crystal defects.[5]

$$m_{\text{eff}} \frac{\partial^2 r}{\partial t^2} + m_{\text{eff}} \Gamma \frac{\partial r}{\partial t} = eE(t) \tag{1}$$

Translating the resulting oscillation to the whole electron gas consisting of n free charge carriers leads to a polarization of the metal, as the electrons are treated as independent of each other. Employing the respective motion equation of the ensemble, a term for the complex dielectric function $\varepsilon(\omega)$ (equation 2) of the material, depending on the frequency of the oscillation, can be derived (equation 3).[5]

$$\varepsilon(\omega) = \varepsilon_1(\omega) + i\varepsilon_2(\omega) \tag{2}$$

$$\varepsilon(\omega) = 1 - \frac{\omega_P^2}{\omega^2 + i\Gamma\omega} \tag{3}$$

Here, ε_1 represents the real part of the dielectric function corresponding to the polarization of the metal and ε_2 is the imaginary part connected to energy dissipation (equations 4 and 5, respectively) while ω_P denotes the Drude plasma frequency which can be described by equation 6. ε_0 represents the vacuum permittivity.[5]

$$\varepsilon_1(\omega) \approx 1 - \frac{\omega_P^2}{\omega^2} \tag{4}$$

$$\varepsilon_2(\omega) \approx 1 - \frac{\omega_P^2}{\omega^3}\Gamma \tag{5}$$

$$\omega_P = \sqrt{\frac{ne^2}{\varepsilon_0 m_{\text{eff}}}} \tag{6}$$

The Quasi-Static Approximation

As alluded to in chapter 1.1, a plasmon is an oscillation of the free charge carrier density in electrically conductive materials. There are volume plasmons and also surface plasmons, which can occur on surfaces between dielectric materials and bulk conductors

like metals where they propagate over long distances.[44,45] In nanoparticles, this surface propagation is severely limited due to the small size of the particle. Here, the oscillation is therefore called localized surface plasmon resonance. Since the particle surface is strongly curved as opposed to the comparably flat surface of a bulk material, a strong restoring force is affecting the excited charge carriers, resulting in the observed resonance.[46] Furthermore, the curvature is enabling the excitation of the plasmon *via* direct light irradiation while the plasmons propagating on larger surfaces can only be excited when phase-matching techniques are employed.[46] The situation of such a particle in an oscillating electric field, as is the case upon its exposure to visible light, is schematically shown in Figure 1.
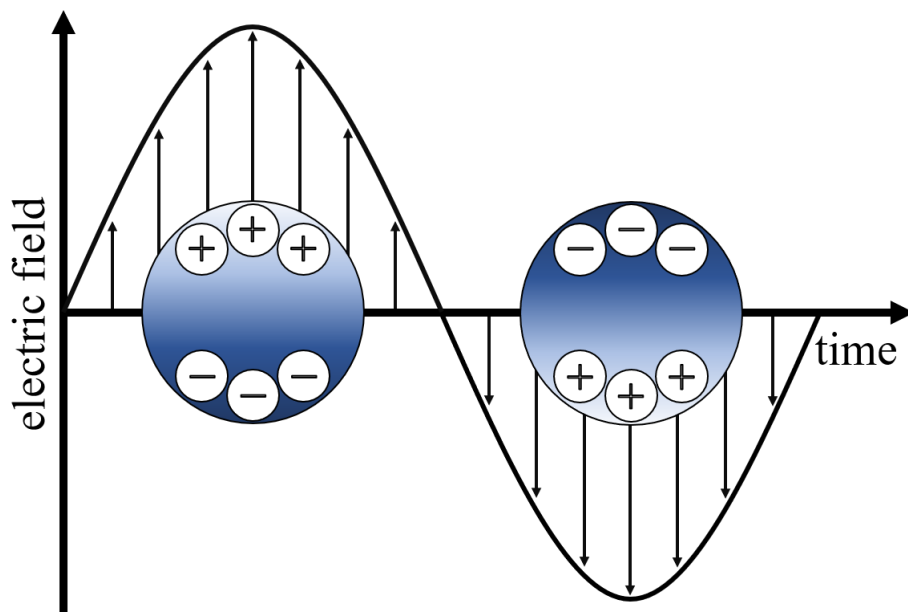
Figure 1. Schematic representation of an electrically conductive particle in an oscillating electric field. The free charge carriers of the material are excited by the field, leading to a polarization of the particle. Over time, an oscillation of the free charge carrier density results.

It can be observed that the oscillation of the charge carrier density leads to a polarization of the particle and hence to the formation of an electric dipole. In this state, the charge carriers are displaced in relation to the oppositely charged atomic cores

resulting in a strong coulombic attraction between them, which acts as a restoring force. Unfortunately, it is not trivial to describe this process mathematically since the electric field is not constant over the whole volume of the particle, leading to retardation effects. Generally, it is therefore necessary to solve Maxwell's differential equations, named after their inventor James C. Maxwell.[47] However, if the particle radius r is much smaller than the incident wavelength λ ($r << \lambda$), which is the case for small nanoparticles in visible light, a constant field can be approximated to simplify the problem.[5,48] This approach is called the quasi-static approximation and is schematically presented in Figure 2.[46]
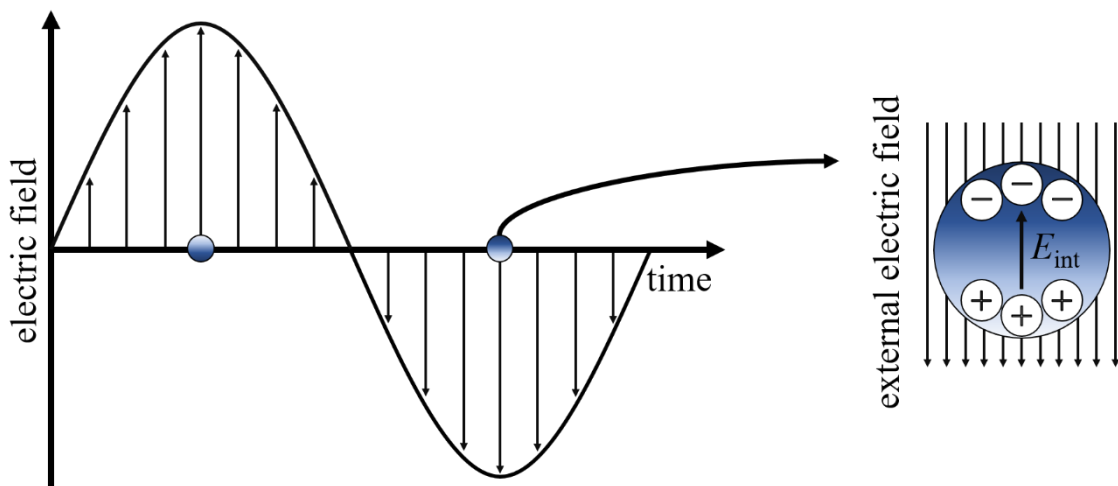
Figure 2. Schematic visualization of the quasi-static approximation. As opposed to the picture painted in Figure 1, the particle size needs to be much smaller than the wavelength of the electric field in order to assume an approximately constant field over the whole nanoparticle. The direction of the resulting internal field E_{int} inside the particle is exactly opposite to the one of the external field.

Using the quasi-static approximation, retardation effects can be neglected and an electro-static approach is possible.[46] To describe the optical response of a perfectly spherical nanoparticle, Laplace's equation (equation 7), developed in the 18th century by Pierre-Simon Laplace, can thus be solved without using Maxwell's equations. Here, ϕ denotes the electric potential of the applied electric field and ∇ the nabla operator.[46]

$$\nabla^2 \phi = 0 \tag{7}$$

From this, the electric field E can be calculated.[46]

$$E = -\nabla \phi \tag{8}$$

For the internal field E_{int}, this can be written as shown in equation 9. Here, ε_m represents the dielectric permittivity of the surrounding medium, $\varepsilon(\omega)$ the dielectric function of the plasmonic material, and E_0 the amplitude of the external electric field.[46]

$$E_{int} = \frac{3\varepsilon_m}{\varepsilon(\omega) + 2\varepsilon_m} E_0 \tag{9}$$

The polarizability α of the sphere can be calculated as presented in equation 10.[5]

$$\alpha = 4\pi\varepsilon_0 r^3 \frac{\varepsilon(\omega) - \varepsilon_m}{\varepsilon(\omega) + 2\varepsilon_m} \tag{10}$$

It is obvious that both E_{int} and α become very large, and therefore resonant, when $|\varepsilon(\omega)+2\varepsilon_m|$ becomes minimal. If the imaginary part of the dielectric function is sufficiently small ($\varepsilon_2(\omega) \ll 1$), the resonance condition can thus be described by equation 11.[5]

$$\varepsilon_1 = -2\varepsilon_m \tag{11}$$

Using this and combining the resonance condition with equation 4, the LSPR frequency ω_{LSPR} can be formulated.[5]

$$\omega_{LSPR} = \frac{\omega_p}{\sqrt{1 + 2\varepsilon_m}} \tag{12}$$

According to equation 12, the LSPR frequency and therefore also the wavelength of the absorbed or scattered light depends on the plasma frequency ω_p and the permittivity of the surrounding medium ε_m. As shown by equation 6, the plasma frequency is influenced by the number of free charge carriers n in the material and the effective mass m_{eff} of these carriers. With an increasing free charge carrier density or a decreasing m_{eff},

the LSPR frequency is shifted to larger frequencies and therefore to shorter wavelengths. In the case of ε_m, larger values lead to smaller LSPR frequencies and hence to longer wavelengths. The latter dependency is the main measuring principle of plasmonic sensors since a change in the particles dielectric surroundings can be detected *via* the change of the respective absorbance spectrum and thus also through the color of a nanoparticle dispersion or film.[10]

If the resonance condition is met, the absorption and scattering cross-sections of the examined spherical particle (C_{abs} and C_{sca}, respectively) become maximal due to the enhanced polarizability of the material. They can be described as shown in equations 13 and 14. In this case, k represents the wave vector.[46]

$$C_{abs} = 4\pi k r^3 \mathrm{Im}\left\{\frac{\varepsilon(\omega) - \varepsilon_m}{\varepsilon(\omega) + 2\varepsilon_m}\right\} \tag{13}$$

$$C_{sca} = \frac{8\pi}{3} k^4 r^6 \left|\frac{\varepsilon(\omega) - \varepsilon_m}{\varepsilon(\omega) + 2\varepsilon_m}\right|^2 \tag{14}$$

It can be seen that while the absorption of the particle scales with r^3 the scattering scales with r^6. Furthermore, the extinction or absorbance cross-section C_{ext} of the spheres is a sum of absorption and scattering processes and is therefore given by equation 15.[46]

$$C_{ext} = C_{abs} + C_{sca} \tag{15}$$

The Mie Theory

In 1908 Gustav Mie made great progress toward the understanding of the optical properties of dispersions containing noble metal nanoparticles. He solved Maxwell's equations for the case of spherical particles, explaining the observed colors by a combination of absorption and scattering processes of light.[47,49] To understand the optical properties of plasmonic nanoparticles which are not accurately described *via* the

quasi-static approximation due to their large dimensions, it is necessary to apply the more complex Mie theory. Fortunately, all the particles covered in this thesis are small enough for the approximation to be sufficient in this regard.

1.2.2 LSPR of Anisotropic Particles

So far, the LSPRs of perfectly isotropic, spherically-shaped nanoparticles have been discussed. In this case, there is only one resonance frequency that can be described as shown in chapter 1.2.1. However, if the examined particle is anisotropic this is not the case anymore. It has been established previously that the LSPR maximum occurs at a wavelength, where the polarizability of the nanoparticle is maximal. Yet, in an anisotropic particle, the polarizability along its different axes varies, resulting in the existence of multiple resonance frequencies and therefore plasmon modes.[5] In Figure 3, the example of a rod-shaped nanoparticle is schematically shown.
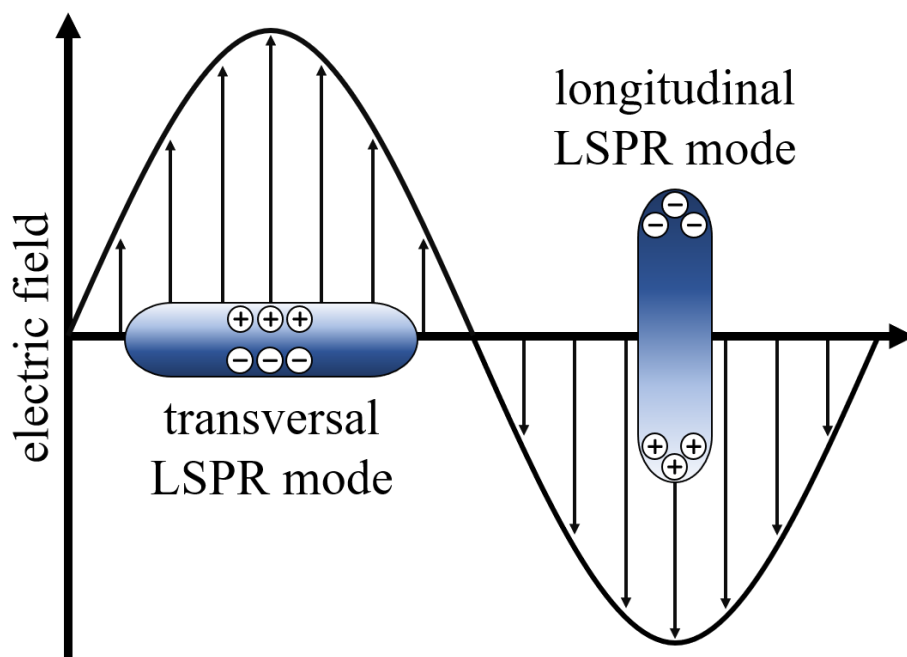

Figure 3. Schematic representation of an anisotropic, rod-shaped nanoparticle in an oscillating electric field. Depending on the orientation of the particle in relation to the incoming field, a polarization happens either along the transversal or the longitudinal axis of the rod. Both result in LSPRs with very different frequencies.

Depending on the orientation of the rod in relation to the external electric field, it can be polarized over its transversal or its longitudinal axis, leading to two resonance frequencies that differ greatly. Since the polarizability of the particle is larger and the coulombic restoring force smaller along its longitudinal axis, the respective plasmonic absorbance band is found at longer wavelengths than the one corresponding to the transversal plasmon mode.[5]

For the case of ellipsoid particles, the direction-dependent polarization α_i along the three principal axes (i = a, b, c) can be considered mathematically by introducing a geometrical depolarization factor L_i (equation 16), leading to equation 17. Here, V represents the volume of the nanoparticle.[5]

$$\sum L_i = L_a + L_b + L_c = 1 \tag{16}$$

$$\alpha_i = \varepsilon_0 \frac{\varepsilon(\omega) - \varepsilon_m}{\varepsilon_m + [\varepsilon(\omega) - \varepsilon_m]L_i} V \tag{17}$$

1.2.3 LSPR of Core-Shell Nanostructures

In core-shell nanostructures, the additional interface between the core and the shell is important to consider when describing the LSPR of either material or the particle as a whole. Plasmon modes, which tend to strongly couple with each other, can be excited in both parts of the nanoparticle depending on the chosen material combination, resulting in much more complicated absorbance spectra. For the sake of simplicity, a perfectly isotropic, spherical core-shell particle with only one shell is examined in the following. In this case, the quasi-static polarizability can be described according to equation 18 with ε_s representing the dielectric function and d the thickness of the shell, while ε_c denotes the dielectric function and r the radius of the core.[5]

$$\alpha = \varepsilon_0 \frac{(\varepsilon_s - \varepsilon_m)(\varepsilon_c + 2\varepsilon_s) + \left(\frac{r}{r+d}\right)^3 (\varepsilon_c - \varepsilon_s)(\varepsilon_m + 2\varepsilon_s)}{(\varepsilon_s + 2\varepsilon_m)(\varepsilon_c + 2\varepsilon_s) + \left(\frac{r}{r+d}\right)^3 (\varepsilon_c - \varepsilon_s)(2\varepsilon_s - \varepsilon_m)} \frac{4\pi}{3}(r+d)^3 \quad (18)$$

In practice, the formation of a thin shell around a plasmonic material initially leads to a broadening of its LSPR and possibly to the occurrence of multiple different plasmon modes. With an increasing shell thickness, this effect becomes less pronounced and the plasmon can be more accurately described as it has been in the previous chapters.[5] There are however significant differences visible in the respective absorbance spectra depending on the chosen material combination.

If a dielectric shell is grown onto a plasmonic core, the LSPR of the latter is only shifted toward shorter or longer wavelengths depending on the dielectric permittivity of the shell material. In the reversed case, where a plasmonic shell is grown onto a dielectric, the LSPR is split due to the two different plasmonic interfaces of the shell.[5] This will be discussed in more detail in chapter 1.2.4.

In the case of a plasmonic shell around a core which is likewise conductive, the LSPR of the core material is attenuated with an increasing shell thickness until the optical properties are finally almost exclusively dominated by the outer material. In practice, this means that for an example of a silver shell around a gold core, the LSPR of the nanoparticle is gradually and hypsochromically shifted from the LSPR wavelength of gold toward the one of silver with an increasing thickness of the shell. Conversely, in a silver-gold system, the silver LSPR shifts bathochromically until the spectral position of pure gold is reached.[50,51]

1.2.4 LSPR of Nanoshells

In essence, nanoshells are a special subcase of core-shell particles, where the core is either a dielectric material or entirely empty (as is the case for hollow nanoparticles).

As mentioned in chapter 1.2.3, here, the LSPR splits in two owing to the different surfaces along which a charge carrier density oscillation can take place, namely the outer surface of the sphere and the inner, cavity surface. The optical properties of such a nanostructure are then a result of a combination of these plasmon modes. This is schematically shown in Figure 4.
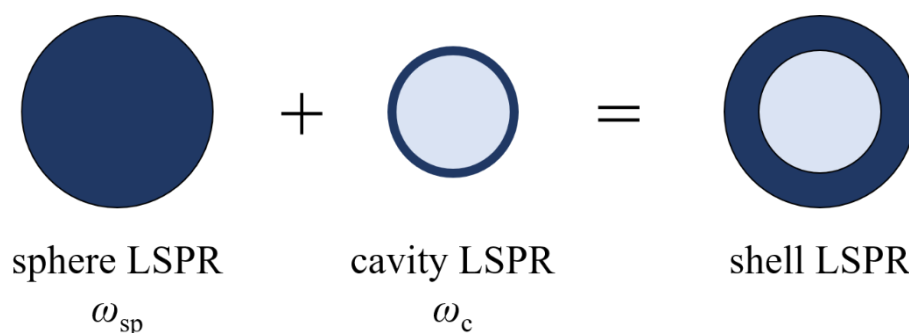
Figure 4. The LSPR of a hollow nanoparticle/nanoshell consists of a combination of the contributions of a "normal" sphere LSPR with the frequency ω_{sp} and an LSPR along the inner surface which is called cavity LSPR and has a frequency ω_c. Adapted by permission from the Materials Research Society, N. Halas, Playing with Plasmons: Tuning the Optical Resonant Properties of Metallic Nanoshells, *MRS Bulletin* **2005**, *30* (5), 362-367, Copyright 2005.[52]

The sphere and cavity LSPRs couple to each other which can be described using a hybridization model analogous to the combination of atomic orbitals to create molecular orbitals according to the molecular orbital theory.[53] Thus, from the coupling of the two plasmon modes two new combined modes arise. One of those is an energetically favorable "bonding" mode ω_- which is shifted toward lower energy and therefore a longer wavelength and one is an "anti-bonding" mode ω_+ which is accordingly energetically elevated, resulting in a hypsochromic shift of the corresponding absorbance band.[52]

In the case of the bonding mode, which is also called bright mode and couples strongly to the optical field, the polarization of the cavity and shell plasmon is coherent,

leading to a maximal polarization of the nanoshell. In the anti-bonding or dark plasmon mode, on the other hand, the polarization of the two surface plasmons is opposite to each other, resulting in a diminished total polarization and stronger restoring Coulomb forces.[52] The combination of sphere and cavity LSPR is schematically presented in Figure 5.
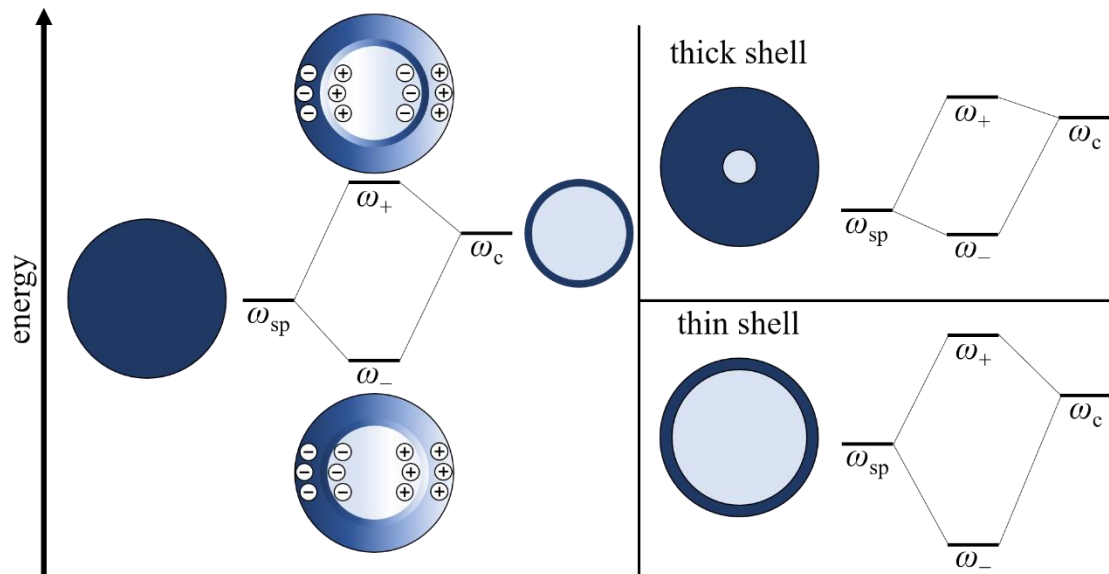

Figure 5. Schematic representation of the interaction between the sphere and cavity plasmon modes in nanoshells. Analogous to the molecular orbital theory, an energetically favorable "bright" or "bonding" mode ω_- with a maximally polarized particle and a dark or "anti-bonding" mode ω_+, where the oscillations of the sphere and cavity plasmon are directly opposed to each other, develop. The energetic positions of these two modes are furthermore dependent on the thickness of the nanoshell. With a decreasing shell thickness, the bonding plasmon mode which is coupling more strongly to the optical field is shifted toward lower energies while the anti-bonding mode is shifted in the opposite direction. Adapted by permission from the Materials Research Society, N. Halas, Playing with Plasmons: Tuning the Optical Resonant Properties of Metallic Nanoshells, *MRS Bulletin* **2005**, *30* (5), 362-367, Copyright 2005.[52]

As shown, the intensity of the plasmon coupling is strongly dependent on the thickness of the nanoshell and therefore on the proximity of the two conductive surfaces. If the dielectric cavity is small in relation to the plasmonic shell, the energetic shift of

the combined plasmon modes is small, while a thin shell around a large cavity leads to much larger differences.[52]

This can be used in order to tune the spectral position of an LSPR as well as its absorbance efficiency. Figure 6 shows the evolution of simulated optical absorbance spectra of spherical nanoparticles with a diameter of 40 nm consisting of a silica core and a gold shell. It can be observed that along with the expected bathochromic shift of the LSPR, its absorbance efficiency is strongly increased with a decreasing thickness of the nanoshell.[54]
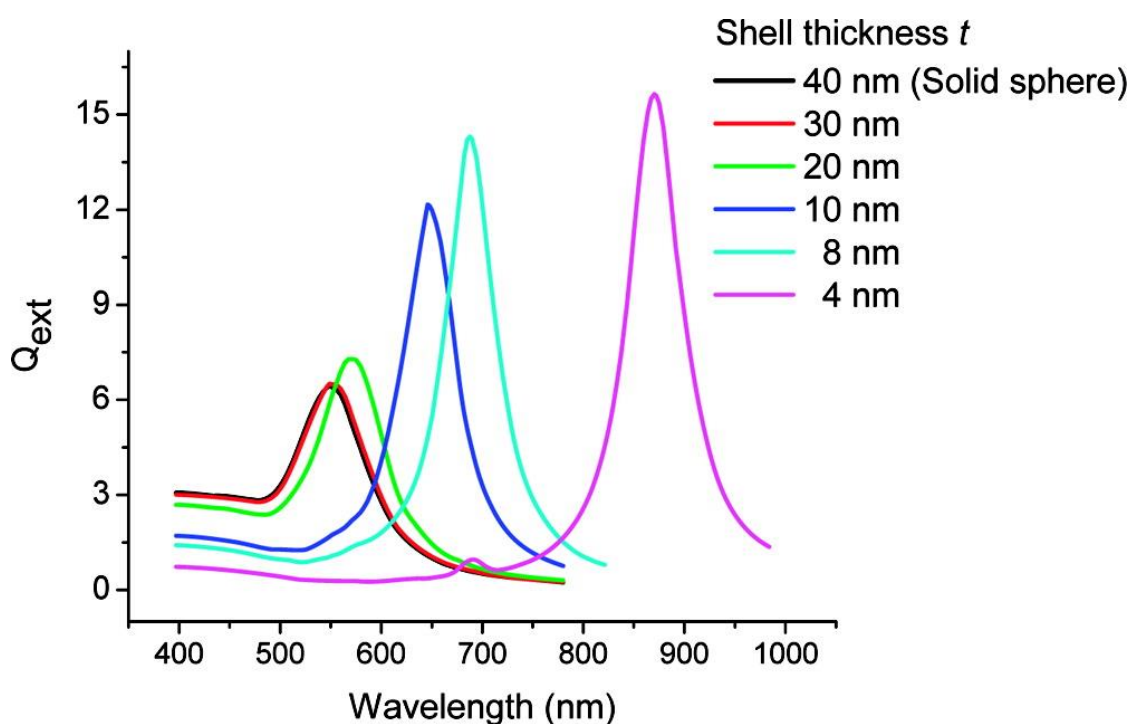
Figure 6. Extinction/absorbance efficiencies Q_{ext} of nanoparticles with a size of 40 nm consisting of a dielectric silica core and a plasmonic gold shell, calculated using the Mie theory. The total diameter of the particles is constant while the thickness of the shell is varied from 4 to 40 nm (solid Au sphere). With a decreasing shell thickness, the extinction efficiency of the LSPR increases and the resonance wavelength is bathochromically shifted. Reprinted with permission from *Nano Letters* **2007**, *7*, 9, 2854–2858. Copyright 2007 American Chemical Society.[54]

For this system, the spectral position λ of the LSPR absorbance band can be calculated using equation 19, where $\Delta\lambda = \lambda - \lambda_0$ denotes the spectral shift of the LSPR maximum in relation to the wavelength λ_0 of the maximum of a solid particle of the same size. [54]

$$\frac{\Delta\lambda}{\lambda_0} = 0.97e^{\left(\frac{-d/r}{0.18}\right)} \tag{19}$$

In comparison to the LSPR of solid nanoparticles, the hybridized plasmon modes of nanoshells are much more sensitive to changes in their dielectric environment due to a stronger plasmonic field on their surface which is a direct result of the coupling between the plasmons along the two interfaces.[38] For instance, hollow gold nanospheres can show a sensitivity factor that is about 4-6 times larger than that of similarly sized solid spheres.[38,39] Because of this, hollow plasmonic nanoparticles are more interesting for usage in sensorics while their larger surface-to-volume ratio also makes them superior candidates for applications in catalysis when compared to solid particles.[38]

1.3 Nanoparticle Synthesis

In this chapter, the most common wet chemistry methods to obtain nanoparticles will be described. A distinct focus will lie on the syntheses of core-shell structures and hollow particles as they are especially pertinent to the work presented in this thesis.

1.3.1 Direct Synthesis

Particles or structures with dimensions on the nanoscale (1-100 nm) can generally be obtained *via* two different approaches. The first, the so-called "top-down" method, is characterized by taking larger, bulk materials and breaking them up into smaller pieces using various means like laser ablation or ball milling.[55] The second route is the "bottom-up" approach, which relies on growing the nanoparticles starting from molecular precursors.[55] The latter is the general technique that is used to produce the particles presented in this thesis.

According to the still prevailing nucleation theory of Viktor K. LaMer and Robert H. Dinegar, it is necessary to separate the nucleation and growth phases of the synthesis in order to obtain monodisperse colloids using wet chemistry.[56] This can be achieved in different ways. One of those is the "hot-injection" method which was first developed in the group of Moungi Bawendi.[57] Here, the "cold" precursors are quickly injected into a reaction solution at high temperatures, resulting in a fast oversaturation of monomers and consequently in a burst of nucleation events. Then, the temperature is quickly decreasing and the monomer concentration is rapidly falling under the saturation limit. From this point onward, no further nucleation is possible and the remaining precursor is used solely to grow the existing particles.

Another approach to produce colloidal dispersions of nanoparticles is the "heat-up" method.[58] In this case, all precursors and other substances needed for the synthesis are

mixed at room temperature. Then, the temperature of the resulting reaction solution is increased in a controlled manner (usually very quickly) until a threshold is reached and monomers are formed rapidly. Like this, a large number of nuclei are simultaneously created. From this point onward, the synthesis progresses similarly to the way described in the case of the hot-injection.

After the nanoparticles have been formed and are grown to the desired size and shape, it is imperative to end the reaction and remove all the residual monomer and precursor concentrations since a colloidal solution of similarly sized small particles is generally not a thermodynamically favored state.[59] Over time and given the opportunity, smaller particles tend to dissolve leading to the further growth of their larger counterparts *via* the addition of the now available monomers.[59] This process is called Ostwald-ripening since it was discovered by Wilhelm Ostwald in the eighteen-nineties.[60]

In this thesis, both the hot-injection and the heat-up approach are used to produce different nickel sulfide nanoparticles. In the literature, there are existing synthesis procedures to obtain nanoparticles of various nickel sulfide phases such as Ni_3S_2, Ni_9S_8, α-NiS, β-NiS, Ni_3S_4, and NiS_2.[61–67] However, the quality of the products is often very low regarding their size distribution and phase purity. So far, only the β-NiS and Ni_3S_4 phases can be produced with a high degree of control over the particle shape and monodispersity.[68–70] β-NiS can be synthesized in the form of nanoprisms and nanorods while in the case of Ni_3S_4, elongated nanoprisms and nanopyramids can be reliably obtained.[68,70] Yet, prior to this thesis, the optical properties of metallic nickel sulfide nanoparticles have not been investigated regarding a possible occurrence of an LSPR.

1.3.2 Core-Shell Synthesis

Unlike the methods described in chapter 1.3.1, the bottom-up synthesis routes to obtain core-shell nanoparticles are generally two-step procedures.[71] They can, however, also be divided into two kinds of approaches. Firstly, the particle shells can be grown *in-situ* directly after the formation of the cores in a one-pot synthesis.[72–75] Secondly, the core particles can be produced in a completely separate step after which they are cleaned up and stored or potentially functionalized before further usage.[76,77] Then, they are introduced as seed particles in a subsequent coating procedure.

One of the main goals of core-shell syntheses is always the suppression of primary nucleation events of the shell material which is why the respective monomers should not be provided in too large concentrations.[71] Furthermore, the seed particles need to be optimized *via* suitable surface ligands to make secondary nucleation onto them energetically favorable.[71] The temperature is also an important parameter and should, if secondary nucleation is thermodynamically favorable compared to homogeneous nucleation, be lower than it would be in the case of a direct synthesis of nanoparticles consisting only of the shell material.[71]

As far as plasmonic core-shell systems are concerned, gold has been investigated intensely as core and also as shell material.[71] For instance, it can be used as a core for the growth of silver, cobalt, nickel, platinum as well as palladium shells or, alternatively, be coated onto iron, copper, and cobalt seed particles instead.[75,78–84] Besides gold-including plasmonic core-shell structures, there are also ways to obtain various different core-shell systems where nickel, cobalt, iron, and copper often serve as core material while the shell consists of comparably more noble metals like silver, copper, platinum, and palladium.[83–87]

Within this thesis, shells of different metallic nickel sulfide phases are grown onto previously synthesized gold core particles. To the best of the author's knowledge, there are no previous works on this subject.

1.3.3 Synthesis of Hollow Nanoparticles

In general, synthesis routes to obtain hollow nanostructures can be divided into two categories. On the one hand, there are templated syntheses where the material which is supposed to enclose a cavity is grown onto a soft- or hard-template which is then removed in a subsequent step.[88] This way, hollow structures consisting of various metal oxides, carbon as well as many other materials can be produced.[89–91]

On the other hand, there are template-free synthesis procedures that are more commonly used in the case of plasmonic nanoparticles and will therefore be explained in more detail here. Examples of this kind of route are the chemical etching of structures, galvanic replacement reactions, and the nanoscale Kirkendall effect.[92]

Chemical Etching

It is possible to obtain hollow nanostructures by selectively etching the particle interior.[92] This has been reported in the case of iron nanocubes which could be transformed into hollow nanoframes due to their insides being corroded by molten sodium salt which was generated *in-situ* during the synthesis.[93] Similarly, cubic cobalt nanoskeletons and palladium nanoboxes/nanocages could be produced *via* the controlled corrosion of cubic particle cores.[94,95] Further examples of hollow nanostructures which can be obtained by chemical etching are nanoparticles consisting of various transition metal oxides such as zinc, copper, iron, and manganese oxide.[96–98]

Galvanic Replacement Reactions

In the case of noble metals, galvanic replacement reactions are the most commonly used method in order to obtain hollow nanostructures.[99] For this, a material with a lower electrode potential, in most cases silver, is used to grow precursor particles which are then subsequently converted to a more noble metal like gold, palladium, or platinum through a galvanic reaction, resulting in hollow structures.[99] For instance, gold nanocages can be obtained from silver nanocubes since the less noble silver is oxidized and consequently dissolved in a redox reaction with gold ions, which are in turn reduced and deposited on the edges of the cubes.[100] Besides nanocages, nanoboxes, triangular nanorings, nanotubes (single- or multiple-walled), nanorattles, and nanoshells can be produced with this technique.[101–106] Platinum and palladium nanocages can be obtained in the same way starting from silver nanocubes.[107]

Instead of silver, other metals like cobalt can also be used as a precursor material. In this way, hollow gold, silver, platinum, palladium, or alloyed AuPt as well as CoPt nanostructures can be synthesized.[108–113] Here, the magnetic properties of cobalt particles and their tendency to form template structures like 1D chains can be used to obtain even more elaborate products.[113,114]

The Nanoscale Kirkendall Effect

In the 1940es, Ernest O. Kirkendall discovered that by heating copper-coated α-brass to 765 °C a directed transport of mass can be induced in the material due to different diffusion rates of copper and zinc atoms.[115,116] Generally, if two metals are in contact and the temperature is high enough, an alloy can be obtained. The resulting phase borders gradually move over time while voids are being formed owing to the respective diffusion coefficients of the metal atoms in the different materials. Here, the atomic

diffusion mechanism is based on the movement through lattice vacancies.[117] This accordingly named Kirkendall effect, which is likewise observed for other compounds besides pure metals, can also be employed to create cavities on the nanoscale, leading to the formation of hollow nanoparticles.[118–120] This is schematically depicted in Figure 7.
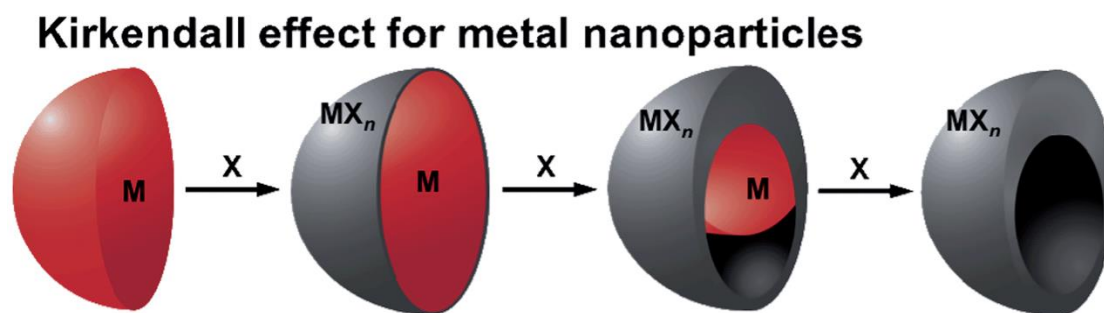

Figure 7. Schematic representation of the nanoscale Kirkendall effect in metal (M) nanoparticles. When a reactive substance X, which can be a pnictogen or chalcogen, is provided, a reaction $M + nX \rightarrow MX_n$ takes place and a shell around the metal core is formed. If the diffusion rate of X^- anions in the material MX_n is smaller than that of M^{n+} cations and if X is constantly added, a hollow nanostructure develops. Republished with permission of the Royal Society of Chemistry, from B. D. Anderson, J. B. Tracy, Nanoparticle Conversion Chemistry: Kirkendall Effect, Galvanic Exchange, and Anion Exchange, Nanoscale **2014**, *6* (21), 12195–12216, Copyright 2014; permission conveyed through Copyright Clearance Center, Inc.[119]

One of the most intensively investigated processes of this kind is the oxidation of particles consisting of transition metals like cobalt, nickel, and iron.[121–124] Here, upon exposing the particles to an oxygen source, a thin metal oxide layer is formed. To keep the reaction going, O^{2-} anions and/or M^{2+} cations then need to diffuse through said layer.[124,125]

The diffusion processes during the oxidation of a metal can be described with the Cabrera-Mott model which was developed by Nicolás Cabrera and Sir Nevill F. Mott in 1949 and is shown schematically in Figure 8.[126] Briefly, once a very thin metal oxide

layer has formed, electrons start to tunnel through the forming shell due to the creation of electronic surface states which are located below the Fermi level energetically. Hence, an electric field is generated. This field, in turn, drives the transport of metal cations and oxygen anions through the oxide.[119,126]
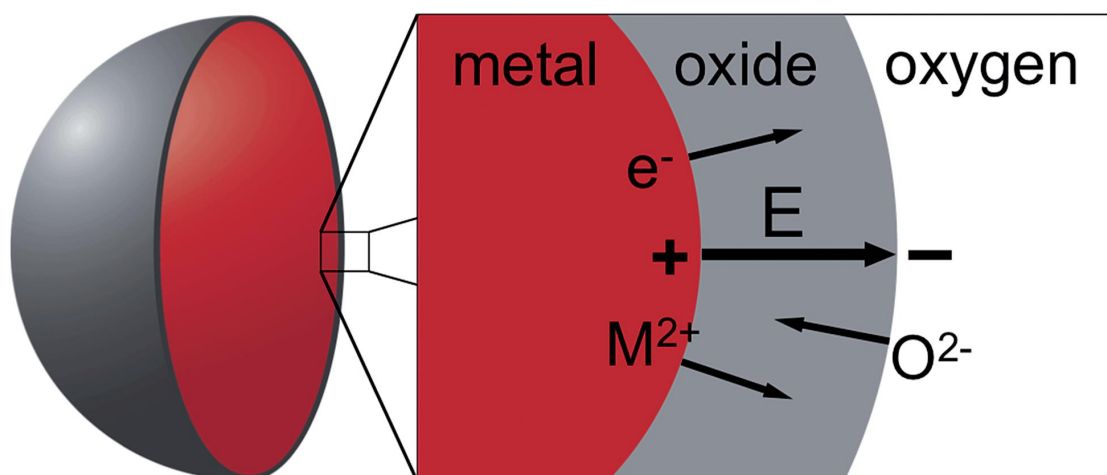

Figure 8. Schematic representation of the oxidization of a metal nanoparticle according to the Cabrera-Mott model. Through the initial surface reaction of metal and oxygen, a thin metal oxide film is formed. Subsequently, an electric field is generated in the metal oxide layer leading to the directed flow of ions and electrons. Republished with permission of the Royal Society of Chemistry, from B. D. Anderson, J. B. Tracy, Nanoparticle Conversion Chemistry: Kirkendall Effect, Galvanic Exchange, and Anion Exchange, Nanoscale **2014**, *6* (21), 12195–12216, Copyright 2014; permission conveyed through Copyright Clearance Center, Inc.[119]

The Cabrera-Mott theory was originally created to model the oxidization of bulk materials. Thus, in order to accurately apply it to nanoparticle systems some adaptations regarding the particles' geometry, volume changes during the process as well as their ligand coverage are needed.[127–129]

If the diffusion of the oxygen anions is faster than the one of the metal cations or the nanoparticles are very small, the whole particle is slowly converted to the metal oxide while the overall particle shape is usually preserved. Alternatively, core-shell structures

can be formed this way.[130–134] However, if the diffusion of the metal cations is quicker, which is often the case due to their smaller ionic radius, a cavity is developing and hollow nanostructures can be obtained.[119]

Besides oxides, many different materials can be produced and modeled this way.[92,119] For instance, hollow metal phosphide nanostructures can be obtained *via* the phosphidation of particles consisting of transition metals like iron, cobalt, nickel, gold, platinum, palladium, or rhodium with reactive phosphorus-containing substances like trioctylphosphine.[135–140] Other examples are hollow nanostructures of metal chalcogenides (sulfides, selenides, or tellurides) resulting from the conversion of cobalt, cadmium, lead, and silver nanoparticles or the transformation of copper and zinc oxide particles to copper selenide and zinc sulfide, respectively.[141–148]

Since the conversion chemistry of nickel nanoparticles *via* the nanoscale Kirkendall effect is very effective in the case of oxidization and phosphidation, experiments regarding the analogous synthesis of hollow nickel sulfide nanostructures were conducted as a part of this thesis. So far, this has only been shown on the microscale and not for actual nanoparticles.[149–155]

1.4 The Ni-S System

The Nickel-Sulfur system consists of a wide range of different compositions and phases. A phase diagram for temperatures above 0 °C is shown in Figure 9.
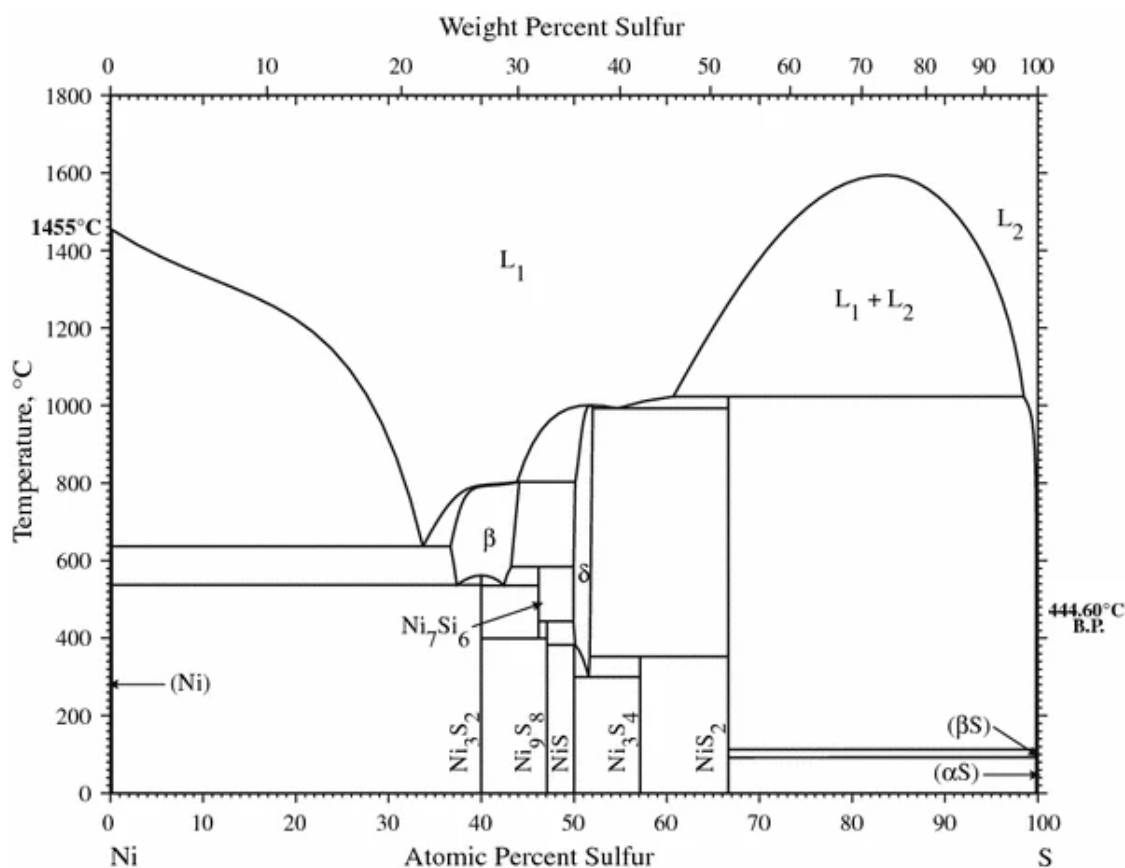

Figure 9. Phase diagram of the Ni-S system at atmospheric pressure. The bolded temperatures refer to the melting point of nickel and the boiling point of sulfur, respectively. Reprinted by permission from Springer Nature, H. Okamoto, Ni-S (Nickel-Sulfur) *Journal of Phase Equilibria and Diffusion* **2009**, *30*, 123, Copyright 2009.[156]

The most common phases, which also naturally occur as minerals, are heazlewoodite (Ni_3S_2), which has a rhombohedral crystal structure, trigonal millerite (β-NiS, denoted as NiS in Figure 9), as well as cubic polydymite (Ni_3S_4) and vaesite (NiS_2).[156–160] Due to the strong covalent nature of the Ni-S bonds in these structures and the large overlap between the Ni 3*d*- and S 3*p*-orbitals combined with Ni-Ni distances, which in some cases can be almost as small as in elemental nickel, all of these materials exhibit a large

density of states (DOS) at their respective Fermi level.[161] The overlap between the orbitals and therefore also the metallic behavior of the Ni-S phases decreases with a decreasing Ni:S ratio, resulting in all of these nickel sulfides apart from one exhibiting the properties of a metal. The exception to this is NiS_2, which is a Mott insulator (this will be explained in more detail in chapter 1.5).[161,162]

The phases relevant to this thesis are Ni_3S_2, Ni_3S_4, and the hexagonal α-NiS phase ($Ni_{1-x}S$, denoted as δ in Figure 9), which crystallizes in the NiAs structure type.[41,156,157] It can be observed that while Ni_3S_2 and Ni_3S_4 are thermodynamically stable at the used synthesis conditions (usually up to slightly over 200 °C) and at room temperature, this is not the case for α-NiS.[156,157] It is metastable and can therefore only be obtained at kinetically controlled synthesis conditions. However, if it is stabilized and subsequently cooled below roughly 265 K, a first-order phase transition, which is accompanied by a sudden and drastic change in electrical conductivity, can be triggered.[41,163] The nature of this and similar transitions will be further explained in chapter 1.5.

1.5 Metal-Insulator Transitions

It is a general convention that materials can be classified as metallic or semiconducting depending on the position of their respective Fermi level.[164–166] If it is positioned between classical bands, a band gap exists and the material is classified either as a semiconductor or even as an electrical insulator depending on the size of the gap. If the Fermi level is located inside a partially filled band/the conduction band, the material should show metallic properties. However, there are some examples of semiconducting/insulating materials which according to those rules should be a metal due to their band structure and DOS (*e.g.* NiS_2, see chapter 1.4).[167] This phenomenon, which was first explained by Sir Nevill F. Mott in 1949, is caused by electron-electron correlations which are neglected in the simpler energy-band model.[168] The underlying principle for these correlations is the fact that a significant amount of Coulomb repulsion exists between the individual electrons. The original model by Mott described the situation of a crystal consisting of atoms with one electron each at 0 K and proposed that there should be a discontinuous transition from insulating to metallic behavior depending on the interatomic distance.[169] This change is caused by the pairing energy which needs to be overcome when moving an electron from one atom to the next where it then has to share its orbital.

This idea was later expanded by Robert S. Knox, who described the situation of a semiconducting material whose bands are forced to overlap by changes to its stoichiometry or specific volume.[170] Here, it was reasoned that the change from semiconductor to metal would need to be discontinuous and therefore result in a sharp transition because small numbers of free electrons and holes would form excitons instead of behaving like an electron gas.[169,170]

The insulating state, which is usually antiferromagnetic, is termed Mott insulator, while the transition toward the metallic state is called a Mott transition.[169] During these sharp transitions there can also be changes to the structure of the material.

Further knowledge was added by John Hubbard who introduced the Hubbard energy U which represents the intra-atomic interaction energy of electrons.[171] He found out that a metal-insulator transition occurs when the ratio B/U of the corresponding bandwidth B to the Hubbard energy is equal to 1.15.[169] This means for strongly correlated materials with a large U compared to their respective bandwidth an insulating state is favored even though the classical band model would otherwise predict a metal. The resulting split bands are called the upper and lower Hubbard band, respectively.[169] A schematic picture of this can be seen in Figure 10.
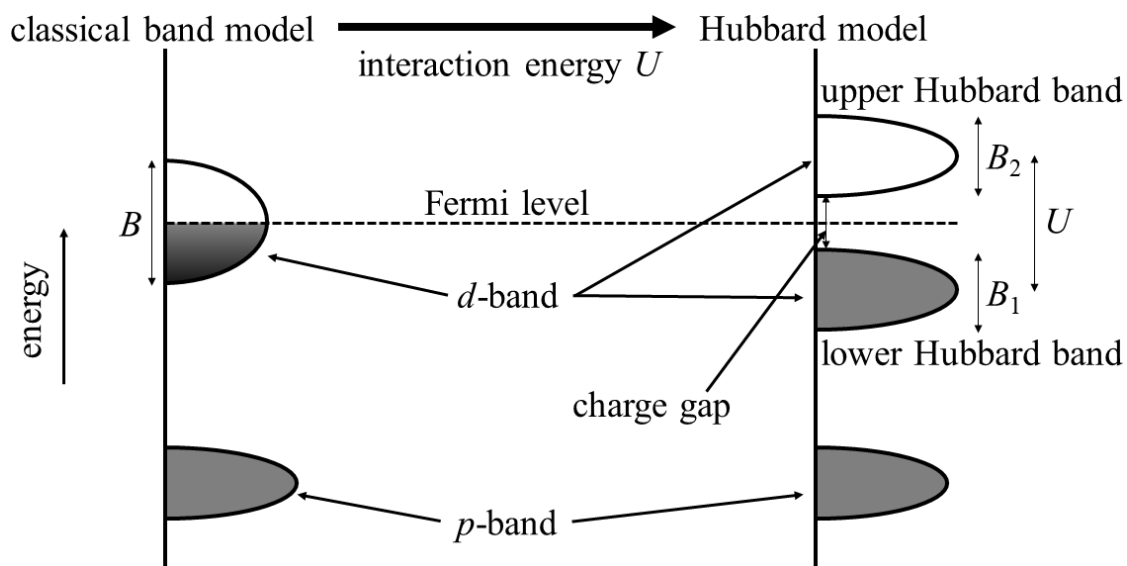

Figure 10. Intra-atomic electron-electron interaction induced splitting of the conduction band of a transition metal with a half-filled d-band into two Hubbard bands, leading to the semiconducting/insulating material properties of a Mott insulator. For the sake of simplicity, the scheme suggests that the bandwidths B_1 and B_2 of the two Hubbard bands are equal, which is not the case.[169] Adapted figure with permission from the American Physical Society, M. Imada, A. Fujimori, and Y. Tokura, *Rev. Mod. Phys.* **1998**, *70*, 1039, Copyright 1998.[172]

Metal-insulator transitions described by the Hubbard model are called Mott-Hubbard transitions and can be triggered by different means such as temperature, pressure, or compositional changes which alter the ratio B/U and therefore cause the two Hubbard bands to overlap.

Prominent examples of materials with metal-insulator transitions are transition metal chalcogenides such as NiO, VO_2, V_2O_3, and Ti_2O_3.[169] As mentioned previously (in chapter 1.4), NiS_2 is also a Mott insulator.[169] In this case, a Mott-Hubbard type transition can be induced by applying pressure to the material.[173] However, if a sufficient amount of sulfur atoms is replaced with selenium to form $NiS_{2-x}Se_x$, the transition also occurs due to the accompanying change in bandwidth, resulting in a metallic state at standard conditions.[169,174] This threshold is reached when x equals 0.5-0.6 at room temperature or 0.44 at 0 K.[174]

Another material from the Ni-S system which exhibits a similar transition is α-NiS ($Ni_{1-x}S$). Here, the transition can be triggered by cooling the material below roughly 265 K.[163,169] Furthermore, the transition temperature can be altered by changes to the composition of the material in the form of nickel deficiencies or doping with other transition metal atoms.[169,175,176] However, the antiferromagnetic low-temperature phase is not a classical Mott insulator in this case. Instead, even though its specific resistivity is increased by a factor of 100 in relation to the paramagnetic high-temperature phase, it still shows the electrical properties of a poorly conducting metal.[163] The changes to the structure, however, are minimal. The lattice parameters a and c expand by 0.3 and 1.0 %, respectively, while the cell volume of the NiAs-type structure is increased by 1.3 %.[41,163] The phase transition is of the first order, which means the corresponding changes to the material properties are likely accompanied by a hysteresis.[172]

The influence of a metal-insulator type transition on the LSPR of nanoparticles has to date only been investigated in the case of VO_2 films that show a plasmonic absorbance band in the near-infrared regime of the electromagnetic spectrum.[177–179] So far, there are no studies dealing with colloidally dispersed particles or resonances that are excitable by visible light. As a part of this thesis, α-NiS nanoparticles are synthesized and examined regarding their temperature-dependent optical properties in order to further investigate this subject.

1.6 References

(1)   Auffan, M.; Rose, J.; Bottero, J.-Y.; Lowry, G. V.; Jolivet, J.-P.; Wiesner, M. R. Towards a Definition of Inorganic Nanoparticles from an Environmental, Health and Safety Perspective. *Nat. Nanotechnol.* **2009**, *4* (10), 634–641.

(2)   Goesmann, H.; Feldmann, C. Nanoparticulate Functional Materials. *Angew. Chemie Int. Ed.* **2010**, *49* (8), 1362–1395.

(3)   Kovalenko, M. V.; Manna, L.; Cabot, A.; Hens, Z.; Talapin, D. V.; Kagan, C. R.; Klimov, V. I.; Rogach, A. L.; Reiss, P.; Milliron, D. J.; Guyot-Sionnnest, P.; Konstantatos, G.; Parak, W. J.; Hyeon, T.; Korgel, B. A.; Murray, C. B.; Heiss, W. Prospects of Nanoscience with Nanocrystals. *ACS Nano* **2015**, *9* (2), 1012–1057.

(4)   Baffou, G.; Quidant, R. Nanoplasmonics for Chemistry. *Chem. Soc. Rev.* **2014**, *43* (11), 3898.

(5)   Kreibig, U.; Vollmer, M. *Optical Properties of Metal Clusters*; Springer Series in Materials Science; Springer Berlin Heidelberg: Berlin, Heidelberg, 1995; Vol. 25.

(6)   Link, S.; El-Sayed, M. A. Optical Properties and Ultrafast Dynamics of Metallic Nanocrystals. *Annu. Rev. Phys. Chem.* **2003**, *54* (1), 331–366.

(7)   Faraday, M. X. The Bakerian Lecture. —Experimental Relations of Gold (and Other Metals) to Light. *Philos. Trans. R. Soc. London* **1857**, *147*, 145–181.

(8)   Maclagan, N. F. The Preparation and Use of Colloidal Gold Sols as Diagnostic Agents. *Br. J. Exp. Pathol.* **1946**, *27* (6), 369–377.

(9)   Macleod, C. E. A. Electric Metallic Colloids and their Therapeutical Applications. *Lancet* **1912**, *179* (4614), 322–323.

(10)   Sepúlveda, B.; Angelomé, P. C.; Lechuga, L. M.; Liz-Marzán, L. M. LSPR-Based Nanobiosensors. *Nano Today* **2009**, *4* (3), 244–251.

(11)   Rosi, N. L.; Mirkin, C. A. Nanostructures in Biodiagnostics. *Chem. Rev.* **2005**, *105* (4), 1547–1562.

(12)   Jain, P. K.; Huang, X.; El-Sayed, I. H.; El-Sayed, M. A. Noble Metals on the Nanoscale: Optical and Photothermal Properties and Some Applications in Imaging, Sensing, Biology, and Medicine. *Acc. Chem. Res.* **2008**, *41* (12), 1578–1586.

(13)   Ventura, B. Della; Cennamo, M.; Minopoli, A.; Campanile, R.; Censi, S. B.; Terracciano, D.; Portella, G.; Velotta, R. Colorimetric Test for Fast Detection of SARS-CoV-2 in Nasal and Throat Swabs. *ACS Sensors* **2020**, *5* (10), 3043–3048.

(14)   Anker, J. N.; Hall, W. P.; Lyandres, O.; Shah, N. C.; Zhao, J.; Van Duyne, R. P. Biosensing with Plasmonic Nanosensors. *Nat. Mater.* **2008**, *7* (6), 442–453.

(15)   Stewart, M. E.; Anderton, C. R.; Thompson, L. B.; Maria, J.; Gray, S. K.; Rogers, J. A.; Nuzzo, R. G. Nanostructured Plasmonic Sensors. *Chem. Rev.* **2008**, *108* (2), 494–521.

(16)   El-Sayed, I. H.; Huang, X.; El-Sayed, M. A. Surface Plasmon Resonance Scattering and Absorption of Anti-EGFR Antibody Conjugated Gold Nanoparticles in Cancer Diagnostics: Applications in Oral Cancer. *Nano Lett.* **2005**, *5* (5), 829–834.

(17)   Perezjuste, J.; Pastorizasantos, I.; Liz-Marzán, L.; Mulvaney, P. Gold Nanorods: Synthesis, Characterization and Applications. *Coord. Chem. Rev.* **2005**, *249* (17–18), 1870–1901.

(18)   Mesch, M.; Metzger, B.; Hentschel, M.; Giessen, H. Nonlinear Plasmonic Sensing. *Nano Lett.* **2016**, *16* (5), 3155–3159.

(19)   Mühlschlegel, A. P.; Eisler, H.; Martin, O. J. F.; Hecht, B.; Pohl, D. W. Resonant Optical Antennas. *Science* **2005**, *308* (5728), 1607–1609.

(20)   Krenn, J. R. Nanoparticle Waveguides: Watching Energy Transfer. *Nat. Mater.* **2003**, *2* (4), 210–211.

(21)   Chen, G.; Seo, J.; Yang, C.; Prasad, P. N. Nanochemistry and Nanomaterials for Photovoltaics. *Chem. Soc. Rev.* **2013**, *42* (21), 8304.

(22)   Kulkarni, A. P.; Noone, K. M.; Munechika, K.; Guyer, S. R.; Ginger, D. S. Plasmon-Enhanced Charge Carrier Generation in Organic Photovoltaic Films Using Silver Nanoprisms. *Nano Lett.* **2010**, *10* (4), 1501–1505.

(23)   Graham, E. G.; MacNeill, C. M.; Levi-Polyachenko, N. H. Review of Metal, Carbon and Polymer Nanoparticles for Infrared Photothermal Therapy. *Nano Life* **2013**, *03* (03), 1330002.

(24)   Pissuwan, D.; Valenzuela, S. M.; Killingsworth, M. C.; Xu, X.; Cortie, M. B. Targeted Destruction of Murine Macrophage Cells with Bioconjugated Gold Nanorods. *J. Nanoparticle Res.* **2007**, *9*, 1109–1124.

(25)   Smith, B. E.; Roder, P. B.; Zhou, X.; Pauzauskie, P. J. Nanoscale Materials for Hyperthermal Theranostics. *Nanoscale* **2015**, *7* (16), 7115–7126.

(26)   Sau, T. K.; Rogach, A. L.; Jäckel, F.; Klar, T. A.; Feldmann, J. Properties and Applications of Colloidal Nonspherical Noble Metal Nanoparticles. *Adv. Mater.* **2010**, *22* (16), 1805–1825.

(27)   Tian, Z. Q.; Ren, B.; Li, J. F.; Yang, Z. L. Expanding Generality of Surface-Enhanced Raman Spectroscopy with Borrowing SERS Activity Strategy. *Chem. Commun.* **2007**, No. 34, 3514–3534.

(28)   Halas, N. J.; Lal, S.; Chang, W.-S.; Link, S.; Nordlander, P. Plasmons in Strongly Coupled Metallic Nanostructures. *Chem. Rev.* **2011**, *111* (6), 3913–3961.

(29)   Luther, J. M.; Jain, P. K.; Ewers, T.; Alivisatos, A. P. Localized Surface Plasmon Resonances Arising from Free Carriers in Doped Quantum Dots. *Nat. Mater.* **2011**, *10* (5), 361–366.

(30)   Dorfs, D.; Härtling, T.; Miszta, K.; Bigall, N. C.; Kim, M. R.; Genovese, A.; Falqui, A.; Povia, M.; Manna, L. Reversible Tunability of the Near-Infrared Valence Band Plasmon Resonance in $Cu_{2-x}Se$ Nanocrystals. *J. Am. Chem. Soc.* **2011**, *133* (29), 11175–11180.

(31)   Kanehara, M.; Koike, H.; Yoshinaga, T.; Teranishi, T. Indium Tin Oxide

Nanoparticles with Compositionally Tunable Surface Plasmon Resonance Frequencies in the Near-IR Region. *J. Am. Chem. Soc.* **2009**, *131* (49), 17736–17737.

(32) Zhao, Y.; Burda, C. Development of Plasmonic Semiconductor Nanomaterials with Copper Chalcogenides for a Future with Sustainable Energy Materials. *Energy Environ. Sci.* **2012**, *5* (2), 5564–5576.

(33) van der Stam, W.; Berends, A. C.; de Mello Donega, C. Prospects of Colloidal Copper Chalcogenide Nanocrystals. *ChemPhysChem* **2016**, *17* (5), 559–581.

(34) Kriegel, I.; Jiang, C.; Rodríguez-Fernández, J.; Schaller, R. D.; Talapin, D. V.; Da Como, E.; Feldmann, J. Tuning the Excitonic and Plasmonic Properties of Copper Chalcogenide Nanocrystals. *J. Am. Chem. Soc.* **2012**, *134* (3), 1583–1590.

(35) Wolf, A.; Kodanek, T.; Dorfs, D. Tuning the LSPR in Copper Chalcogenide Nanoparticles by Cation Intercalation, Cation Exchange and Metal Growth. *Nanoscale* **2015**, 19519–19527.

(36) Tao, H.; Lin, Y.; Yan, J.; Di, J. A Plasmonic Mercury Sensor Based on Silver-Gold Alloy Nanoparticles Electrodeposited on Indium Tin Oxide Glass. *Electrochem. commun.* **2014**, *40*, 75–79.

(37) Strobbia, P.; Languirand, E.; Cullum, B. M. Recent Advances in Plasmonic Nanostructures for Sensing: A Review. *Opt. Eng.* **2015**, *54* (10), 100902.

(38) Mahmoud, M. A.; O'Neil, D.; El-Sayed, M. A. Hollow and Solid Metallic Nanoparticles in Sensing and in Nanocatalysis. *Chem. Mater.* **2014**, *26* (1), 44–58.

(39) Mahmoud, M. A.; El-Sayed, M. A. Gold Nanoframes: Very High Surface Plasmon Fields and Excellent near-Infrared Sensors. *J. Am. Chem. Soc.* **2010**, *132* (36), 12704–12710.

(40) Tu, M. H.; Sun, T.; Grattan, K. T. V. LSPR Optical Fibre Sensors Based on Hollow Gold Nanostructures. *Sensors Actuators, B Chem.* **2014**, *191*, 37–44.

(41) White, R. M.; Mott, N. F. The Metal-Non-Metal Transition in Nickel Sulphide (NiS). *Philos. Mag.* **1971**, *24* (190), 845–856.

(42) Drude, P. Zur Elektronentheorie Der Metalle. *Ann. Phys.* **1900**, *306* (3), 566–613.

(43) Sommerfeld, A.; Bethe, H. Elektronentheorie Der Metalle. In *Aufbau Der Zusammenhängenden Materie*; Springer Berlin Heidelberg: Berlin, Heidelberg, 1933; pp 333–622.

(44) Zhukovsky, S. V.; Kidwai, O.; Sipe, J. E. Physical Nature of Volume Plasmon Polaritons in Hyperbolic Metamaterials. *Opt. Express* **2013**, *21* (12), 14982.

(45) Gramotnev, D. K.; Bozhevolnyi, S. I. Plasmonics beyond the Diffraction Limit. *Nat. Photonics* **2010**, *4* (2), 83–91.

(46) Maier, S. A. *Plasmonics: Fundamentals and Applications*; Springer US: New York, NY, 2007; Vol. 677.

(47) Maxwell, J. C. VIII. A Dynamical Theory of the Electromagnetic Field. *Philos.*

Trans. R. Soc. London **1865**, *155*, 459–512.

(48) Bohren, C. F.; Huffman, D. R. *Absorption and Scattering of Light by Small Particles*; Wiley, 1998.

(49) Mie, G. Beiträge Zur Optik Trüber Medien, Speziell Kolloidaler Metallösungen. *Ann. Phys.* **1908**, *330* (3), 377–445.

(50) Cortie, M. B.; McDonagh, A. M. Synthesis and Optical Properties of Hybrid and Alloy Plasmonic Nanoparticles. *Chem. Rev.* **2011**, *111* (6), 3713–3735.

(51) Rodríguez-González, B.; Burrows, A.; Watanabe, M.; Kiely, C. J.; Liz Marzán, L. M. Multishell Bimetallic AuAg Nanoparticles: Synthesis, Structure and Optical Properties. *J. Mater. Chem.* **2005**, *15* (17), 1755.

(52) Halas, N. Playing with Plasmons: Tuning the Optical Resonant Properties of Metallic Nanoshells. *MRS Bull.* **2005**, *30* (5), 362–367.

(53) Prodan, E.; Nordlander, P. Structural Tunability of the Plasmon Resonances in Metallic Nanoshells. *Nano Lett.* **2003**, *3* (4), 543–547.

(54) Jain, P. K.; El-Sayed, M. a. Universal Scaling of Plasmon Coupling in Metal Nanostructures: Extension from Particle Pairs to Nanoshells. *Nano Lett.* **2007**, *7* (9), 2854–2858.

(55) *Introduction to Nanoscale Science and Technology*; Di Ventra, M., Evoy, S., Heflin, J. R., Eds.; Nanostructure Science and Technology; Springer US: Boston, MA, 2004.

(56) LaMer, V. K.; Dinegar, R. H. Theory, Production and Mechanism of Formation of Monodispersed Hydrosols. *J. Am. Chem. Soc.* **1950**, *72* (11), 4847–4854.

(57) Murray, C. B.; Norris, D. J.; Bawendi, M. G. Synthesis and Characterization of Nearly Monodisperse CdE (E = Sulfur, Selenium, Tellurium) Semiconductor Nanocrystallites. *J. Am. Chem. Soc.* **1993**, *115* (19), 8706–8715.

(58) van Embden, J.; Chesman, A. S. R.; Jasieniak, J. J. The Heat-Up Synthesis of Colloidal Nanocrystals. *Chem. Mater.* **2015**, *27* (7), 2246–2285.

(59) Yin, Y.; Alivisatos, A. P. Colloidal Nanocrystal Synthesis and the Organic–Inorganic Interface. *Nature* **2005**, *437* (7059), 664–670.

(60) Ostwald, W. Studien Über Die Bildung Und Umwandlung Fester Körper. *Zeitschrift für Phys. Chemie* **1897**, *22U* (1), 289–330.

(61) Karthikeyan, R.; Thangaraju, D.; Prakash, N.; Hayakawa, Y. Single-Step Synthesis and Catalytic Activity of Structure-Controlled Nickel Sulfide Nanoparticles. *CrystEngComm* **2015**, *17* (29), 5431–5439.

(62) Hollingsworth, N.; Roffey, A.; Islam, H.; Mercy, M.; Roldan, A.; Bras, W.; Wolthers, M.; Catlow, C. R. a.; Sankar, G.; Hogarth, G.; de Leeuw, N. H. The Active Nature of Primary Amines during the Thermal Decomposition of Nickel-Dithiocarbamates to Nickel-Sulfide Nanoparticles. *Chem. Mater.* **2014**, 141017153726008.

(63) Abdelhady, A. L.; Malik, M. A.; O'Brien, P.; Tuna, F. Nickel and Iron Sulfide Nanoparticles from Thiobiurets. *J. Phys. Chem. C* **2012**, *116* (3), 2253–2259.

(64) Du, H.; Liu, D.; Wu, H.; Xia, W.; Zhang, X.; Chen, Z.; Liu, Y.; Liu, H. Surface Modification of Nickel Sulfide Nanoparticles: Towards Stable Ultra-Dispersed Nanocatalysts for Residue Hydrocracking. *ChemCatChem* **2016**, *8* (8), 1543–1550.

(65) Lei, Z.; Zhang, W.; Li, B.; Guan, G.; Huang, X.; Peng, X.; Zou, R.; Hu, J. A Full-Spectrum-Absorption from Nickel Sulphide Nanoparticles for Efficient NIR-II Window Photothermal Therapy. *Nanoscale* **2019**, *11* (42), 20161–20170.

(66) Sobhani, A.; Salavati-Niasari, M. Synthesis, Characterization, Optical and Magnetic Properties of a Nickel Sulfide Series by Three Different Methods. *Superlattices Microstruct.* **2013**, *59*, 1–12.

(67) Roffey, A.; Hollingsworth, N.; Islam, H.-U.; Mercy, M.; Sankar, G.; Catlow, C. R. A.; Hogarth, G.; de Leeuw, N. H. Phase Control during the Synthesis of Nickel Sulfide Nanoparticles from Dithiocarbamate Precursors. *Nanoscale* **2016**, *8* (21), 11067–11075.

(68) Liu, Q.; Díaz, A.; Prosvirin, A.; Luo, Z.; Batteas, J. D. Shape-Controlled Synthesis of Nanopyramids and Nanoprisms of Nickel Sulfide (Ni 3 S 4). *Nanoscale* **2014**, *6* (15), 8935–8942.

(69) Ghezelbash, A.; Korgel, B. A. Nickel Sulfide and Copper Sulfide Nanocrystal Synthesis and Polymorphism. *Langmuir* **2005**, *21* (21), 9451–9456.

(70) Ghezelbash, A.; Sigman, M. B.; Korgel, B. A. Solventless Synthesis of Nickel Sulfide Nanorods and Triangular Nanoprisms. *Nano Lett.* **2004**, *4* (4), 537–542.

(71) Ghosh Chaudhuri, R.; Paria, S. Core/Shell Nanoparticles: Classes, Properties, Synthesis Mechanisms, Characterization, and Applications. *Chem. Rev.* **2012**, *112* (4), 2373–2433.

(72) Phadtare, S.; Kumar, A.; Vinod, V. P.; Dash, C.; Palaskar, D. V.; Rao, M.; Shukla, P. G.; Sivaram, S.; Sastry, M. Direct Assembly of Gold Nanoparticle "Shells" on Polyurethane Microsphere "Cores" and Their Application as Enzyme Immobilization Templates. *Chem. Mater.* **2003**, *15* (10), 1944–1949.

(73) Wang; Luo, J.; Fan, Q.; Suzuki, M.; Suzuki, I. S.; Engelhard, M. H.; Lin, Y.; Kim, N.; Wang, J. Q.; Zhong, C.-J. Monodispersed Core−Shell Fe₃O₄@Au Nanoparticles. *J. Phys. Chem. B* **2005**, *109* (46), 21593–21601.

(74) Kobayashi, Y.; Horie, M.; Konno, M.; Rodríguez-González, B.; Liz-Marzán, L. M. Preparation and Properties of Silica-Coated Cobalt Nanoparticles. *J. Phys. Chem. B* **2003**, *107* (30), 7420–7425.

(75) Bao, F.; Li, J.-F.; Ren, B.; Jian-LinYao; Gu, R.-A.; Tian, Z.-Q. Synthesis and Characterization of Au@Co and Au@Ni Core−Shell Nanoparticles and Their Applications in Surface-Enhanced Raman Spectroscopy. *J. Phys. Chem. C* **2008**, *112* (2), 345–350.

(76) Kim, H.; Achermann, M.; Balet, L. P.; Hollingsworth, J. A.; Klimov, V. I. Synthesis and Characterization of Co/CdSe Core/Shell Nanocomposites: Bifunctional Magnetic-Optical Nanocrystals. *J. Am. Chem. Soc.* **2005**, *127* (2), 544–546.

(77) Caruso, R. A.; Susha, A.; Caruso, F. Multilayered Titania, Silica, and Laponite

Nanoparticle Coatings on Polystyrene Colloidal Templates and Resulting Inorganic Hollow Spheres. *Chem. Mater.* **2001**, *13* (2), 400–409.

(78) Güzel, R.; Üstündağ, Z.; Ekşi, H.; Keskin, S.; Taner, B.; Durgun, Z. G.; Turan, A. A. İ.; Solak, A. O. Effect of Au and Au@Ag Core–Shell Nanoparticles on the SERS of Bridging Organic Molecules. *J. Colloid Interface Sci.* **2010**, *351* (1), 35–42.

(79) Kumar, S.; Zou, S. Electrooxidation of Carbon Monoxide and Methanol on Platinum-Overlayer-Coated Gold Nanoparticles: Effects of Film Thickness. *Langmuir* **2007**, *23* (13), 7365–7371.

(80) Li, J.-F.; Yang, Z.-L.; Ren, B.; Liu, G.-K.; Fang, P.-P.; Jiang, Y.-X.; Wu, D.-Y.; Tian, Z.-Q. Surface-Enhanced Raman Spectroscopy Using Gold-Core Platinum-Shell Nanoparticle Film Electrodes: Toward a Versatile Vibrational Strategy for Electrochemical Interfaces. *Langmuir* **2006**, *22* (25), 10372–10379.

(81) Lee, Y. W.; Kim, M.; Kim, Z. H.; Han, S. W. One-Step Synthesis of Au@Pd Core−Shell Nanooctahedron. *J. Am. Chem. Soc.* **2009**, *131* (47), 17036–17037.

(82) Hu, J.-W.; Li, J.-F.; Ren, B.; Wu, D.-Y.; Sun, S.-G.; Tian, Z.-Q. Palladium-Coated Gold Nanoparticles with a Controlled Shell Thickness Used as Surface-Enhanced Raman Scattering Substrate. *J. Phys. Chem. C* **2007**, *111* (3), 1105–1112.

(83) Lee, W.; Kim, M. G.; Choi, J.; Park, J.-I.; Ko, S. J.; Oh, S. J.; Cheon, J. Redox−Transmetalation Process as a Generalized Synthetic Strategy for Core−Shell Magnetic Nanoparticles. *J. Am. Chem. Soc.* **2005**, *127* (46), 16090–16097.

(84) Nadagouda, M. N.; Varma, R. S. A Greener Synthesis of Core (Fe, Cu)-Shell (Au, Pt, Pd, and Ag) Nanocrystals Using Aqueous Vitamin C. *Cryst. Growth Des.* **2007**, *7* (12), 2582–2587.

(85) Lu, L.; Zhang, W.; Wang, D.; Xu, X.; Miao, J.; Jiang, Y. Fe@Ag Core–Shell Nanoparticles with Both Sensitive Plasmonic Properties and Tunable Magnetism. *Mater. Lett.* **2010**, *64* (15), 1732–1734.

(86) Zhang, X.-B.; Yan, J.-M.; Han, S.; Shioyama, H.; Xu, Q. Magnetically Recyclable Fe@Pt Core−Shell Nanoparticles and Their Use as Electrocatalysts for Ammonia Borane Oxidation: The Role of Crystallinity of the Core. *J. Am. Chem. Soc.* **2009**, *131* (8), 2778–2779.

(87) Wang, G.; Wu, H.; Wexler, D.; Liu, H.; Savadogo, O. Ni@Pt Core–Shell Nanoparticles with Enhanced Catalytic Activity for Oxygen Reduction Reaction. *J. Alloys Compd.* **2010**, *503* (1), L1–L4.

(88) Soares, S. F.; Fernandes, T.; Daniel-da-Silva, A. L.; Trindade, T. The Controlled Synthesis of Complex Hollow Nanostructures and Prospective Applications. *Proc. R. Soc. A Math. Phys. Eng. Sci.* **2019**, *475* (2224), 20180677.

(89) Lou, X. W.; Yuan, C.; Archer, L. A. Shell-by-Shell Synthesis of Tin Oxide Hollow Colloids with Nanoarchitectured Walls: Cavity Size Tuning and Functionalization. *Small* **2007**, *3* (2), 261–265.

(90) Zhang, G.; Xia, B. Y.; Xiao, C.; Yu, L.; Wang, X.; Xie, Y.; Lou, X. W. D. General

Formation of Complex Tubular Nanostructures of Metal Oxides for the Oxygen Reduction Reaction and Lithium-Ion Batteries. *Angew. Chemie Int. Ed.* **2013**, *52* (33), 8643–8647.

(91) Liu, H.; Feng, Z.; Wang, J.; Diao, J.; Su, D. Synthesis of Hollow Carbon Nanostructures Using a ZnO Template Method. *New Carbon Mater.* **2016**, *31* (1), 87–91.

(92) An, K.; Hyeon, T. Synthesis and Biomedical Applications of Hollow Nanostructures. *Nano Today* **2009**, *4* (4), 359–373.

(93) Kim, D.; Park, J.; An, K.; Yang, N.-K.; Park, J.-G.; Hyeon, T. Synthesis of Hollow Iron Nanoframes. *J. Am. Chem. Soc.* **2007**, *129* (18), 5812–5813.

(94) Wang, X.; Fu, H.; Peng, A.; Zhai, T.; Ma, Y.; Yuan, F.; Yao, J. One-Pot Solution Synthesis of Cubic Cobalt Nanoskeletons. *Adv. Mater.* **2009**, *21* (16), 1636–1640.

(95) Xiong, Y.; Wiley, B.; Chen, J.; Li, Z.-Y.; Yin, Y.; Xia, Y. Corrosion-Based Synthesis of Single-Crystal Pd Nanoboxes and Nanocages and Their Surface Plasmon Properties. *Angew. Chemie Int. Ed.* **2005**, *44* (48), 7913–7917.

(96) Zeng, H.; Cai, W.; Liu, P.; Xu, X.; Zhou, H.; Klingshirn, C.; Kalt, H. ZnO-Based Hollow Nanoparticles by Selective Etching: Elimination and Reconstruction of Metal−Semiconductor Interface, Improvement of Blue Emission and Photocatalysis. *ACS Nano* **2008**, *2* (8), 1661–1670.

(97) Kuo, C.-H.; Huang, M. H. Fabrication of Truncated Rhombic Dodecahedral Cu_2O Nanocages and Nanoframes by Particle Aggregation and Acidic Etching. *J. Am. Chem. Soc.* **2008**, *130* (38), 12815–12820.

(98) An, K.; Kwon, S. G.; Park, M.; Na, H. Bin; Baik, S.-I.; Yu, J. H.; Kim, D.; Son, J. S.; Kim, Y. W.; Song, I. C.; Moon, W. K.; Park, H. M.; Hyeon, T. Synthesis of Uniform Hollow Oxide Nanoparticles through Nanoscale Acid Etching. *Nano Lett.* **2008**, *8* (12), 4252–4258.

(99) Lu, X.; Chen, J.; Skrabalak, S. E.; Xia, Y. Galvanic Replacement Reaction: A Simple and Powerful Route to Hollow and Porous Metal Nanostructures. *Proc. Inst. Mech. Eng. Part N J. Nanoeng. Nanosyst.* **2007**, *221* (1), 1–16.

(100) Skrabalak, S. E.; Au, L.; Li, X.; Xia, Y. Facile Synthesis of Ag Nanocubes and Au Nanocages. *Nat. Protoc.* **2007**, *2* (9), 2182–2190.

(101) Chen, J.; Saeki, F.; Wiley, B. J.; Cang, H.; Cobb, M. J.; Li, Z.-Y.; Au, L.; Zhang, H.; Kimmey, M. B.; Li, X.; Xia, Y. Gold Nanocages: Bioconjugation and Their Potential Use as Optical Imaging Contrast Agents. *Nano Lett.* **2005**, *5* (3), 473–477.

(102) Sun, Y.; Xia, Y. Triangular Nanoplates of Silver: Synthesis, Characterization, and Use as Sacrificial Templates For Generating Triangular Nanorings of Gold. *Adv. Mater.* **2003**, *15* (9), 695–699.

(103) Sun, Y.; Xia, Y. Mechanistic Study on the Replacement Reaction between Silver Nanostructures and Chloroauric Acid in Aqueous Medium. *J. Am. Chem. Soc.* **2004**, *126* (12), 3892–3901.

(104) Sun, Y.; Xia, Y. Multiple-Walled Nanotubes Made of Metals. *Adv. Mater.* **2004**,

16 (3), 264–268.

(105) Khalavka, Y.; Becker, J.; Sönnichsen, C. Synthesis of Rod-Shaped Gold Nanorattles with Improved Plasmon Sensitivity and Catalytic Activity. *J. Am. Chem. Soc.* **2009**, *131* (5), 1871–1875.

(106) Sun, Y.; Wiley, B.; Li, Z.-Y.; Xia, Y. Synthesis and Optical Properties of Nanorattles and Multiple-Walled Nanoshells/Nanotubes Made of Metal Alloys. *J. Am. Chem. Soc.* **2004**, *126* (30), 9399–9406.

(107) Chen, J.; Wiley, B.; McLellan, J.; Xiong, Y.; Li, Z.-Y.; Xia, Y. Optical Properties of Pd−Ag and Pt−Ag Nanoboxes Synthesized via Galvanic Replacement Reactions. *Nano Lett.* **2005**, *5* (10), 2058–2062.

(108) Liang, H.-P.; Wan, L.-J.; Bai, C.-L.; Jiang, L. Gold Hollow Nanospheres: Tunable Surface Plasmon Resonance Controlled by Interior-Cavity Sizes. *J. Phys. Chem. B* **2005**, *109* (16), 7795–7800.

(109) Liang, H. P.; Zhang, H. M.; Hu, J. S.; Guo, Y. G.; Wan, L. J.; Bai, C. L. Pt Hollow Nanospheres: Facile Synthesis and Enhanced Electrocatalysts. *Angew. Chemie - Int. Ed.* **2004**, *43* (12), 1540–1543.

(110) Chen, M.; Gao, L. Synthesis and Characterization of Ag Nanoshells by a Facile Sacrificial Template Route through in Situ Replacement Reaction. *Inorg. Chem.* **2006**, *45* (13), 5145–5149.

(111) Guo, S.; Fang, Y.; Dong, S.; Wang, E. High-Efficiency and Low-Cost Hybrid Nanomaterial as Enhancing Electrocatalyst: Spongelike Au/Pt Core/Shell Nanomaterial with Hollow Cavity. *J. Phys. Chem. C* **2007**, *111* (45), 17104–17109.

(112) Vasquez, Y.; Sra, A. K.; Schaak, R. E. One-Pot Synthesis of Hollow Superparamagnetic CoPt Nanospheres. *J. Am. Chem. Soc.* **2005**, *127* (36), 12504–12505.

(113) Liang, H.-P.; Guo, Y.-G.; Zhang, H.-M.; Hu, J.-S.; Wan, L.-J.; Bai, C.-L. Controllable AuPt Bimetallic Hollow Nanostructures. *Chem. Commun.* **2004**, No. 13, 1496.

(114) Zeng, J.; Huang, J.; Lu, W.; Wang, X.; Wang, B.; Zhang, S.; Hou, J. Necklace-like Noble-Metal Hollow Nanoparticle Chains: Synthesis and Tunable Optical Properties. *Adv. Mater.* **2007**, *19* (16), 2172–2176.

(115) Kirkendall, E. O. Diffusion of Zinc in Alpha Brass. *Trans. AIME* **1942**, *147*, 104–110.

(116) Smigelkas, A. D.; Kirkendall, E. O. Zinc Diffusion in Alpha Brass. *Trans. AIME* **1947**, *171*, 130–142.

(117) Paul, A. *The Kirkendall Effect in Solid State Diffusion*. Dissertation, Technical University of Eindhoven, Eindhoven, 2004.

(118) Wang, W.; Dahl, M.; Yin, Y. Hollow Nanocrystals through the Nanoscale Kirkendall Effect. *Chem. Mater.* **2013**, *25* (8), 1179–1189.

(119) Anderson, B. D.; Tracy, J. B. Nanoparticle Conversion Chemistry: Kirkendall Effect, Galvanic Exchange, and Anion Exchange. *Nanoscale* **2014**, *6* (21),

12195–12216.

(120) El Mel, A. A.; Nakamura, R.; Bittencourt, C. The Kirkendall Effect and Nanoscience: Hollow Nanospheres and Nanotubes. *Beilstein J. Nanotechnol.* **2015**, *6* (1), 1348–1361.

(121) Yang, Z.; Walls, M.; Lisiecki, I.; Pileni, M.-P. Unusual Effect of an Electron Beam on the Formation of Core/Shell (Co/CoO) Nanoparticles Differing by Their Crystalline Structures. *Chem. Mater.* **2013**, *25* (11), 2372–2377.

(122) Ha, D.-H.; Moreau, L. M.; Honrao, S.; Hennig, R. G.; Robinson, R. D. The Oxidation of Cobalt Nanoparticles into Kirkendall-Hollowed CoO and Co_3O_4: The Diffusion Mechanisms and Atomic Structural Transformations. *J. Phys. Chem. C* **2013**, *117* (27), 14303–14312.

(123) Johnston-Peck, A. C.; Wang, J.; Tracy, J. B. Synthesis and Structural and Magnetic Characterization of Ni(Core)/NiO(Shell) Nanoparticles. *ACS Nano* **2009**, *3* (5), 1077–1084.

(124) Peng, S.; Sun, S. Synthesis and Characterization of Monodisperse Hollow Fe_3O_4 Nanoparticles. *Angew. Chemie Int. Ed.* **2007**, *46* (22), 4155–4158.

(125) Brückman, A. The Mechanism of Transport of Matter through the Scales during Oxidation of Metals and Alloys. *Corros. Sci.* **1967**, *7* (1), 51–59.

(126) Cabrera, N.; Mott, N. F. Theory of the Oxidation of Metals. *Reports Prog. Phys.* **1949**, *12* (1), 308.

(127) Ermoline, A.; Dreizin, E. L. Equations for the Cabrera–Mott Kinetics of Oxidation for Spherical Nanoparticles. *Chem. Phys. Lett.* **2011**, *505* (1–3), 47–50.

(128) Zhdanov, V. P.; Kasemo, B. Cabrera–Mott Kinetics of Oxidation of Nm-Sized Metal Particles. *Chem. Phys. Lett.* **2008**, *452* (4–6), 285–288.

(129) Auge, A.; Weddemann, A.; Vogel, B.; Wittbracht, F.; Hütten, A. A Level Set Based Approach for Modeling Oxidation Processes of Ligand Stabilized Metallic Nanoparticles. *Appl. Phys. Lett.* **2010**, *96* (9), 093111.

(130) Railsback, J. G.; Johnston-Peck, A. C.; Wang, J.; Tracy, J. B. Size-Dependent Nanoscale Kirkendall Effect during the Oxidation of Nickel Nanoparticles. *ACS Nano* **2010**, *4* (4), 1913–1920.

(131) Yoon, T.-J.; Shao, H.; Weissleder, R.; Lee, H. Oxidation Kinetics and Magnetic Properties of Elemental Iron Nanoparticles. *Part. Part. Syst. Charact.* **2013**, *30* (8), 667–671.

(132) Tracy, J. B.; Weiss, D. N.; Dinega, D. P.; Bawendi, M. G. Exchange Biasing and Magnetic Properties of Partially and Fully Oxidized Colloidal Cobalt Nanoparticles. *Phys. Rev. B* **2005**, *72* (6), 064404.

(133) Verelst, M.; Ely, T. O.; Amiens, C.; Snoeck, E.; Lecante, P.; Mosset, A.; Respaud, M.; Broto, J. M.; Chaudret, B. Synthesis and Characterization of CoO, Co_3O_4, and Mixed Co/CoO Nanoparticules. *Chem. Mater.* **1999**, *11* (10), 2702–2708.

(134) Cabot, a.; Cabot, a.; Puntes, V. F.; Puntes, V. F.; Shevchenko, E.; Shevchenko,

E.; Yin, Y.; Yin, Y.; Balcells, L.; Balcells, L.; Marcus, M. a.; Marcus, M. a.; Hughes, S. M.; Hughes, S. M.; Alivisatos, a. P.; Alivisatos, a. P.; Others; Others. Vacancy Coalescence During Oxidation of Iron Nanoparticles - Supporting Information. *J. Am. Chem. Soc* **2007**, *129* (34), 10358–10360.

(135) Muthuswamy, E.; Kharel, P. R.; Lawes, G.; Brock, S. L. Control of Phase in Phosphide Nanoparticles Produced by Metal Nanoparticle Transformation: Fe$_2$P and FeP. *ACS Nano* **2009**, *3* (8), 2383–2393.

(136) Henkes, A. E.; Vasquez, Y.; Schaak, R. E. Converting Metals into Phosphides: A General Strategy for the Synthesis of Metal Phosphide Nanocrystals. *J. Am. Chem. Soc.* **2007**, *129* (7), 1896–1897.

(137) Henkes, A. E.; Schaak, R. E. Template-Assisted Synthesis of Shape-Controlled Rh$_2$P Nanocrystals. *Inorg. Chem.* **2008**, *47* (2), 671–677.

(138) Chiang, R.-K.; Chiang, R.-T. Formation of Hollow Ni$_2$P Nanoparticles Based on the Nanoscale Kirkendall Effect. *Inorg. Chem.* **2007**, *46* (2), 369–371.

(139) Henkes, A. E.; Schaak, R. E. Trioctylphosphine: A General Phosphorus Source for the Low-Temperature Conversion of Metals into Metal Phosphides. *Chem. Mater.* **2007**, *19* (17), 4234–4242.

(140) Ha, D.-H.; Moreau, L. M.; Bealing, C. R.; Zhang, H.; Hennig, R. G.; Robinson, R. D. The Structural Evolution and Diffusion during the Chemical Transformation from Cobalt to Cobalt Phosphide Nanoparticles. *J. Mater. Chem.* **2011**, *21* (31), 11498.

(141) Yin, Y.; Rioux, R. M.; Erdonmez, C. K.; Hughes, S.; Somorjai, G. A.; Alivisatos, A. P. Formation of Hollow Nanocrystals Through the Nanoscale Kirkendall Effect. *Science (80-.).* **2004**, *304* (5671), 711–714.

(142) Yin, Y.; Erdonmez, C. K.; Cabot, A.; Hughes, S.; Alivisatos, A. P. Colloidal Synthesis of Hollow Cobalt Sulfide Nanocrystals. *Adv. Funct. Mater.* **2006**, *16* (11), 1389–1399.

(143) Cabot, A.; Smith, R. K.; Yin, Y.; Zheng, H.; Reinhard, B. M.; Liu, H.; Alivisatos, A. P. Sulfidation of Cadmium at the Nanoscale. *ACS Nano* **2008**, *2* (7), 1452–1458.

(144) Tan, H.; Li, S.; Fan, W. Y. Core−Shell and Hollow Nanocrystal Formation via Small Molecule Surface Photodissociation; Ag@Ag$_2$Se as an Example. *J. Phys. Chem. B* **2006**, *110* (32), 15812–15816.

(145) Gao, J.; Zhang, B.; Zhang, X.; Xu, B. Magnetic-Dipolar-Interaction-Induced Self-Assembly Affords Wires of Hollow Nanocrystals of Cobalt Selenide. *Angew. Chemie Int. Ed.* **2006**, *45* (8), 1220–1223.

(146) Shao, H.-F.; Qian, X.-F.; Zhu, Z.-K. The Synthesis of ZnS Hollow Nanospheres with Nanoporous Shell. *J. Solid State Chem.* **2005**, *178* (11), 3522–3528.

(147) Cao, H.; Qian, X.; Zai, J.; Yin, J.; Zhu, Z. Conversion of Cu$_2$O Nanocrystals into Hollow Cu$_{2-x}$Se Nanocages with the Preservation of Morphologies. *Chem. Commun.* **2006**, No. 43, 4548–4550.

(148) Wang, Y.; Cai, L.; Xia, Y. Monodisperse Spherical Colloids of Pb and Their Use

as Chemical Templates to Produce Hollow Particles. *Adv. Mater.* **2005**, *17* (4), 473–477.

(149) Zhang, W.; Yan, X.; Tong, X.; Yang, J.; Miao, L.; Sun, Y.; Peng, L. Synthesis of Nickel Sulfide Monolayer Hollow Spheres Arrays as Cathode Materials for Alkaline Batteries. *Mater. Lett.* **2016**, *178*, 120–123.

(150) Wang, Y.; Zhu, Q.; Tao, L.; Su, X. Controlled-Synthesis of NiS Hierarchical Hollow Microspheres with Different Building Blocks and Their Application in Lithium Batteries. *J. Mater. Chem.* **2011**, *21* (25), 9248.

(151) Salavati-Niasari, M.; Banaiean-Monfared, G.; Emadi, H.; Enhessari, M. Synthesis and Characterization of Nickel Sulfide Nanoparticles via Cyclic Microwave Radiation. *Comptes Rendus Chim.* **2013**, *16* (10), 929–936.

(152) Chen, Z.; Wan, Z.; Yang, T.; Zhao, M.; Lv, X.; Wang, H.; Ren, X.; Mei, X. Preparation of Nickel Cobalt Sulfide Hollow Nanocolloids with Enhanced Electrochemical Property for Supercapacitors Application. *Sci. Rep.* **2016**, *6* (1), 25151.

(153) Yang, R.; Li, R.; Zhang, L.; Xu, Z.; Kang, Y.; Xue, P. Facile Synthesis of Hollow Mesoporous Nickel Sulfide Nanoparticles for Highly Efficient Combinatorial Photothermal–Chemotherapy of Cancer. *J. Mater. Chem. B* **2020**, *8* (34), 7766–7776.

(154) Yu, X.-Y.; Yu, L.; Wu, H. Bin; Lou, X. W. D. Formation of Nickel Sulfide Nanoframes from Metal-Organic Frameworks with Enhanced Pseudocapacitive and Electrocatalytic Properties. *Angew. Chemie Int. Ed.* **2015**, *54* (18), 5331–5335.

(155) Lynch, B. B.; Kelliher, A. P.; Anderson, B. D.; Japit, A.; Spencer, M. A.; Rizvi, M. H.; Sarac, M. F.; Augustyn, V.; Tracy, J. B. Sulfidation and Selenidation of Nickel Nanoparticles. *Carbon Energy* **2021**, *3* (4), 582–589.

(156) Okamoto, H. Ni-S (Nickel-Sulfur). *J. Phase Equilibria Diffus.* **2009**, *30* (1), 123.

(157) Kullerud, G.; Yund, R. A. The Ni-S System and Related Minerals. *J. Petrol.* **1962**, *3* (1), 126–175.

(158) Trahan, J.; Goodrich, R. G. Heat Capacity of Hexagonal NiS: Metal-Nonmetal Transition. *Phys. Rev. B* **1972**, *6* (1), 199–203.

(159) Grice, J. D.; Ferguson, R. B. Crystal Structure Refinement of Millerite (Beta - NiS). *Can. Mineral.* **1974**, *12* (4), 248–252.

(160) Rajamani, V.; Prewitt, C. T. The Crystal Structure of Millerite. *Can. Mineral.* **1974**, *12* (4), 253–257.

(161) Wang, J. H.; Cheng, Z.; Bŕdas, J. L.; Liu, M. Electronic and Vibrational Properties of Nickel Sulfides from First Principles. *J. Chem. Phys.* **2007**, *127* (21).

(162) Kautz, R. L.; Dresselhaus, M. S.; Adler, D.; Linz, A. Electrical and Optical Properties of NiS_2. *Phys. Rev. B* **1972**, *6* (6), 2078–2082.

(163) Panda, S. K.; Dasgupta, I.; Şaşıoğlu, E.; Blügel, S.; Sarma, D. D. NiS - An Unusual Self-Doped, Nearly Compensated Antiferromagnetic Metal. *Sci. Rep.*

2013, *3* (1), 2995.

(164) Wilson, A. H. The Theory of Electronic Semi-Conductors. *Proc. R. Soc. London. Ser. A, Contain. Pap. a Math. Phys. Character* **1931**, *133* (822), 458–491.

(165) Wilson, A. H. The Theory of Electronic Semi-Conductors. - II. *Proc. R. Soc. London. Ser. A, Contain. Pap. a Math. Phys. Character* **1931**, *134* (823), 277–287.

(166) Bloch, F. Über Die Quantenmechanik Der Elektronen in Kristallgittern. *Zeitschrift für Phys.* **1929**, *52* (7–8), 555–600.

(167) Tremel, W.; Seshadri, R.; Finckh, E. W. Metall Oder Nichtmetall? Das Ist Hier Die Frage!: Festkörperphysik Für Chemiker. *Chemie unserer Zeit* **2001**, *35* (1), 42–58.

(168) Mott, N. F. The Basis of the Electron Theory of Metals, with Special Reference to the Transition Metals. *Proc. Phys. Soc. Sect. A* **1949**, *62* (7), 416–422.

(169) Mott, N. F. *Metal-Insulator Transitions*, 2nd ed.; CRC Press: London, 1990.

(170) Knox, R. S. *Theory of Excitons*; Solid state physics: Supplement; Acad. Press, 1972.

(171) Hubbard, J. Electron Correlations in Narrow Energy Bands. *Proc. R. Soc. London. Ser. A. Math. Phys. Sci.* **1963**, *276* (1365), 238–257.

(172) Imada, M.; Fujimori, A.; Tokura, Y. Metal-Insulator Transitions. *Rev. Mod. Phys.* **1998**, *70* (4), 1039–1263.

(173) Mori, N.; Mitsui, T.; Yomo, S. High Pressure Effect on the Electrical Properties of NiS2. *Solid State Commun.* **1973**, *13* (8), 1083–1085.

(174) Schuster, C.; Gatti, M.; Rubio, A. Electronic and Magnetic Properties of NiS$_2$, NiSSe and NiSe$_2$ by a Combination of Theoretical Methods. *Eur. Phys. J. B* **2012**, *85* (9), 325.

(175) Sparks, J. T.; Komoto, T. Metal-to-Semiconductor Transition in Hexagonal NiS. *Rev. Mod. Phys.* **1968**, *40* (4), 752–754.

(176) Nakamura, M.; Fujimori, A.; Sacchi, M.; Fuggle, J. C.; Misu, A.; Mamori, T.; Tamura, H.; Matoba, M.; Anzai, S. Metal-Nonmetal Transition in NiS Induced by Fe and Co Substitution: X-Ray-Absorption Spectroscopic Study. *Phys. Rev. B* **1993**, *48* (23), 16942–16947.

(177) Nishikawa, K.; Kishida, Y.; Ito, K.; Tamura, S.; Takeda, Y. Near-Infrared Localized Surface Plasmon Resonance of Self-Growing W-Doped VO$_2$ Nanoparticles at Room Temperature. *Appl. Phys. Lett.* **2017**, *111* (19), 193102.

(178) Bercea, A. I.; Champeaux, C.; Constantinescu, C. D.; Dumas-Bouchiat, F. Vanadium Dioxide–Iridium Composite Development: Specific Near Infrared Surface Plasmon Resonance. *J. Compos. Sci.* **2021**, *5* (7), 193.

(179) Ke, Y.; Zhang, B.; Wang, T.; Zhong, Y.; Vu, T. D.; Wang, S.; Liu, Y.; Magdassi, S.; Ye, X.; Zhao, D.; Xiong, Q.; Sun, Z.; Long, Y. Manipulating Atomic Defects in Plasmonic Vanadium Dioxide for Superior Solar and Thermal Management. *Mater. Horizons* **2021**, *8* (6), 1700–1710.

2 Optical Properties of Different Nickel Sulfide Nanostructures

2.1 Summary

The results presented in chapter 2.2 represent the first investigation of the optical properties of nickel sulfide nanoparticles regarding the possible occurrence of a localized surface plasmon resonance. They show that in the case of particles consisting of the metallic phases Ni_3S_2 and Ni_3S_4 absorbance maxima in the visible regime of the electromagnetic spectrum can be found using optical spectroscopy. To confirm the plasmonic nature of these features, multiple experiments were conducted. The dependency of the LSPR maximum on the dielectric surroundings was investigated by changing the solvent of the particle dispersions. As expected for a plasmonic material, the maximum was bathochromically shifted with an increasing dielectric permittivity of the solvent. Additionally, novel Au-Ni_3S_2 core-shell nanostructures were synthesized. The LSPR maximum of these particles hypsochromically shifted from that of the Au cores toward the respective spectral position of pure Ni_3S_2 with an increasing shell thickness instead of bathochromically shifting the gold plasmon as it would be the case for most semiconducting shells grown onto gold cores. Furthermore, prismatic Ni_3S_4 nanorods with much broader absorbance features were examined. Since these particles were not colloidally stable over longer time spans, they tended to aggregate over time, resulting in a bathochromically shifted and broadened LSPR maximum due to plasmon coupling. This change to the optical spectra could be reversed by ultrasonicating the sample. When compared to the smaller, spherical Ni_3S_2 nanoparticles, the nanorods also showed a very broad absorption at longer wavelengths. This can be attributed to an

LSPR along the longitudinal axis of the rods. In general, the nickel sulfide nanostructures show much broader absorbance bands than comparable Au nanoparticles which are attributed to a larger damping constant in the material. Finally, transient absorption spectroscopy measurements were conducted in order to further confirm the metallic nature of the particles. It was found that upon irradiation with 180 femtosecond laser pulses at the maximum wavelength the plasmon was bleached for a very short time. After initially shifting to longer wavelengths, it was regained in a few picoseconds. All performed measurements and experiments lead to the conclusion that nanoparticles of the investigated nickel sulfide phases show an LSPR maximum in the visible regime of the electromagnetic spectrum.

To examine the nickel sulfide particles as a potential substitute for more expensive noble metal nanoparticles, their optical properties were directly compared to those of Au nanoparticles of the same size. This is shown in chapter 2.3. A method to determine and compare the molar extinction coefficient of both particle species was developed and its results were verified by comparison with literature values for Au nanocrystals. Additionally, Au-Ni_3S_2 core-shell particles were investigated and their synthesis was improved compared to the study shown in chapter 2.2 by minimizing homogeneous nucleation *via* a lower reaction temperature. It was found that at the respective LSPR maximum wavelength the extinction coefficient of Au particles is only about two times larger than the one of Ni_3S_2 particles of the same diameter. The respective value of the core-shell particles can be tuned in between the ones of the pure nanoparticles by varying the shell thickness. However, this comparison does not take into account that the LSPR maximum of the nickel sulfide is much broader and therefore a lot more photons are absorbed at shorter and longer wavelengths than it is the case for the

comparably sharp Au absorbance band. Hence, in total, the number of photons the Ni_3S_2 samples absorb might be similar.

In conclusion, nickel sulfide nanostructures of previously unattainable quality were synthesized and found to exhibit LSPR maxima in the visible part of the electromagnetic spectrum while displaying molar extinction coefficients similar to Au nanocrystals, making them an interesting alternative to noble metal nanoparticles.

2.2 Localized Surface Plasmon Resonances of Various Nickel Sulfide Nanostructures and Au-Ni$_3$S$_2$ Core-Shell Nanoparticles

Rasmus Himstedt, Pascal Rusch, Dominik Hinrichs, Torben Kodanek, Jannika Lauth, Sachin Kinge, Laurens D. A. Siebbeles, and Dirk Dorfs

Localized Surface Plasmon Resonances of Various Nickel Sulfide Nanostructures and Au–Ni$_3$S$_2$ Core–Shell Nanoparticles

Rasmus Himstedt,[†,‡] Pascal Rusch,[†,‡] Dominik Hinrichs,[‡] Torben Kodanek,[‡] Jannika Lauth,[§] Sachin Kinge,[⊥] Laurens D. A. Siebbeles,[§] and Dirk Dorfs*[‡]

[‡]Institute of Physical Chemistry and Electrochemistry, Leibniz Universität Hannover, Callinstraße 3A, 30167 Hannover, Germany

[§]Chemical Engineering Department, Delft University of Technology, Van der Maasweg 9, NL-2629 HZ Delft, The Netherlands

[⊥]Materials Research & Development, Toyota Motor Europe, Hoge Wei 33, B-1930 Zaventem, Belgium

S Supporting Information

ABSTRACT: In this work, we investigate the occurrence of localized surface plasmon resonances (LSPRs) in different nickel sulfide nanostructures. Therefore, spherical and anisotropic nickel sulfide nanoparticles (NPs) are synthesized and analyzed regarding their optical properties by UV/vis/NIR and transient absorption spectroscopy. Furthermore, new pathways for the synthesis of spherical Ni$_3$S$_2$ nanodots with an extremely narrow size distribution, as well as Au–Ni$_3$S$_2$ core–shell NPs with controllable shell thickness, are presented. Our results show that NPs of different metallic nickel sulfide phases like Ni$_3$S$_2$ and Ni$_3$S$_4$ exhibit LSPR bands in the visible regime of the electromagnetic spectrum, which possibly makes them a comparably cheaper alternative to NPs consisting of noble metals like Au and Ag. In case of the presented plasmonic core–shell particles, the resonance frequency of the plasmon can be tuned between those of pure gold and pure Ni$_3$S$_2$ NPs by varying the Ni$_3$S$_2$ shell thickness.
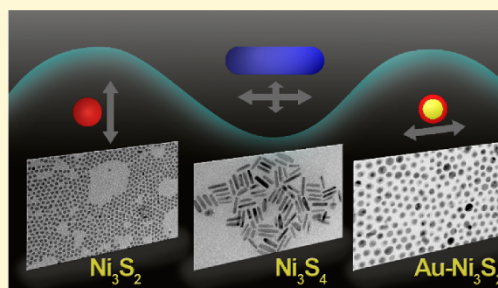
INTRODUCTION

Even though the localized surface plasmon resonance (LSPR) is an optical property of nanoparticles, which by now has been known for more than a century, significant progress toward its understanding has been achieved only in more recent times.[1−5] Besides the classical example of noble metal particles, new plasmonic materials like metal oxides and chalcogenides have been discovered.[6−13] In most of those cases, the necessary amount of free charge carriers exists because of a degenerate doping of the material. In principle, every nanoparticle with a sufficiently large pool of free charge carriers is prone to exhibit a LSPR. In this work, we are going to investigate different materials of the phase-rich binary nickel sulfide system, since nanoparticles of most of the stable phases are likely to show a LSPR due to their metallic nature in the bulk state.[14−16] Because the electronic properties of these materials are well-known, the focus will lie on the paramagnetic rhombohedral Ni$_3$S$_2$ phase (heazlewoodite) and the cubic Ni$_3$S$_4$ phase (polydymite) which displays itinerant electron ferrimagnetism.[17−19]

While Ni$_3$S$_2$ nanostructures have been discussed as a potential electrocatalyst for water splitting or alternatively for the reduction of oxygen to water, Ni$_3$S$_4$ shows potential for application in high-performance supercapacitors.[20−23] In recent years, there has been a significant development in the shape-controlled synthesis of nanoparticles of these pure nickel sulfide

phases. Ni$_3$S$_4$ nanocrystals can be obtained at room temperature by combining aqueous nickel chloride and sodium dithionite solutions and at 180 °C with elemental sulfur in oleylamine or as a byproduct during the synthesis of NiS nanostructures.[19,24−26] Finally, nanopyramids and elongated, rod-shaped nanoprisms of the material can be produced in a one-pot colloidal synthesis.[27] In the case of Ni$_3$S$_2$ it is possible to obtain nanowires or hollow sub-micrometer-sized spheres via gamma irradiation. The most promising results so far in regard to small spherical nanoparticles of Ni$_3$S$_4$ or Ni$_3$S$_2$ are achieved by syntheses in primary amines, which are used as a coordinating solvent.[28−30]

However, the optical properties of nickel sulfide nanoparticles have not been investigated regarding the possible occurrence of a localized surface plasmon resonance. In this article, we describe an optimized nanoparticle synthesis procedure yielding Ni$_3$S$_2$ nanoparticles with a very low degree of polydispersity which is unpreceded in the literature. Furthermore, we provide a detailed study of the optical properties of the as synthesized nanoparticles, which allowed us to conclude that the main absorption band of the nickel sulfide nanoparticles can indeed be attributed to a localized surface

plasmon resonance. Furthermore, heteronanoparticles consisting of an Au core and a nickel sulfide shell were synthesized to investigate the interaction between the well-known LSPR of the noble metal and the nickel sulfide shell material. The obtained results further strengthen the finding that nickel sulfide nanoparticles are plasmonic. Thus, this article widens the field of plasmonic particles active in the visible part of the spectrum and again shows nicely that this field extends far beyond the well-known noble metal nanoparticles.

■ EXPERIMENTAL SECTION

Used Chemicals. Acetone (>99%), chloroform (99.8%), dodecanethiol (DDT, 98%), ethanol (>98%), hexadecanediol (HDD, 98%), n-hexane (99%), 1-octadecene (ODE, 90%), oleylamine (OLAm, 70%), tetrachloroethylene (TCE, > 99%), 1,2,3,4-tetrahydronapthalene (99%), and toluene (99.7%) were purchased from Sigma-Aldrich. Nickel chloride hexahydrate (NiCl$_2$·6H$_2$O, 99.9%), tri$n$-octylphosphine (TOP, 97%) and tri$n$-octylphosphine oxide (TOPO, 99%) were purchased from ABCR. Borane $tert$-butylamine (BBA, 97%), hydrogen tetrachloroaurate trihydrate (HAuCl$_4$·3H$_2$O, 99.99%), methanol (99.9%), nickel 2,4-pentanedioate (Ni(acac)$_2$, 95%), and oleic acid (OLA, 90%) were purchased from Alfa Aesar.

Synthesis of Ni$_3$S$_2$ Nanoparticles. NiCl$_2$·6H$_2$O (24 mg), HDD (63 mg), and TOPO (2.5 g) were mixed in a 25 mL three-neck round-bottom flask and subsequently degassed under vacuum at 90 °C for 2.5 h. Under an argon flow, TOP (1 mL) and DDT (0.225 mL) were added to the resulting solution, which was then stirred at 120 °C for 1.5 h. Afterward, it was heated up to 225 °C using a 20 °C/min heating ramp. After 1 min of reaction time, the heating mantle was removed and the mixture was allowed to cool down to about 70 °C. The whole batch was then transferred via a glass syringe into a centrifuge vial, which contained toluene (5 mL) under argon. The nanoparticles were precipitated by the addition of a mixture of acetone and methanol and subsequent centrifugation (3773 g) for 15 min. The supernatant was discarded and the particles were redispersed in toluene (4.5 mL) and stored under inert atmosphere.

Synthesis of Ni$_3$S$_4$ Nanoparticles. The Ni$_3$S$_4$ nanorods were synthesized by using a slightly modified procedure developed by Liu et al.[27] In a 50 mL three-neck round-bottom flask NiCl$_2$·6H$_2$O (47.5 mg), HDD (105 mg), OLA (200 μL), and OLAm (1.2 mL) were dissolved in ODE (5 mL). The solution was purged of air and water by repeatedly evacuating the flask and flushing with nitrogen. It was then heated up to 90 °C under nitrogen and DDT (450 μL) was added. The resulting mixture was subsequently heated to 225 °C with a rate of 20 °C/min and the temperature was held for 1 min. The product was allowed to cool down to room temperature and the solution was diluted by the addition of toluene (10 mL). The nanoparticles were precipitated by adding acetone (20 mL) and centrifugation (3773 g) for 5 min. After an analogous additional washing step (dispersion in toluene, precipitation with acetone and centrifugation), the product was finally dispersed in toluene and stored under inert atmosphere. This procedure yields nanorods with an average aspect ratio (AR) of 4.6. Particles with an AR of 3.9 were obtained when no OLA was used during the synthesis. When Ni(acac)$_2$ (120.8 mg) was used as Ni precursor instead of NiCl$_2$·6H$_2$O and no OLA was present, then the product consisted of irregularly shaped nanoparticles.

Synthesis of Au Nanoparticles. Au nanoparticles were synthesized according to a method by Zhu et al.[31] In a 50 mL three-neck round-bottom flask, HAuCl$_4$·3H$_2$O (200 mg) was dissolved in 1,2,3,4-tetrahydronapthalene (10 mL) and OLAm (10 mL). The solution was cooled from the outside with ice and stirred for 20 min. Then a mixture of BBA (87 mg) in 1,2,3,4-tetrahydronapthalene (1 mL) and OLAm (1 mL) was added and the resulting solution was stirred for 2 h. The nanoparticles were precipitated by the addition of acetone (45 mL) and centrifugation (3000 g) for 5 min. The supernatant was discarded and the precipitate dispersed and kept in toluene (8 mL). The Au concentration of the Au nanoparticle dispersion was determined using a Varian AA 140 atomic absorption

spectrometer. The solvent (toluene) was evaporated, and the resulting precipitate was dissolved in aqua regia and subsequently diluted with deionized water. The applied wavelength was 242.8 nm and the sample was measured using an acetylene flame.

Synthesis of Au−Ni$_3$S$_2$ Core−Shell Nanoparticles. OLAm (0.25 mL) and ODE (2.5 mL) were mixed in a 25 mL three-neck round-bottom flask and degassed under vacuum at 90 °C for 2 h. Then the solution was heated up to 225 °C under argon. 0.4 mL of the Au nanoparticle dispersion ([Au]: 14 mg/mL, determined by atomic absorption spectroscopy) were dried in vacuum, the particles were redispersed in a mixture of toluene (100 μL), ODE (0.5 mL) and TOP (0.4 mL) and the resulting solution was injected into the reaction flask. The Ni (10.2 mg of NiCl$_2$·6H$_2$O in 0.1 mL of OLAm and 0.9 mL of ODE for a thin shell, 26 mg of NiCl$_2$·6H$_2$O in 0.25 mL of OLAm for a thick shell) and S (0.1 mL of DDT in 0.9 mL ODE for a thin shell, 0.3 mL of DDT for a thick shell) precursor solutions were simultaneously added dropwise over 1−2 min. After an additional minute of reaction time, the reaction mixture was transferred into a centrifuge vial containing toluene (5 mL) under argon using a glass syringe and the particles were precipitated by the addition of ethanol (13.5 mL) and centrifugation (3773 g) for 20 min. The product was then redispersed in toluene (4.5 mL) and stored under an inert atmosphere.

Electron Microscopy. Transmission electron microscopic (TEM) analysis and electron diffraction measurements were performed using a FEI Tecnai G2 F20 device, equipped with a field emission gun and operated at 200 kV. Prior to the measurements the samples were washed at least once by precipitation with ethanol followed by centrifugation and redispersion in chloroform. Ten microliters of the resulting dispersion were then drop-casted onto a carbon-coated copper grid (300 mesh).

Optical Spectroscopy. UV/vis/NIR absorbance spectra were measured in transmission mode using a Cary 5000 spectrophotometer by Agilent Technologies. Pure absorption spectra were collected in the center position of an Agilent DRA-2500 integrating sphere, which was mounted onto the device. The samples were diluted with the respective solvent and placed in a quartz glass cuvette (1 cm path length) under inert atmosphere.

X-ray Diffraction. X-ray diffraction (XRD) patterns were measured with a Bruker D8 Advance in reflection mode. The device was operated at 40 kV and 40 mA utilizing Cu K-alpha radiation. Samples were prepared by drop-casting and drying the NP dispersion on a single crystalline silicon holder.

Transient Absorption Spectroscopy. The LSPR resonance of Ni$_3$S$_2$ nanocrystals in solution (toluene, inside a 2 mm quartz cuvette) was studied by broadband pump−probe spectroscopy in a setup described previously and briefly discussed here.[32,33] 180 fs laser pulses, generated in a Yb:KGW oscillator at 1028 nm, are split-off to generate a pump and a probe beam. The pump beam energy can be varied by nonlinear frequency mixing in an optical parametric amplifier (OPA) and second harmonics generation (Light Conversion, Orpheus). A broadband probe spectrum is generated by focusing the 1028 nm laser light onto a sapphire (500−1500 nm) or a CaF$_2$ (400−600 nm) crystal by nonlinear processes. The probe pulse can be delayed up to 3 ns by an automated delay stage. The majority of the 1028 nm fundamental laser beam is used as pump pulse for photoexciting the sample (wavelengths 310−1500 nm) after nonlinear frequency mixing in an optical parametric amplifier (OPA) and second harmonics module (Light Conversion, Orpheus). The pump and the probe pulse overlap at the sample position in an ∼8° angle. The pump pulse is dumped after the photoexcitation of the sample, while the probe light is led to a detector fiber suitable for the probe spectrum selected (Helios, Ultrafast Systems). The transient absorption spectrum is calculated as the difference between the probe signal obtained respectively with and without photoexcitation by the pump pulses. By controlling the delay stage, we can monitor the spectral response of the sample at different times after photoexcitation. All data are corrected for dispersion by fitting a polynomial function to the solvent response.

RESULTS AND DISCUSSION

Nickel sulfide (Ni_3S_2) nanoparticles (NPs) were produced in a one-pot bottom-up synthesis from $NiCl_2$ and DDT as precursors. TOP acted as capping agent for the particles while TOPO was used as the solvent.

The synthesized nanoparticles are quasi-spherical in shape and possess an average diameter of 5.1 ± 0.4 nm with a narrow size distribution, which has been determined by TEM analysis and are clearly crystalline (see Figure 1A, B). The nickel sulfide
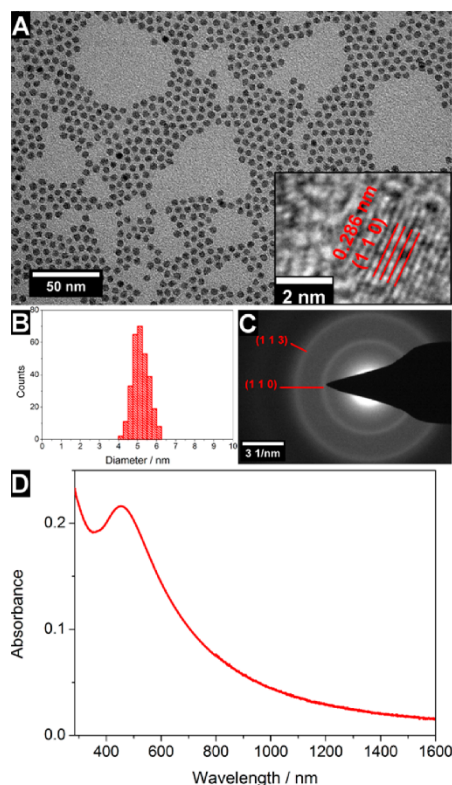

Figure 1. (A) TEM micrograph of Ni_3S_2 nanoparticles. The smaller inset shows a high-resolution TEM of a single particle. The observable lattice planes are attributed to the (1 1 0) planes of Ni_3S_2. (B) Corresponding particle size distribution. The mean diameter of the nanodots is 5.1 ± 0.4 nm and was determined by measuring the size of 300 particles. (C) Electron diffraction pattern of the sample. The visible reflections can be attributed to the (1 1 0) and (1 1 3) lattice planes of Ni_3S_2. (D) UV/vis/NIR absorbance spectrum of the particles dispersed in toluene. A LSPR band emerges at a wavelength of 453 nm.

phase of the obtained nanoparticles was analyzed by high-resolution TEM, electron diffraction (see Figure 1C), and X-ray diffraction (see Figures S1−S3) measurements and was identified as the rhombohedral Ni_3S_2 phase (heazlewoodite). Because bulk heazlewoodite is known as a conventional band metal and an ohmic behavior of a film of particles on a glass substrate has been found (see Figures S4 and S5), nanoparticles of this material should in theory exhibit a localized surface plasmon resonance like other metal nanoparticles.[18] Our samples were therefore investigated in this regard by UV/vis/

NIR absorbance spectroscopy. The results show a single absorbance band in the visible regime of the electromagnetic spectrum at 453 nm which we attribute to the aforementioned LSPR (see Figure 1D). To confirm this thesis, we investigated the influence of the dielectric permittivity of the surrounding medium of the nanoparticles on the position of the LSPR maximum by changing the solvent. Several aliquots of the dispersion were dried under vacuum, followed by a redispersion of the particles in different mixtures of hexane and tetrachloroethylene (ε_m, 1.9 and 2.3, respectively).[34]

The results clearly show how the observed absorbance band shifts toward longer wavelengths with an increasing TCE amount in the mixture (see Figure 2). This is the expected
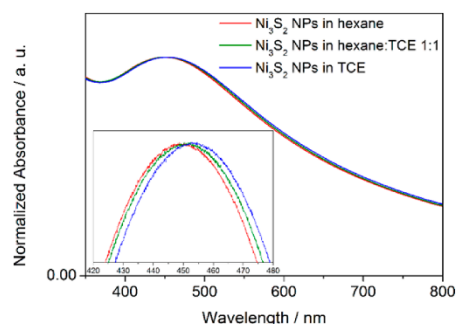

Figure 2. Normalized UV/vis absorbance spectra of Ni_3S_2 nanoparticles dispersed in different volume ratios of hexane to TCE. The inset shows a magnification of the LSPR maximum which is bathochromically shifted by an increasing dielectric permittivity of the surrounding medium.

behavior for a LSPR, since the resonance frequency should decrease with a rising permittivity of the surrounding medium.[35,36] The measured size of the bathochromic shift is only 5−6 nm, because besides solvent molecules there is of course also a large amount of ligand molecules on the surface of the particles, so the effective change to the dielectric medium is by far not as pronounced as it would be for naked nanoparticles. However, a clear tendency is noticeable and well in line with our interpretation.

To further confirm the plasmonic nature of the observed absorbance band, we conducted femtosecond transient absorption spectroscopy measurements (TA). Ni_3S_2 nanoparticles were photoexcited with 180 fs laser pulses at the localized surface plasmon resonance maximum (460 nm, photoexcitation density ∼7.0 × 10^{-13} photons/cm^2, see Figure 3 for comparison of TA bleaches and ground-state absorption).[32,33] Photoexcitation at the plasmon resonance results in the collective excitation of all the conduction electrons. Indeed we find a short-lived bleach of the plasmon absorption band under photoexcitation, which originates from the damping of the localized surface plasmon resonance. The induced absorption features on the higher and lower energy side of the plasmon resonance bleach are also typical for LSPR type absorption bands and originate from the broadening of the plasmon resonance at higher electronic temperatures due to the laser pulses.[37,38] Note that we do not find any long-lasting bleach features that could be assigned to a semiconducting behavior of the Ni_3S_2 nanoparticles. Hence, the TA measure-
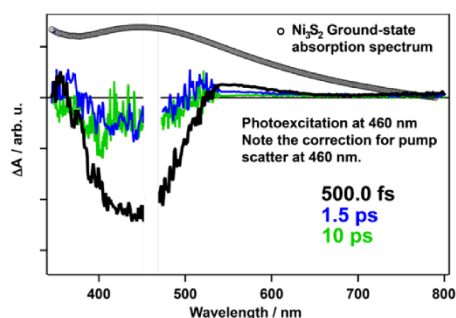
Figure 3. TA spectra of Ni_3S_2 nanoparticles at different times shortly after photoexcitation at 460 nm. The plasmon resonance bleach feature decays after only a few picoseconds and no bleach feature due to semiconducting properties of the Ni_3S_2 nanoparticles is observed.

ments are in good agreement with metallic/plasmonic behavior of the Ni_3S_2 particles.

An important property that is influencing the LSPR is the particle shape. In the case of rod-shaped nanoparticles of noble metals like gold and silver, a second LSPR band at longer wavelengths, which is strongly dependent on the aspect ratio of the long axis to the short axis of the rod, is observed.[3,39] Elongated, rod-shaped nanoprisms of nickel sulfide have already been synthesized by Liu et al. but the optical properties of this material have not yet been investigated.[27]

By slightly modifying the synthesis parameters the aspect ratio (AR) of the nanorods could be tuned between 3.9 and 4.6 while irregularly shaped nanoparticles with much smaller ARs could also be obtained (see Figure 4A−C). The XRD patterns (see Figure 4E) show that the phase of those particles is the metallic spinel-type Ni_3S_4, which name is derived from the mineral polydymite. The absorption spectra (see Figure 4D) show a distinct absorption band at 467 nm for the investigated nanorod samples which is corresponding to the transversal LSPR mode. Additionally, with an increasing AR the absorption of the dispersions at larger wavelengths is rising significantly. Since these spectra were measured in an integrating sphere this observation cannot be explained by a higher scattering background of the sample due to a larger size of the particles. In the case of the nanorods with an AR of 4.6 also a shoulder can be seen at a wavelength of 700−800 nm. The logical conclusion is that the cause for this increasing absorption is a LSPR mode along the longitudinal axis of the nanoparticles.

However, this band is by far not as pronounced and distinct as it is the case for noble metal particles, which could be due to stronger damping mechanisms in the material. Kriegel et al. found a similar behavior for the LSPR of anisotropic $Cu_{2-x}Te$ particles.[40] Instead of distinct longitudinal LSPR bands, they observed a broad absorbance in the IR regime of the electromagnetic spectrum. They attribute this to a strong damping of the anisotropic plasmon mode. The same could be the case for the presented Ni_3S_4 nanorods. In addition to the shape of the nanoparticles and the surrounding dielectric medium, the aggregation of particles severely alters the resonance frequency of the plasmon due to the coupling between the LSPRs of different particles which are in close proximity to each other. A broadening of the band is expected as well as a bathochromic shift of the LSPR maximum.[41] The synthesized Ni_3S_4 nanorods with an AR of 4.6 were investigated in this regard. The particles generally showed a tendency to
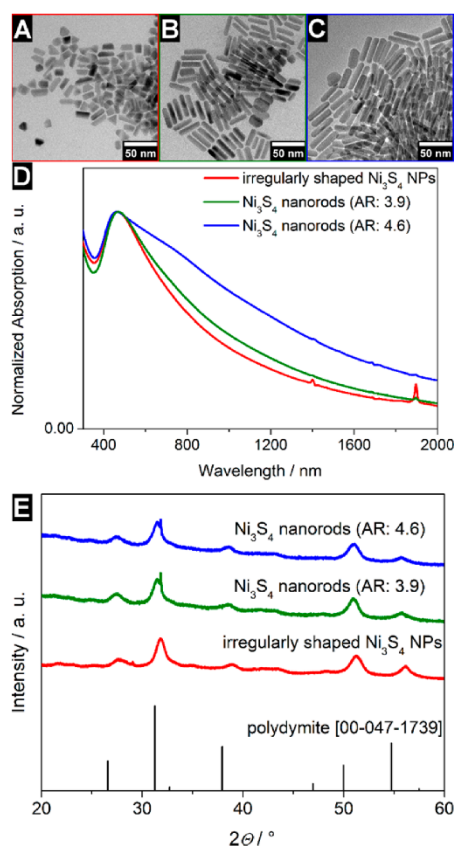

Figure 4. (A−C) TEM micrographs of (A) irregularly shaped Ni_3S_4 nanoparticles, (B) Ni_3S_4 nanorods with an average AR of 3.9, and (C) Ni_3S_4 nanorods with an average AR of 4.6, respectively. (D) Normalized UV/vis/NIR absorption spectra of the nanoparticles dispersed in chloroform. With an increasing particle aspect ratio the absorption at longer wavelengths is becoming stronger. (E) XRD patterns of the shown nanoparticles. The obtained nickel sulfide phase is cubic Ni_3S_4 (polydymite).

aggregate after a few days (see Figure S6). Without treatment with ultrasonication the absorption maximum of these aggregated samples experiences a strong bathochromic shift and also a noticeable broadening of the band (see Figure 5). After an ultrasonication treatment the now dispersed nanoparticles again show the same absorption behavior as freshly synthesized ones. This is also a strong argument for plasmonic coupling between the aggregated nanocrystals.

Yet another way to modify a plasmon resonance is the formation of core−shell nanoparticles. If both the core and the shell are plasmonic, then the LSPR of the hybrid particle tends to shift, starting from the resonance wavelength of the core materials toward the one of the shell material with an increasing shell thickness.[42] A good way to prove that the nickel sulfide absorbance band is indeed a LSPR is therefore to grow a nickel sulfide shell around a plasmonic core which consists of a different material. Preferably, the core material is one with a lower resonance frequency because in case of a nonplasmonic shell the LSPR of the core will be shifted bathochromically, since the dielectric permittivity of the shell material will in most cases
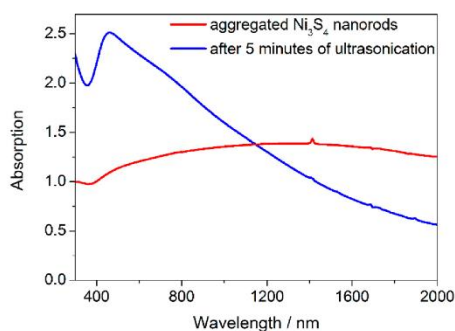
Figure 5. UV/vis/NIR absorption spectra of aggregated Ni_3S_4 nanorods with an AR of 4.6 in chloroform before and after ultrasonication. In the aggregated state, there is a strong and broad absorption in the IR regime of the spectrum because of plasmonic coupling between the nanoparticles.

be much larger than the one of the organic solvent surrounding the core particles. If a hypsochromic shift can be achieved by growing nickel sulfide on a plasmonic core, this would be a very strong indicator for plasmonic properties of nickel sulfide. For this reason, different amounts of nickel sulfide (Ni_3S_2) were grown onto previously synthesized gold seeds. By varying the amount of added Ni and S precursors, $Au-Ni_3S_2$ core−shell particles with different shell thicknesses were successfully synthesized (see Figure 6A−C). The HR-TEM and electron diffraction analysis (see Figure 6D, E, respectively) clearly show that the shell material is Ni_3S_2. Additionally, this was confirmed by X-ray diffraction measurements (see Figure S7). The nanoparticle dispersions also show an absorbance band which is continuously hypsochromically shifted with an increasing

Ni_3S_2 shell thickness. The achievable LSPR positions range from the LSPR position of the pure gold particles toward the absorbance feature of the pure Ni_3S_2 nanoparticles which were discussed earlier (see Figure 6F). This leads to the conclusion that the shell is indeed plasmonic itself, since any sort of dielectric shell around the gold particles would have resulted in a bathochromic shift as shown multiple times in the literature.[43,44] Hence, Ni_3S_2 could be used as an alternative material for plasmonic core−shell nanoparticles, allowing the hypsochromic shifting of the resonance frequency of different materials which exhibit a LSPR at longer wavelengths (e.g., Au nanodots or -rods). While this is in principle also possible using Ag or other noble metals as particle shell, a chalcogenide type material could be of interest due to its significantly altered surface properties compared to a pure noble metal surface and also because of its cheaper price.

■ CONCLUSION

In this work, we present an investigation of the localized surface plasmon resonance of nickel sulfide nanostructures. A new synthesis procedure to obtain highly monodisperse Ni_3S_2 nanodots was developed. These show a distinct absorbance feature in the visible regime of the electromagnetic spectrum which can be shifted bathochromically by increasing the dielectric permittivity of the surrounding medium. Additionally, transient absorption spectroscopy measurements yielded results (e.g., a very short-lived bleaching of the plasmon resonance in the picosecond time regime) which are characteristic for plasmonic materials. Furthermore, Ni_3S_4 nanorods with different aspect ratios were synthesized by slightly altering an existing method. Their absorption at large wavelengths rises with an increasing aspect ratio of the particles due to an emerging longitudinal LSPR mode. They also show a bathochromically shifted and broadened absorption upon
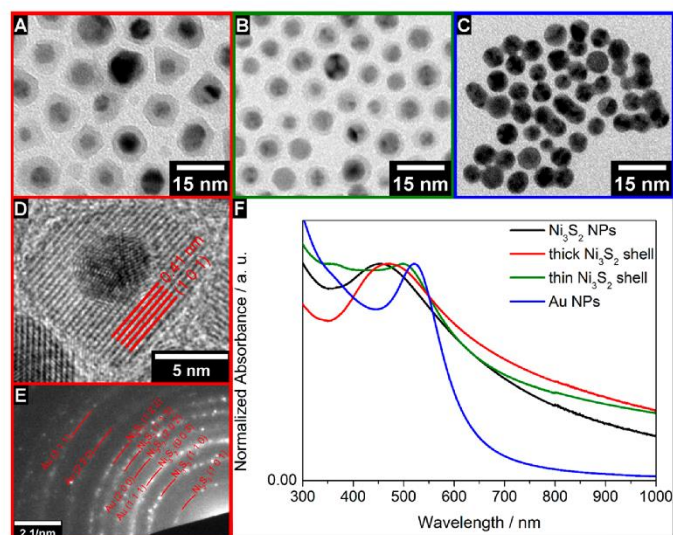

Figure 6. (A−C) TEM micrographs of $Au-Ni_3S_2$ NPs with a (A) thick shell, (B) a thin shell, and (C) pure Au particles. (D) HR-TEM image of a single core−shell particle with a thick shell. The highlighted lattice planes are attributed to the (1 0 1) planes of Ni_3S_2. (E) Electron diffraction pattern of a sample of Au NPs with a thick Ni_3S_2 shell. All reflections can be attributed to either Au or Ni_3S_2. (F) Normalized UV/vis/NIR absorbance spectra of the shown NPs in comparison with pure Ni_3S_2 particles. With increasing shell thickness the absorbance maximum gradually shifts from the LSPR position of pure Au NPs toward that of pure Ni_3S_2 NPs.

Article

aggregation which we attribute to plasmonic coupling between the particles. Finally, Au−Ni_3S_2 core−shell nanoparticles were synthesized for the first time. The absorbance band of these particles gets hypsochromically shifted compared to that of the pure Au seeds depending of the thickness of the Ni_3S_2 shell. This is the expected optical behavior for a plasmonic core−shell particle which shell has a higher resonance frequency than the core. All findings agree with the interpretation that the absorption band of various nickel sulfide nanoparticles can indeed be assigned to a localized surface plasmon resonance, expanding the material class of plasmonic materials with resonances in the visible spectral range further beyond the traditional noble metals.

■ **ASSOCIATED CONTENT**

⑤ Supporting Information

The Supporting Information is available free of charge on the ACS Publications website at DOI: 10.1021/acs.chemmater.7b02259.

> XRD analysis of Ni_3S_2 nanodots and Au−Ni_3S_2 core−shell particles, dynamic light scattering (DLS) measurements of Ni_3S_4 nanorods, four-point probe measurements of a Ni_3S_2 nanoparticle film (PDF)

■ **AUTHOR INFORMATION**

Corresponding Author
*E-mail: dirk.dorfs@pci.uni-hannover.de.

ORCID ⓘ
Laurens D. A. Siebbeles: 0000-0002-4812-7495
Dirk Dorfs: 0000-0001-6175-4891

Author Contributions
†R.H. and P.R. contributed equally.

■ **REFERENCES**

(1) Siedentopf, H.; Zsigmondy, R. Über die Sichtbarmachung und Größenbestimmung ultramikroskopischer Teilchen mit besonderer Anwendung auf Goldrubingläser. *Ann. Phys.* **1902**, *315*, 1−39.
(2) Mie, G. Beiträge zur Optik trüber Medien speziell kolloidaler Metallösungen. *Ann. Phys.* **1908**, *330*, 377−445.
(3) Gans, R. Über die Form ultramikroskopischer Silberteilchen. *Ann. Phys.* **1915**, *352*, 270−284.
(4) Holland, W. R.; Hall, D. G. Surface-Plasmon Dispersion-Relation: Shifts Induced by the Interaction with Localized Plasma Resonances. *Phys. Rev. B: Condens. Matter Mater. Phys.* **1983**, *27*, 7765−7768.

(5) Bohren, C. F.; Huffman, D. R. *Absorption and Scattering of Light by Small Particles*; Wiley: New York, 1983.
(6) Kanehara, M.; Koike, H.; Yoshinaga, T.; Teranishi, T. Indium Tin Oxide Nanoparticles with Compositionally Tunable Surface Plasmon Resonance Frequencies in the Near-IR Region. *J. Am. Chem. Soc.* **2009**, *131*, 17736−17737.
(7) Dorfs, D.; Härtling, T.; Miszta, K.; Bigall, N. C.; Kim, M. R.; Genovese, A.; Falqui, A.; Povia, M.; Manna, L. Reverse Tunability of the Near-Infrared Valence Band Plasmon Resonance in $Cu_{2-x}Se$ Nanocrystals. *J. Am. Chem. Soc.* **2011**, *133*, 11175−11180.
(8) Luther, J. M.; Jain, P. K.; Ewers, T.; Alivisatos, A. P. Localized Surface Plasmon Resonances Arising from Free Carriers in Doped Quantum Dots. *Nat. Mater.* **2011**, *10*, 361−366.
(9) Kriegel, I.; Scotognella, F.; Manna, L. Plasmonic Doped Semiconductor Nanocrystals: Properties, Fabrication, Applications and Perspective. *Phys. Rep.* **2017**, *674*, 1−52.
(10) Comin, A.; Manna, L. New Materials for Tunable Plasmonic Colloidal Nanocrystals. *Chem. Soc. Rev.* **2014**, *43*, 3957−3975.
(11) Zhao, Y.; Burda, C. Development of Plasmonic Semiconductor Nanomaterials with Copper Chalcogenides for a Future with Sustainable Energy Materials. *Energy Environ. Sci.* **2012**, *5*, 5564−5576.
(12) Liu, X.; Swihart, M. T. Heavily-Doped Colloidal Semiconductor and Metal Oxide Nanocrystals: An Emerging New Class of Plasmonic Nanomaterials. *Chem. Soc. Rev.* **2014**, *43*, 3908−3920.
(13) Faucheaux, J. A.; Stanton, A. L. D.; Jain, P. K. Plasmon Resonances of Semiconductor Nanocrystals: Physical Principles and New Opportunities. *J. Phys. Chem. Lett.* **2014**, *5*, 976−985.
(14) Kullerud, G.; Yund, R. A. The Ni-S System and Related Minerals. *J. Petrol.* **1962**, *3*, 126−175.
(15) Adachi, K.; Sato, K.; Takeda, M. Magnetic Properties of Cobalt and Nickel Dichalcogenide Compounds with Pyrite Structure. *J. Phys. Soc. Jpn.* **1969**, *26*, 631−638.
(16) Wang, J. H.; Cheng, Z.; Bredas, J. L.; Liu, M. Electronic and Vibrational Properties of Nickel Sulfides from First Principles. *J. Chem. Phys.* **2007**, *127*, 214705.
(17) Metcalf, P. A.; Crooker, B. C.; McElfresh, M.; Kakol, Z.; Honig, J. M. Low-Temperature Electronic and Magnetic Properties of Single-Crystal Ni_3S_2. *Phys. Rev. B: Condens. Matter Mater. Phys.* **1994**, *50*, 2055−2060.
(18) Lu, Z. W.; Klein, B. M.; Singh, D. J. Electronic Structure of Heazlewoodite Ni_3S_2. *Phys. Rev. B: Condens. Matter Mater. Phys.* **1996**, *54*, 13542−13545.
(19) Manthiram, A.; Jeong, Y. U. Ambient Temperature Synthesis of Spinel Ni_3S_4: An Itinerant Electron Ferrimagnet. *J. Solid State Chem.* **1999**, *147*, 679−681.
(20) Falkowski, J. M.; Concannon, N. M.; Yan, B.; Surendranath, Y. Heazlewoodite, Ni_3S_2; A Potent Catalyst for Oxygen Reduction to Water Under Benign Conditions. *J. Am. Chem. Soc.* **2015**, *137*, 7978−7981.
(21) Feng, L. L.; Yu, G.; Wu, Y.; Li, G. D.; Li, H.; Sun, Y.; Asefa, A.T.; Chen, W.; Zou, X. High-Index Faceted Ni_3S_2 Arrays as Highly Active and Ultrastable Electrocatalysts for Water Splitting. *J. Am. Chem. Soc.* **2015**, *137*, 14023−14026.
(22) Zhang, Y.; Sun, W.; Rui, X.; Li, B.; Tan, H. T.; Guo, G.; Madhavi, S.; Zong, Y.; Yan, Q. One-Pot Synthesis of Tunable Crystalline Ni_3S_4@Amorphous MoS_2 Core/Shell Nanospheres for High-Performance Supercapacitors. *Small* **2015**, *11*, 3694−3702.
(23) Wang, L.; Liu, J.; Zhang, L. L.; Dai, B.; Xu, M.; Ji, M.; Zhao, X. S.; Cao, C.; Zhang, J.; Zhu, H. Rigid Three-Dimensional Ni_3S_4 Nanosheet Frames: Controlled Synthesis and Their Enhanced Electrochemical Performance. *RSC Adv.* **2015**, *5*, 8422−8426.
(24) Jeong, Y. U.; Manthiram, A. Synthesis of Nickel Sulfides in Aqueous Solutions Using Sodium Dithionite. *Inorg. Chem.* **2001**, *40*, 73−77.
(25) Ghezelbash, A.; Korgel, B. A. Nickel Sulfide and Copper Sulfide Nanocrystal Synthesis and Polymorphism. *Langmuir* **2005**, *21*, 9451−9456.

(26) Ghezelbash, A.; Sigman, M. B.; Korgel, B. A. Solventless Synthesis of Nickel Sulfide Nanorods and Triangular Nanoprisms. *Nano Lett.* **2004**, *4*, 537−542.

(27) Liu, Q.; Diaz, A.; Prosvirin, Z.; Luo, Z.; Batteas, D. Shape-controlled Synthesis of Nanopyramids and Nanoprisms of Nickel Sulfide (Ni_3S_4). *Nanoscale* **2014**, *6*, 8935−8942.

(28) Li, J.; Shen, P. K.; Tian, Z. One-Step Synthesis of Ni3S2 Nanowires at Low Temperature as Efficient Electrocatalyst for Hydrogen Evolution Reaction. *Int. J. Hydrogen Energy* **2017**, *42*, 7136−7142.

(29) Hu, Y.; Chen, J.; Li, X. Synthesis of Nickel Sulfide Submicrometer-Sized Hollow Spheres Using a γ-Irradiation Route. *Adv. Funct. Mater.* **2004**, *14*, 383−386.

(30) Gervas, C.; Mlowe, S.; Akerman, M. P.; Ezekiel, I.; Moyo, T.; Revaprasadu, N. Synthesis of Rare Pure Phase Ni_3S_2 and Ni_3S_4 Nanoparticles in Different Primary Amine Coordinating Solvents. *Polyhedron* **2017**, *122*, 16−24.

(31) Zhu, W.; Michalsky, R.; Metin, Ö.; Lv, H.; Guo, S.; Wright, C. J.; Sun, X.; Peterson, A. A.; Sun, S. Monodisperse Au Nanoparticles for Selective Electrocatalytic Reduction of CO_2 to CO. *J. Am. Chem. Soc.* **2013**, *135*, 16833−16836.

(32) Lauth, J.; Kinge, S.; Siebbeles, L. D. A. Ultrafast Transient Absorption and Terahertz Specroscopy as Tools to Probe Photo-excited States and Dynamics in Colloidal 2D Nanostructures. *Z. Phys. Chem.* **2017**, *231*, 107−119.

(33) Spoor, F. C. M.; Kunneman, L. T.; Evers, W. H.; Renaud, N.; Grozema, F. C.; Houtepen, A. J.; Siebbeles, L. D. A. Hole Cooling Is Much Faster than Electron Cooling in PbSe Quantum Dots. *ACS Nano* **2016**, *10*, 695−703.

(34) Wohlfarth, C. *Static Dielectric Constants of Pure Liquids and Binary Liquid Mixtures; Landolt-Börnstein−Group IV Physical Chemistry*; Springer: Berlin, 2008.

(35) Kreibig, U.; Vollmer, M. *Optical Properties of Metal Clusters; Springer Series in Materials Science*; Springer: Berlin, 1995; Vol. 25.

(36) Link, S.; Mohamed, M. B.; El-Sayed, M. Simulation of the Optical Absorption Spectra of Gold Nanorods as a Function of Their Aspect Ratio and the Effect of the Medium Dielectric Constant. *J. Phys. Chem. B* **1999**, *103*, 3073−3077.

(37) El-Sayed, M.; Link, S. In *Semiconductor and Metal Nanocrystals*; Klimov, V. I., Ed.; CRC Press: Boca Raton, FL, 2003.

(38) Link, S.; El-Sayed, M. A. Shape and Size Dependence of Radiative, Non-radiative and Photothermal Properties of Gold Nanocrystals. *Int. Rev. Phys. Chem.* **2000**, *19*, 409−453.

(39) Link, S.; El-Sayed, M. Spectral Properties and Relaxation Dynamics of Surface Plasmon Electronic Oscillations in Gold and Silver Nano-Dots and Nano-Rods. *J. Phys. Chem. B* **1999**, *103*, 8410−8426.

(40) Kriegel, I.; Rodríguez-Fernández, J.; Wisnet, A.; Zhang, H.; Waurisch, C.; Eychmüller, A.; Dubavik, A.; Govorov, A. O.; Feldmann, J. Shedding Light on Vacancy-Doped Copper Chalcogenides: Shape-Controlled Synthesis, Optical Properties, and Modeling of Copper Telluride Nanocrystals with Near-Infrared Plasmon Resonances. *ACS Nano* **2013**, *7*, 4367−4377.

(41) Quinten, M.; Kreibig, U. Optical Properties of Aggregates of Small Metal Particles. *Surf. Sci.* **1986**, *172*, 557−577.

(42) Rodríguez-González, B.; Burrows, A.; Watanabe, M.; Kiely, C. J.; Liz-Marzán, L. M. Multishell Bimetallic AuAg Nanoparticles: Synthesis, Structure and Optical Properties. *J. Mater. Chem.* **2005**, *15*, 1755−1759.

(43) Mulvaney, P. Surface Plasmon Spectroscopy of Nanosized Metal Particles. *Langmuir* **1996**, *12*, 788−800.

(44) Hirakawa, T.; Kamat, P. V. Photoinduced Electron Storage and Surface Plasmon Modulation in Ag@TiO$_2$ Clusters. *Langmuir* **2004**, *20*, 5645−5647.

Supporting Information: Localized Surface Plasmon Resonances of Various Nickel Sulfide Nanostructures and Au-Ni$_3$S$_2$ Core-Shell Nanoparticles

Rasmus Himstedt[†‡], Pascal Rusch[†‡], Dominik Hinrichs[†], Torben Kodanek[†], Jannika Lauth[‖], Sachin Kinge[#], Laurens D. A. Siebbelens[‖] and Dirk Dorfs[†]*

[†]Institute of Physical Chemistry and Electrochemistry, Leibniz Universität Hannover, Callinstraße 3A, 30167 Hannover, Germany

[‖]Chemical Engineering Department, Delft University of Technology, Van der Maasweg 9, NL-2629 HZ Delft, The Netherlands

[#]Toyota Motor Europe, Materials Research & Development, Hoge Wei 33, B-1930, Zaventem, Belgium

Structural analysis of nickel sulfide nanodots

Due to the small size of the nanocrystals (see Figure 1), it is difficult to properly identify their phase using x-ray diffraction. There are very broad reflections visible at the correct angles for Ni$_3$S$_2$ (heazlewoodite), but the result is not definite (see Figure S1).

heazlewoodite [01-073-0698]

2Θ / °
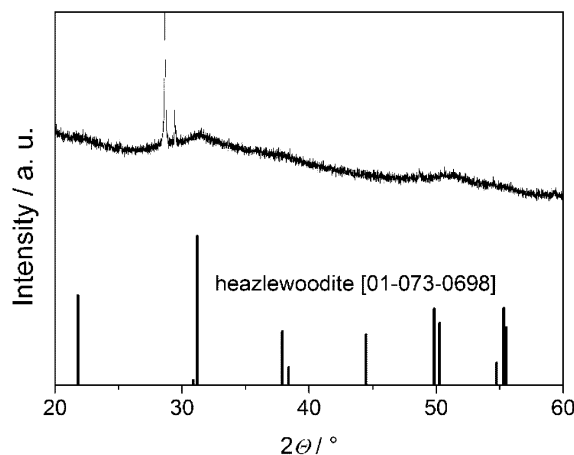
Figure S1. XRD pattern of nickel sulfide nanodots. Broad reflections are visible and can be attributed to the heazlewoodite phase. There also seems to be a contamination of the sample causing sharp reflections at 27-30 °2θ.

However, when the amount of tri-*n*-octylphosphine (TOP) added to the reaction mixture during the synthesis is reduced from 1 to 0.3 mL the small particles from large aggregates (see Figure S2) which do exhibit more intense reflections. The reason for this is the fact that TOP acts as the capping agent and surface ligand to the particles.

1
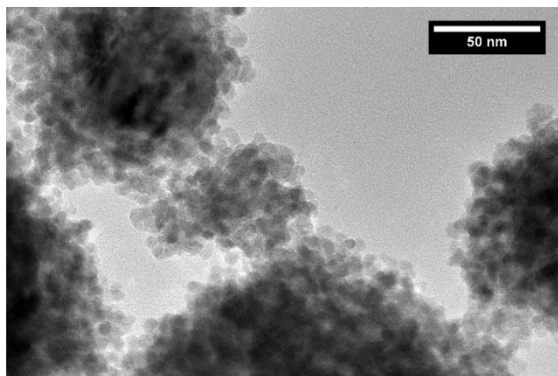
Figure S2. TEM-micrograph of large nickel sulfide aggregates. It can be clearly seen that they consist of single nanodots.

The reflections of the corresponding XRD pattern can be attributed to the heazlewoodite phase without a doubt (see Figure S3). In addition to the presented high-resolution TEM and electron diffraction analysis, (see Figure 1) this leads to the conclusion that the dispersed small particles are of the same phase, since there is no reason to assume that the obtained nickel sulfide phase changes due to an alteration of the TOP concentration.
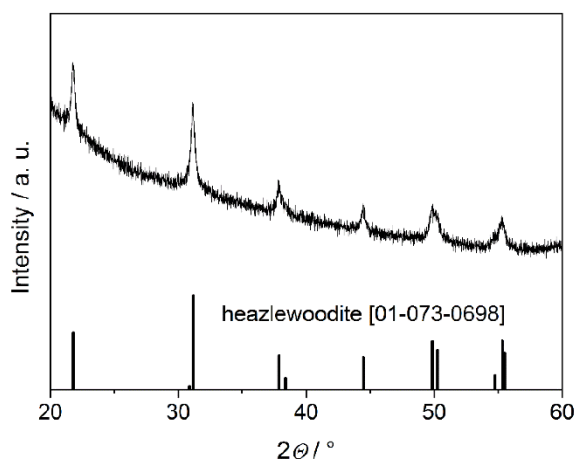
Figure S3. XRD pattern of aggregated nanodots. The reflections can be attributed to the rhombohedral Ni_3S_2 phase.

_I-V_ measurements of a film consisting of Ni_3S_2 nanoparticles

To show the conductivity of the material, a film of Ni_3S_2 nanoparticles (see Figure S2) on a glass substrate was made by simply evaporating the solvent toluene under vacuum (see Figure S4).

2
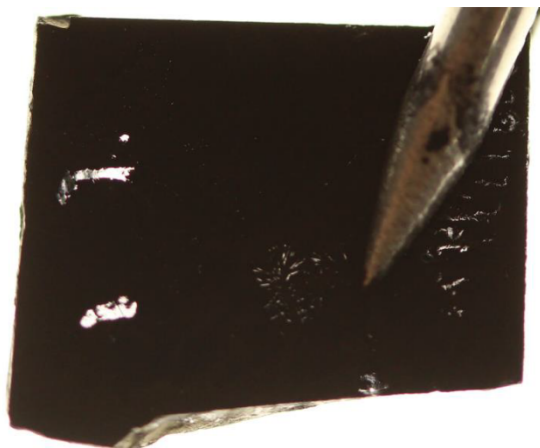
Figure S4. Photograph of a film of Ni$_3$S$_2$ nanoparticles on a glass substrate.

Then the I-V behavior of the film was investigated using the four-point probe method (see Figure S5). The linear fit of the data points clearly shows an ohmic behavior of the nanoparticle film.
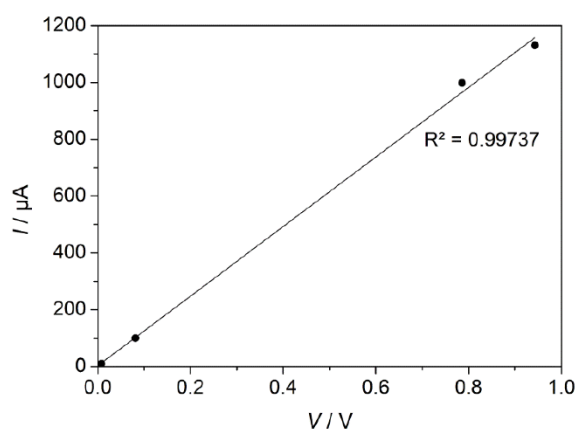
Figure S5. I-V plot of the nanoparticle film. A linear and therefore ohmic behavior of the sample can be clearly seen. The measured sheet resistance of the film amounts to 3708 Ω. The rather large resistance can be mostly attributed to the fact that there are still organic ligands on the particle surface which separate the metallic nanoparticles in the film.

Dynamic light scattering (DLS) measurements of Ni$_3$S$_4$ nanorods

In order to prove that the Ni$_3$S$_4$ nanorods with an aspect ratio of 4.6 shown in Figure 3 and 4 were well-dispersed during our usual spectroscopic analysis and strongly aggregated after a few days, DLS measurements of the investigated solutions were conducted using a Zetasizer Nano ZSP device by Malvern Instruments equipped with a HeNe laser (see Figure S6). The measured hydrodynamic size distribution clearly shows a distinct maximum at about 45 nm in case of the ultrasonicated particles which fits well with an average nanorod length of about 38 nm determined by TEM analysis. The sample that was allowed to stand undisturbed for a few days on the other hand contains larger sized aggregates.
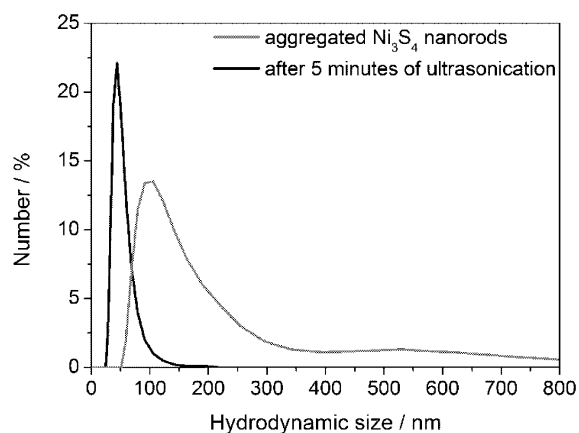
3

Figure S6. DLS measurements of the aggregated and later ultrasonicated Ni$_3$S$_4$ nanorods shown in Figure 3. There are large aggregates visible before the treatment with ultrasonication, while afterwards the nanoparticles are well-dispersed.

XRD analysis of Au-Ni$_3$S$_2$ core-shell nanoparticles

In addition to the presented electron diffraction pattern (see Figure 6E), x-ray diffraction analysis was conducted in case of the core-shell particle with a thick nickel sulfide shell (see Figure S7). The visible reflections can be attributed to Au and Ni$_3$S$_2$.
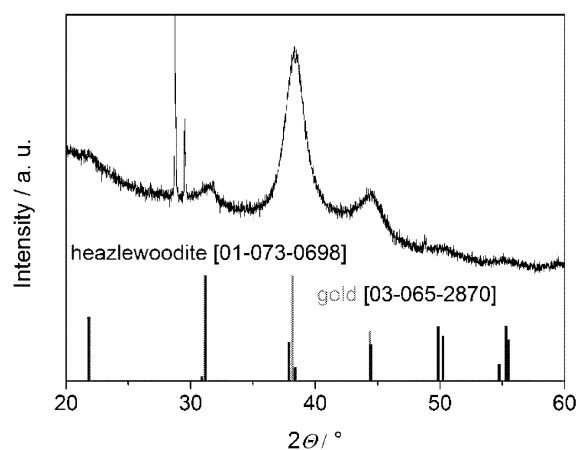
Figure S7. XRD pattern of core-shell nanoparticles with a thick nickel sulfide shell. Most reflections can be attributed to Au and Ni$_3$S$_2$, while 2 sharp reflections which are visible at 27-29 °2θ probably are not caused by the nanoparticles (they were not observed during the electron diffraction analysis of the sample), but by an unknown contamination of the sample. Most likely, this contamination is the same substance which also caused the additional reflections in the XRD pattern of the nanodots.

4

2.3 Extinction Coefficient of Plasmonic Nickel Sulfide Nanocrystals and Gold-Nickel Sulfide Core-Shell Nanoparticles

Rasmus Himstedt, Dominik Hinrichs, and Dirk Dorfs

Rasmus Himstedt[a], Dominik Hinrichs[a] and Dirk Dorfs*

Extinction Coefficient of Plasmonic Nickel Sulfide Nanocrystals and Gold-Nickel Sulfide Core-Shell Nanoparticles

Abstract: In the presented work, the molar extinction coefficient of plasmonic heazlewoodite (Ni_3S_2) nanoparticles and Au-Ni_3S_2 core-shell nanoparticles is determined for the first time. The results are compared to analogously determined extinction coefficients of pure Au nanocrystals (NCs), which themselves correlate very well with existing literature on the subject. The measured extinction coefficients at the localized surface plasmon resonance (LSPR) maximum wavelength of nickel sulfide particles are similar to the values of equally sized Au NCs. Therefore, considering the lower cost of the heazlewoodite material, it could be a reasonable alternative for optical applications of nanoparticles showing a LSPR in the visible regime of the electromagnetic spectrum. Furthermore, this study shows, that by growing a Ni_3S_2 shell onto a pure Au nanocrystal a highly tuneable optical material with variable LSPR frequency and molar extinction coefficient is obtained.

Keywords: colloidal nanocrystals; core-shell nanoparticles; extinction coefficient; localized surface plasmon resonance; nickel sulfide.

1 Introduction

Nanoparticles consisting of materials with a large number of free charge carriers exhibit a unique optical property, the localized surface plasmon resonance (LSPR). Upon irradiation with light of a resonant wavelength, the free charge carriers get collectively excited, resulting in a charge carrier density oscillation.

[a]**Rasmus Himstedt and Dominik Hinrichs:** These authors contributed equally to this work.
*Corresponding author: Dirk Dorfs, Institute for Physical Chemistry and Electrochemistry, Leibniz Universität Hannover, Callinstr. 3A, 30167 Hannover, Germany,
e-mail: dirk.dorfs@pci.uni-hannover.de
Rasmus Himstedt and Dominik Hinrichs: Institute for Physical Chemistry and Electrochemistry, Leibniz Universität Hannover, Callinstr. 3A, 30167 Hannover, Germany

Besides the size and shape of the nanoparticle, the resonance frequency of this oscillation is also strongly dependent on the charge carrier density of the material and their effective mass. For nanocrystals of the noble metals gold and silver, this usually results in a resonance frequency that is located in the visible regime of the electromagnetic spectrum [1]. These particles are an interesting material for optical applications in various fields such as biosensing, imaging, surface-enhanced Raman spectroscopy (SERS) or optical waveguides and antennas [2–8].

The range of existing plasmonic nanomaterials generally spans from metals like the mentioned gold and silver or platinum to degenerately doped semiconductors such as tin-doped indium oxide (ITO) or some copper chalcogenides (e.g. $Cu_{2-x}Se$ or $Cu_{2-x}Te$) [9–12]. Yet, besides the expensive and intensely researched gold and silver, there are only a few known nanoparticle types with a resonance frequency in the visible regime of the electromagnetic spectrum.

Recently, it was found that nanostructures of metallic nickel sulfide phases like heazlewoodite (Ni_3S_2) and polydymite (Ni_3S_4) also meet this criterion [13]. So far these materials have been under investigation as an electrode material for the hydrogen evolution reaction (HER) of electrochemical water splitting or alternatively the reduction of oxygen to water in case of heazlewoodite, while polydymite shows promising properties as a potential supercapacitor [14–17].

In order to evaluate the suitability of these comparably cheap nickel sulfide materials for optical applications, it is important to know their molar extinction coefficient $\varepsilon(\lambda)$ at the LSPR maximum wavelength. Since in previous work it was found that relative to the investigated Ni_3S_4 dispersions, which are prone to show an aggregation of particles over time, the examined Ni_3S_2 colloids are a lot more stable, the focus of this study will be the determination of the extinction coefficient of differently sized Ni_3S_2 nanodots as well as of Au-Ni_3S_2 core-shell nanoparticles.

The extinction behavior of Au nanoparticles of various sizes has been thoroughly studied via optical spectroscopy and it is possible to determine the concentration of gold colloids using only this method if the average nanocrystal diameter is known and the corresponding size distribution is narrow [18–20]. In order to be able to directly compare the obtained results of nickel sulfide nanoparticles to their equally sized noble metal counterparts and to ensure a dependable methodology, the extinction coefficients of both materials need to be determined in exactly the same way.

Thus, the concentration of the respective particles in dispersion will be determined via atomic absorption spectroscopy in combination with electron microscopic analysis and their molar extinction coefficient will be investigated via the LSPR maximum extinction of differently concentrated aliquots, measured with UV/vis absorbance spectroscopy. Our results not only allow to estimate the

concentration of Ni_3S_2 colloids solely via their absorption spectra but at the same time demonstrate that the extinction coefficient of these nanoparticles is (although not as large as the extinction coefficient of gold particles) remarkably high.

2 Experimental section

2.1 Materials

Hydrogen tetrachloroaurate trihydrate ($HAuCl_4 \cdot 3H_2O$, 99.99%), nickel chloride hexahydrate ($NiCl_2 \cdot 6H_2O$, 99.9%), trioctylphosphine (TOP, 97%) and trioctylphosphine oxide (TOPO, 99%) were obtained from ABCR. Borane tertbutylamine complex (BBA, 97%), methanol (99.9%) and 1,2,3,4-tetrahydronaphthalene (97%) were obtained from Alfa Aesar. Acetone (99.7%), chloroform (99.8%), dodecanethiol (DDT, 98%), ethanol (>98%), 1,2-hexadecanediol (HDD, 98%), hydrochloric acid (HCl, >37%), nitric acid (HNO_3, >69%), 1-octadecene (ODE, 90%), oleylamine (OLAM, 70%), and toluene (99.7%) were obtained from Sigma-Aldrich. All chemicals were used as received without further purification.

2.2 Preparation of Ni_3S_2 nanocrystals

Ni_3S_2 nanodots were synthesized following the procedure of a previous work [13]. Briefly, $NiCl_2 \cdot 6H_2O$ (24 mg, 0.1 mmol), HDD (67 mg, 0.26 mmol) and TOPO (2.5 g) were degassed for 2 h at 90 °C. Afterwards TOP (1 mL) and DDT (0.225 mL, 0.94 mmol) were added and the reaction mixture was stirred for 45 min at 120 °C under argon flow. The resulting solution was heated up to 225 °C with a rate of 20 °C/min and kept at this temperature for 1 min before the heating mantle was removed. After cooling down to 70 °C toluene (5 mL), acetone (5 mL) and methanol (20 mL) were added to the mixture and the nanoparticles were precipitated by centrifugation (20 min, 3773 g) before they were redispersed and kept in toluene (4.5 mL).

2.3 Preparation of Au nanocrystals (<6 nm)

The synthesis of small quasi-spherical gold nanocrystals was carried out via the reduction of tetrachloroaurate in presence of oleylamine [21]. $HAuCl_4 \cdot 3H_2O$ (0.2 g, 0.51 mmol) was dissolved in a mixture of 1,2,3,4-tetrahydronaphthalene (10 mL) and OLAM (10 mL). The solution was cooled down to 0 °C. A freshly prepared

solution of BBA (87 mg, 1 mmol) in 1,2,3,4-tetrahydronaphthalene (1 mL) and OLAM (1 mL) was injected to the reaction mixture. The solution was stirred for two additional hours. Afterwards, the Au NCs were precipitated by the addition of acetone ($\approx$140 mL), centrifuged (5 min, 5000 g) and redispersed in toluene. This cleaning step was repeated. Finally, the product was dispersed in toluene. The average diameter of the Au NCs of the obtained highly monodisperse colloids varies from batch to batch between 4 nm to 6 nm. Smaller Au NCs can be produced with increased reaction temperature (e.g. 40 °C for <3 nm).

2.4 Preparation of Au nanocrystals (>6 nm)

For the preparation of larger Au NCs, a seed-mediated growth approach was used and modified [22]. For the synthesis of 10 nm gold nanocrystals, previously prepared Au NCs ($\approx$6 nm diameter, 30 mg) were dispersed in a solution of $HAuCl_4 \cdot 3H_2O$ (100 mg) in ODE (10 mL) and OLAM (10 mL). The temperature was increased to 80 °C within 10 min and was held for additional 2 h. The product was precipitated by the addition of acetone, centrifuged (5 min, 5000 g), and dispersed in toluene. This solution was used for a consecutive second growing step with $HAuCl_4 \cdot 3H_2O$ (320 mg) in ODE (27 mL) and OLAM (27 mL). After purification by precipitation with acetone and centrifugation (5 min, 5000 g), the particles were collected in toluene. For the preparation of different Au NCs sizes, the amount of gold precursor and/or the number of growing steps can be varied.

2.5 Preparation of Au-Ni$_3$S$_2$ core-shell nanoparticles

Au-Ni$_3$S$_2$ core-shell particles were synthesized according to a slightly modified version of a previously reported procedure [13]. First, $NiCl_2 \cdot 6H_2O$ (9.4 mg, 40 μmol) was dissolved in ODE (5 mL) and OLAM (0.5 mL) and degassed for 1 h at 80 °C. Then the solution was heated up to 200 °C under argon flow and Au seed crystals (4.1 nmol), dispersed in a mixture of toluene (0.1 mL), ODE (0.5 mL), OLAM (0.25 mL) and TOP (0.4 mL), were injected. Directly afterward DDT (0.1 mL, 0.4 mmol) in ODE (1 mL) was added dropwise over 1 min. After an additional minute of reaction time, the resulting mixture was quenched with toluene (5 mL). The nanoparticles were precipitated by the addition of ethanol (12 mL) and centrifugation (20 min, 3773 g) and were finally redispersed and stored in toluene (4 mL). The used amount of the nickel and sulfur precursors can be varied in order to obtain shells with different thicknesses if Au seeds of the same size are used.

2.6 Optical spectroscopy

The UV/vis extinction spectroscopy was carried out at an Agilent Cary 5000 UV/vis/NIR spectrophotometer. The sample stock solutions were diluted to various concentrations in pure toluene (in case of the Ni_3S_2 NCs and the core-shell particles) or in toluene with 1 vol% of oleylamine (in case of the pristine Au NCs) in a quartz glass cuvette with 10 mm path length. The optical densities of all samples were kept below 0.8 to ensure the linear dependence of extinction and particle concentration.

2.7 Elemental analysis

The nickel and gold mass concentrations of the stock solutions were determined by atomic absorption spectroscopy (AAS) using a Varian AA 140 spectrometer. Aliquots of the stock solutions were taken and the solvent was completely evaporated. Subsequently, the residual solid was dissolved in aqua regia. These solutions were diluted with deionized water. The extinctions in the atomic absorption spectrometer were measured in relation to separately prepared calibration standards with known Ni and Au mass concentration. In case of the core-shell nanoparticles, only the Ni mass concentration was determined and used, since the presence of Ni disturbs the Au AAS measurement.

2.8 Electron microscopy

Transmission electron microscopy (TEM) was performed using a FEI Tecnai G2 F20 with a field emission gun operated at 200 kV. All samples were cleaned via precipitation and centrifugation. The specimens were prepared by drop casting the cleaned samples onto a copper grid supported carbon film from Quantifoil.

3 Results and discussion

The synthesized nanoparticles are shown in TEM images in Figure 1. It can be seen that quasi-spherical monodisperse particles were obtained in case of the heazlewoodite (Ni_3S_2) nanodots (see Figure 1a) as well as in case of the Au nanocrystals (see Figure 1b) and the Au-Ni_3S_2 core-shell structures with different sizes for the Au-core and the Ni_3S_2-shell (see Figure 1c + d). Compared to an
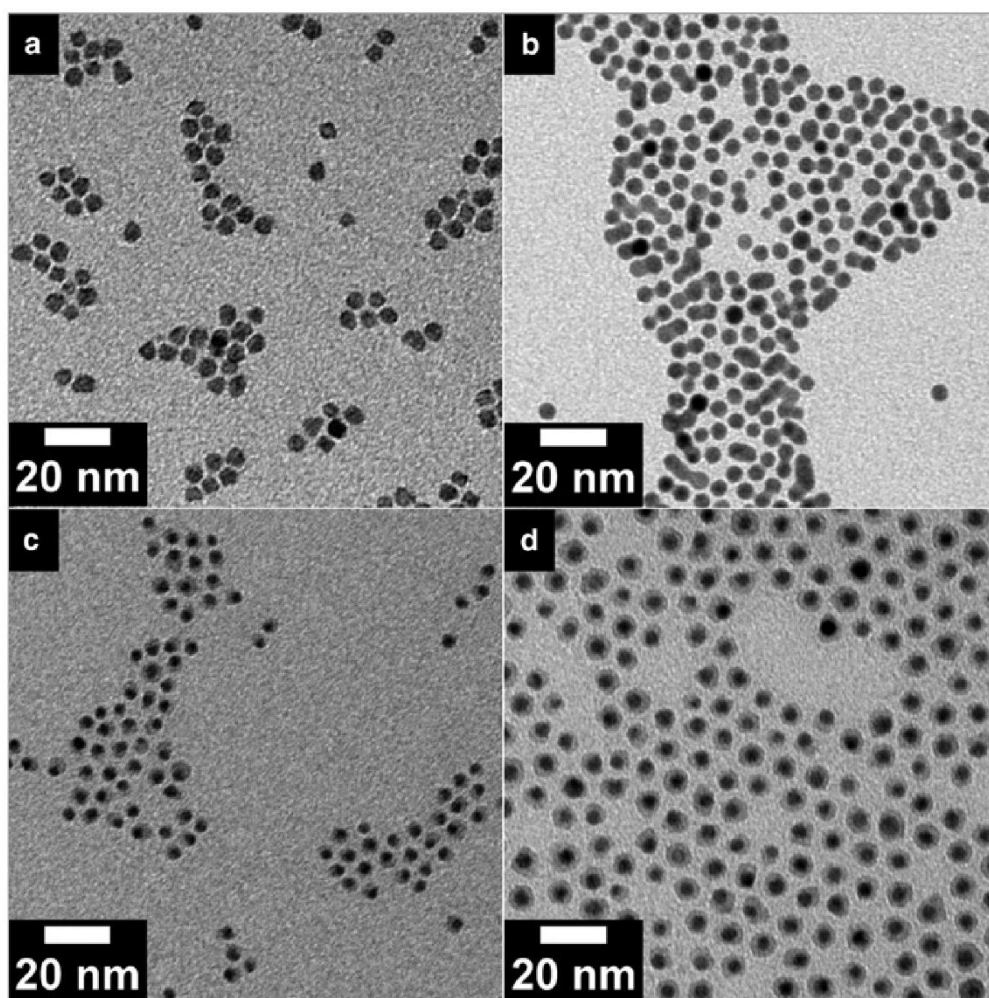
Fig. 1: TEM micrographs of Ni_3S_2 nanodots with an average diameter of 5.3 ± 0.5 nm (a), Au nanocrystals with an average diameter of 5.3 ± 0.4 nm (b) and Au-Ni_3S_2 core-shell nanoparticles with average particle diameters of 5.2 ± 0.5 nm (average core diameter: 3.5 ± 0.3 nm) (c) and 7.0 ± 0.6 nm (average core diameter: 4.5 ± 0.4 nm) (d), respectively. The nanocrystals in (b) were used as seeds for the synthesis of core-shell particles shown in (d). The Au cores were obviously slightly etched during the reaction, reducing their size from 5.3 ± 0.4 to 4.5 ± 0.4 nm. This observation was made in case of all the investigated core-shell samples and has been taken into account for the determination of their particle concentration via AAS measurements.

earlier study on this material the uniformity of the core-shell structures could be improved and homogenous Ni_3S_2 nucleation was suppressed by reducing the reaction temperature for the synthesis of the hybrid particles from 225 to 200 °C [13]. Additional TEM analysis and the size distributions for each further investigated sample can be found in the Supporting information (see Figures S1, S2 and S6).

For a comparison of the molar extinction coefficient of the different particle types, it is necessary to produce nanoparticles with a very similar total diameter, which is the case for the shown pure nanocrystals, and the core-shell particles in Figure 1c since they all have an average diameter of about 5.3 nm with a very small standard deviation. Additional sources for errors are the fact that the Ni_3S_2 nanodots are clearly more faceted and therefore less spherical than the Au particles and that the growth of a very thin nickel sulfide shell onto small Au cores apparently in some cases results in slightly anisotropic core-shell structures.

The optical spectra of the investigated nanoparticles are presented in Figure 2. All samples show a LSPR band in the visible regime of the electromagnetic spectrum. Compared to the Au LSPR, the maximum of the Ni_3S_2 band is found at a shorter wavelength. While depending on the size of the examined nanoparticles, the LSPR maximum of the core-shell particles generally tends to be strongly shifted towards the position of the shell material LSPR. It can also be seen that
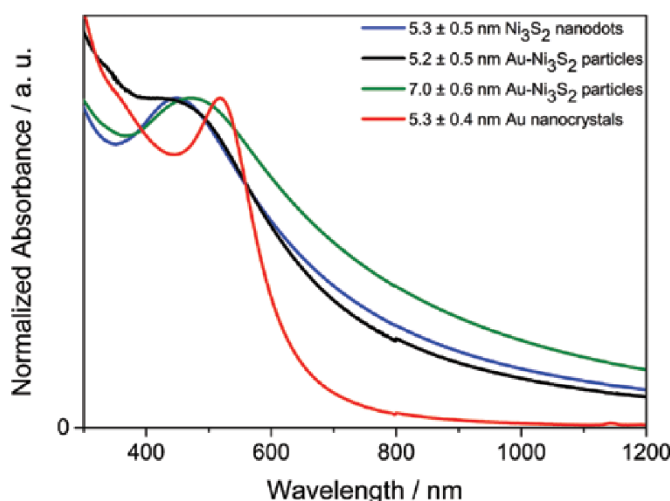
Fig. 2: Normalized UV/vis absorbance spectra of 5.3 nm Ni_3S_2 nanodots (blue line), 5.3 nm Au nanocrystals (red line) and Au-Ni_3S_2 core-shell nanoparticles with diameters of 5.2 nm (black line) and 7.0 nm (green line) in toluene. The spectral position of the core-shell particle LSPR (green line) is hypsochromically shifted from the position of the pure Au seeds at 517 nm towards the position of the Ni_3S_2 nanodots at 448 nm due to the growth of the plasmonic shell around the Au core. While a hypsochromic shift of the LSPR maximum, in general, could also partially be explained by the fact that the gold is slightly etched during the core-shell synthesis, even very small Au particles do not show a pronounced LSPR band at wavelengths this short (see Table S2 in the Supporting information). In case of core-shell particles with a smaller core, the LSPR maximum can be found at an even shorter wavelength. It is also obvious that the spectral linewidth of the LSPR band of the Ni_3S_2 and core-shell particles is much broader than the one of the Au nanocrystals of the same size and of similar monodispersity, which could be due to stronger damping processes of the plasmon in the nickel sulfide material.

the absorbance band of the nickel sulfide particles is much broader than the Au particle plasmon band, which is probably due to stronger damping effects in the material and leads to an extinction that is spread out over a larger part of the spectrum and therefore smaller at the maximum wavelength.

The particle concentrations c_{NC} of the synthesized dispersions were determined by measuring the Au/Ni mass concentration of the respective sample via AAS and correlating the obtained values with the nanoparticle size distributions gained by the TEM analysis. Following this, the extinction or attenuation A of several different dilutions of the samples at their respective LSPR maximum wavelength λ_{max} was measured. Using the Beer–Lambert law (see Equation 1, l represents the light path length through the sample, which in this case is 1 cm and corresponds to the length of the used cuvettes) the molar extinction coefficient $\varepsilon_{NC}(\lambda_{max})$ of the nanostructures could be determined via a linear fit to the measured extinction values [23]. The slope of the obtained linear regression represents ε_{NC}.

$$A = \varepsilon_{NC} \cdot c_{NC} \cdot l \tag{1}$$

An exemplary spectroscopic determination of the molar extinction coefficient is shown in Figure 3 (for detailed data on all investigated samples see also the Supporting information).

The analogously obtained results for all investigated nanoparticle samples are summarized in Figure 4. The molar extinction coefficient of the Au NCs at the LSPR maximum rises linearly with an increasing particle diameter in logarithmic coordinates, which is in accordance with recent literature and the obtained values also fit well (see a detailed comparison in Figure S5 of the Supporting information) [18–20, 24, 25]. The dependency of ε on the particle diameter D is given by Equation 2 [19].

$$\ln(\varepsilon) = k \ln(D) + a \tag{2}$$

While for Au NCs a usually lies between 9.8 and 11.2, k tends to have a value close to 3 (between 3 and 4 in recent literature), owing to the dependency of the nanoparticle extinction cross section on the particle volume and therefore D^3 [18–20, 25]. In case of the Au NCs investigated here, k and a have values of 3.5 and 10.8, respectively.

In relation to the gold particles, the ε values for the Ni_3S_2 nanodots are smaller which indicates a lower oscillator strength of the material. However, they are still in a similar range. The molar extinction coefficient of 5.3 nm Au nanocrystals, for example, is only about 2 times larger than the value of similarly sized Ni_3S_2
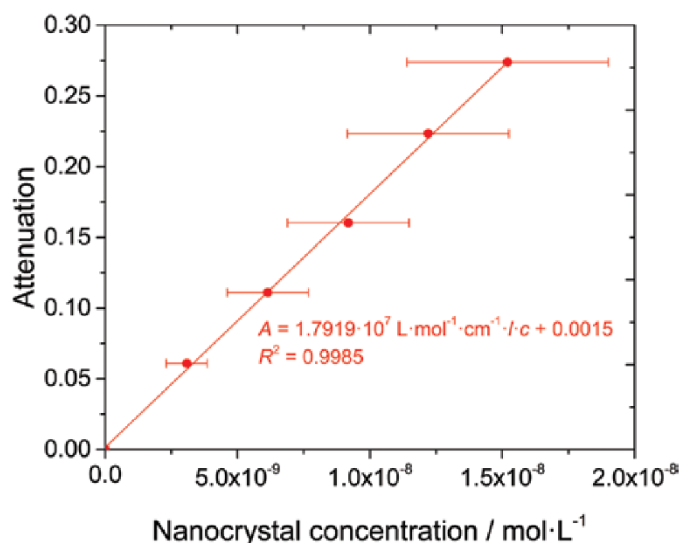
Fig. 3: Example for the spectroscopic determination of the molar extinction coefficient for oleylamine-stabilized gold nanocrystals in toluene. The particles have an average diameter of 5.3 ± 0.4 nm and the attenuation of different nanoparticle concentrations at the LSPR maximum wavelength (518 nm in this case) was measured via UV/vis absorbance spectroscopy. The error bars originate from the standard deviation of the average nanocrystal diameter and its effect on the calculated particle concentrations via the measured Au mass concentration. It can be seen that the attenuation is linearly dependent on the concentration in case of the investigated optical densities. According to the Beer–Lambert law and knowing that the path length l of the light is 1 cm, which is the length of the used cuvette, ε can be inferred via the slope of a linear fit to the measured data points. In this case, the obtained value for the molar extinction coefficient is $1.7919 \cdot 10^7 \pm 314{,}707$ L $\cdot$ mol^{-1} $\cdot$ cm^{-1} while R^2 for the used linear fit is 0.9985.

nanodots. There is also a rather steep increase in the ε value from a diameter of 5.1 to 5.3 nm. However, in addition to the generally expected increase, the crystallinity of the particles could also play a role leading to this observation since due to fewer crystal defects more crystalline nickel sulfide particles tend to show less LSPR damping, therefore a smaller LSPR bandwidth, and a larger attenuation at λ_{max}.

For a fair evaluation and comparison of the two materials it is important to note that compared to the Au particles Ni_3S_2 nanostructures absorb a lot of light at different wavelengths than the LSPR maximum wavelength λ_{max} due to their broader absorbance band, which in turn leads to a smaller determined molar extinction coefficient $\varepsilon(\lambda)$ at the investigated light wavelength. Therefore, the total oscillator strength of the two materials could be almost equal.

Intermediary ε values can be obtained by growing a nickel sulfide shell around gold cores. The oscillator strength of the core-shell particle seems to be a combination of the ones of the pure metals. This can be seen by looking at the
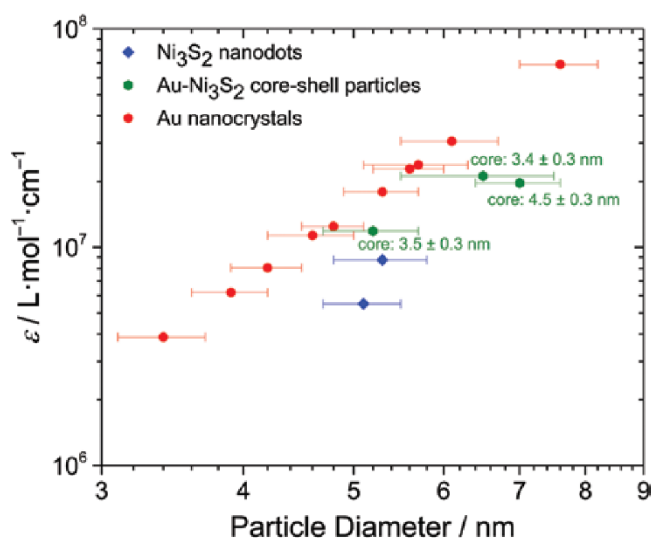
Fig. 4: Measured extinction coefficients of quasi-spherical Au and Ni_3S_2 nanocrystals as well as $Au\cdot Ni_3S_2$ core-shell nanoparticles of different sizes at the corresponding λ_{max} in toluene. The error bars correlate to the respective standard deviations of the size distributions of the investigated nanoparticle samples. While there is a clear linear dependency of the Au extinction coefficient on the particle diameter in logarithmic coordinates, the ε value of Ni_3S_2 nanodots is smaller than the one of Au particles of the same size indicating a smaller oscillator strength of their LSPR. The extinction coefficient of the core-shell particles, on the other hand, lies between the values for similarly sized Au and Ni_3S_2 nanoparticles.

extinction coefficient of 5.2 nm $Au\text{-}Ni_3S_2$ particles, which is found in between the values for respective pure NCs of almost the same size. This means that in addition to its LSPR maximum wavelength the oscillator strength of an Au nanoparticle can also be adjusted by a controlled Ni_3S_2 shell growth. It is also visible that an increasing shell thickness around cores of the same size leads to an accordingly increased molar extinction coefficient. The reason why the value for the largest (7 nm diameter) core-shell particles is apparently smaller than the one of the 6.5 nm sized nanoparticles could be because the latter sample shows a comparably broad size distribution (see also the Supporting information for more details) with a few strongly absorbing larger and possibly more crystalline particles, which are increasing the average molar extinction coefficient of the whole ensemble.

4 Conclusion

In conclusion, this work represents the first determination of the molar extinction coefficient at the localized surface plasmon resonance of Ni_3S_2 nanodots

and Au-Ni$_3$S$_2$ core-shell nanoparticles. The synthesis of the hybrid particles was also improved compared to recent literature in order to obtain uniform core-shell structures without any visible homogeneously nucleated nickel sulfide crystals or remaining pure gold seeds left in the resulting dispersions. The extinction coefficient at the LSPR maximum is an important factor to keep in mind for any kind of possible optical application of these materials. The measured values are slightly smaller than the ones of similarly sized gold nanoparticles, possibly owing to the broader LSPR absorbance band of the nickel sulfide material. Yet, considering their far smaller cost, heazlewoodite nanostructures could still be an interesting alternative to the commonly used noble metal nanoparticles depending on the specific application. Furthermore, it is possible to modify the molar extinction coefficient as well as the LSPR frequency of the Au/Ni$_3$S$_2$ core-shell particles by varying the Ni$_3$S$_2$ shell thickness, resulting in a highly tunable optical material.

5 Supporting information

TEM analysis including size distributions, the spectroscopic determination of molecular extinction coefficients and a summary of the respective values for all investigated samples as well as a comparison of the obtained results for Au NCs with the existing literature.

References

1. S. Link, M. A. El-Sayed, Int. Rev. Phys. Chem. **19** (2000) 409.
2. K. A. Willets, R. P. Van Duyne, Annu. Rev. Phys. Chem. **58** (2007) 267.
3. E. C. Dreaden, A. M. Alkilany, X. Huang, C. J. Murphy, M. A. El-Sayed, Chem. Soc. Rev. **41** (2012) 2740.
4. W. Zhou, X. Gao, D. Liu, X. Chen, Chem. Rev. **115** (2015) 10575.
5. X. Yang, M. Yang, B. Pang, M. Vara, Y. Xia, Chem. Rev. **115** (2015) 10410.
6. L. A. Lane, X. Qian, S. Nie, Chem. Rev. **115** (2015) 10489.
7. J. R. Krenn, Nat. Mater. **2** (2003) 210.
8. A. P. Mühlschlegel, H. Eisler, O. J. F. Martin, B. Hecht, D. W. Pohl, Science **308** (2005) 1607.
9. M. Kanehara, H. Koike, T. Yoshinaga, T. Teranishi, J. Am. Chem. Soc. **131** (2009) 17736.

10. J. M. Luther, P. K. Jain, T. Ewers, A. P. Alivisatos, Nat. Mater. **10** (2011) 361.

11. D. Dorfs, T. Härtling, K. Miszta, N. C. Bigall, M. R. Kim, A. Genovese, A. Falqui, M. Povia, L. Manna, J. Am. Chem. Soc. **133** (2011) 11175.

12. I. Kriegel, J. Rodriguez-Fernandez, A. Wisnet, H. Zhang, C. Waurisch, A. Eychmüller, A. Dubavik, A. O. Govorov, J. Feldmann, ACS Nano **7** (2013) 4367.

13. R. Himstedt, P. Rusch, D. Hinrichs, T. Kodanek, J. Lauth, S. Kinge, L. D. A. Siebbeles, D. Dorfs, Chem. Mater. **29** (2017) 7371.

14. L. L. Feng, G. Yu, Y. Wu, G. D. Li, H. Li, Y. Sun, T. Asefa, W. Chen, X. Zou, J. Am. Chem. Soc. **137** (2015) 14023.

15. J. M. Falkowski, N. M. Concannon, B. Yan, Y. Surendranath, J. Am. Chem. Soc. **137** (2015) 7978.

16. L. Wang, J. Liu, L. L. Zhang, B. Dai, M. Xu, M. Ji, X. S. Zhao, C. Cao, J. Zhang, H. Zhu, RSC Adv. **5** (2015) 8422.

17. Y. Zhang, W. Sun, X. Rui, B. Li, H. T. Tan, G. Guo, S. Madhavi, Y. Zong, Q. Yan, Small **11** (2015) 3694.

18. K. S. Lee, M. A. El-Sayed, J. Phys. Chem. B **110** (2006) 19220.

19. X. Liu, M. Atwater, J. Wang, Q. Huo, Colloids Surf. B Biointerfaces **58** (2007) 3.

20. G. A. Rance, D. H. Marsh, A. N. Khlobystov, Chem. Phys. Lett. **460** (2008) 230.

21. S. Peng, Y. Lee, C. Wang, H. Yin, S. Dai, S. Sun, Nano Res. **1** (2008) 229.

22. W. Zhu, R. Michalsky, Ö. Metin, H. Lv, S. Guo, C. J. Wright, X. Sun, A. A. Peterson, S. Sun, J. Am. Chem. Soc. **135** (2013) 16833.

23. A. Beer, Ann. Phys. **162** (1852) 78.

24. A. I. Dolinnyi, Colloid J. **79** (2017) 611.

25. M. M. Maye, L. Han, N. N. Kariuki, N. K. Ly, W. Ben Chan, J. Luo, C. J. Zhong, Anal. Chim. Acta **496** (2003) 17.

1

Rasmus Himstedt[‡], Dominik Hinrichs[‡] and Dirk Dorfs[*]

Supporting Information: Extinction Coefficient of Plasmonic Nickel Sulfide Nanocrystals and Gold-Nickel Sulfide Core-Shell Nanoparticles

Ni_3S_2 Nanodots

Representative TEM images and the correlating size distributions of the investigated Ni_3S_2 nanocrystal (NC) samples are presented in Figure S1. It can be seen that the nanoparticles are quasi-spherical in shape and show a low degree of polydispersity.
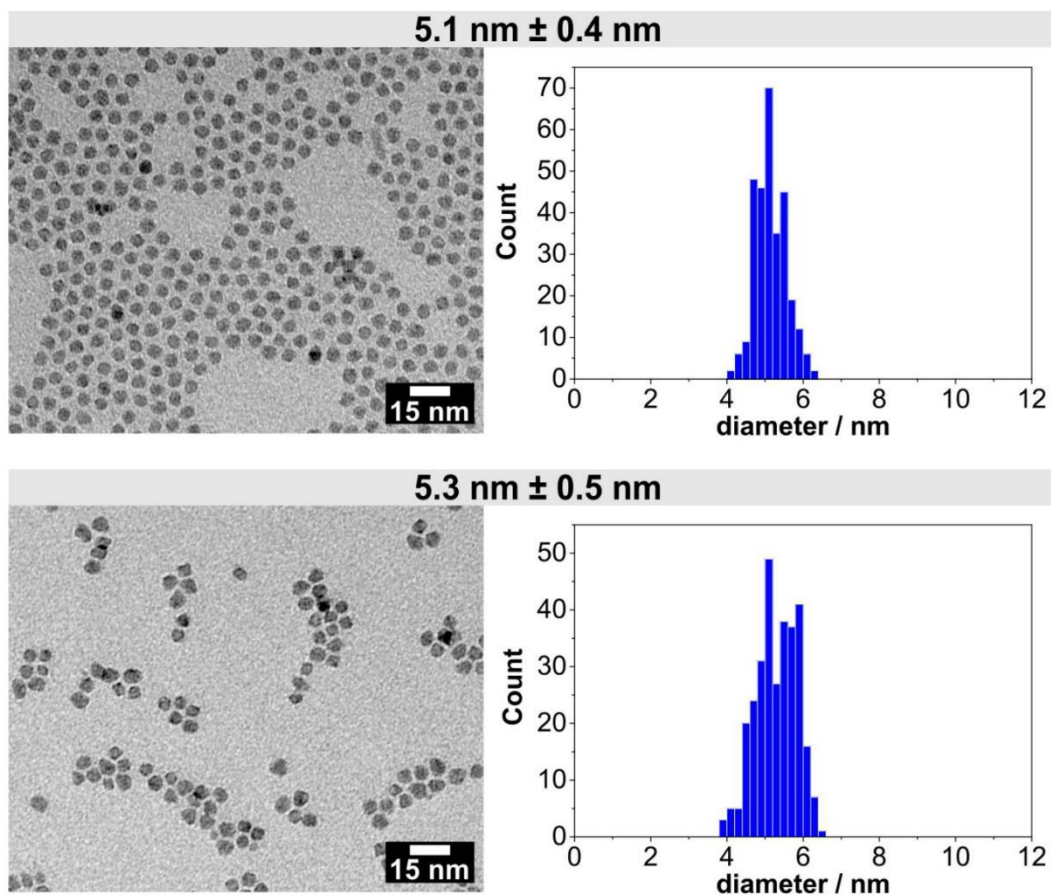

Fig. S1: TEM micrographs and size distributions of the used Ni_3S_2 nanoparticle samples.

[*]**Corresponding Author: Dirk Dorfs**, Institute for Physical Chemistry and Electrochemistry, Leibniz Universität Hannover, Callinstr. 3A, 30167 Hannover, Germany, email: dirk.dorfs@pci.uni-hannover.de

[‡]**These authors contributed equally: Rasmus Himstedt and Dominik Hinrichs**, Institute for Physical Chemistry and Electrochemistry, Leibniz Universität Hannover, Callinstr. 3A, 30167 Hannover, Germany

2

In order to determine the molar extinction coefficient ε of the nanoparticles, the extinction values at the LSPR maximum λ_{max} of particle dispersions with different concentrations were measured. The results are shown in Figure S2 and a clear linear dependency is visible. The slope of the linear fit corresponds to the molar extinction coefficient. It is also obvious that the larger particles exhibit a much steeper slope than the smaller ones.
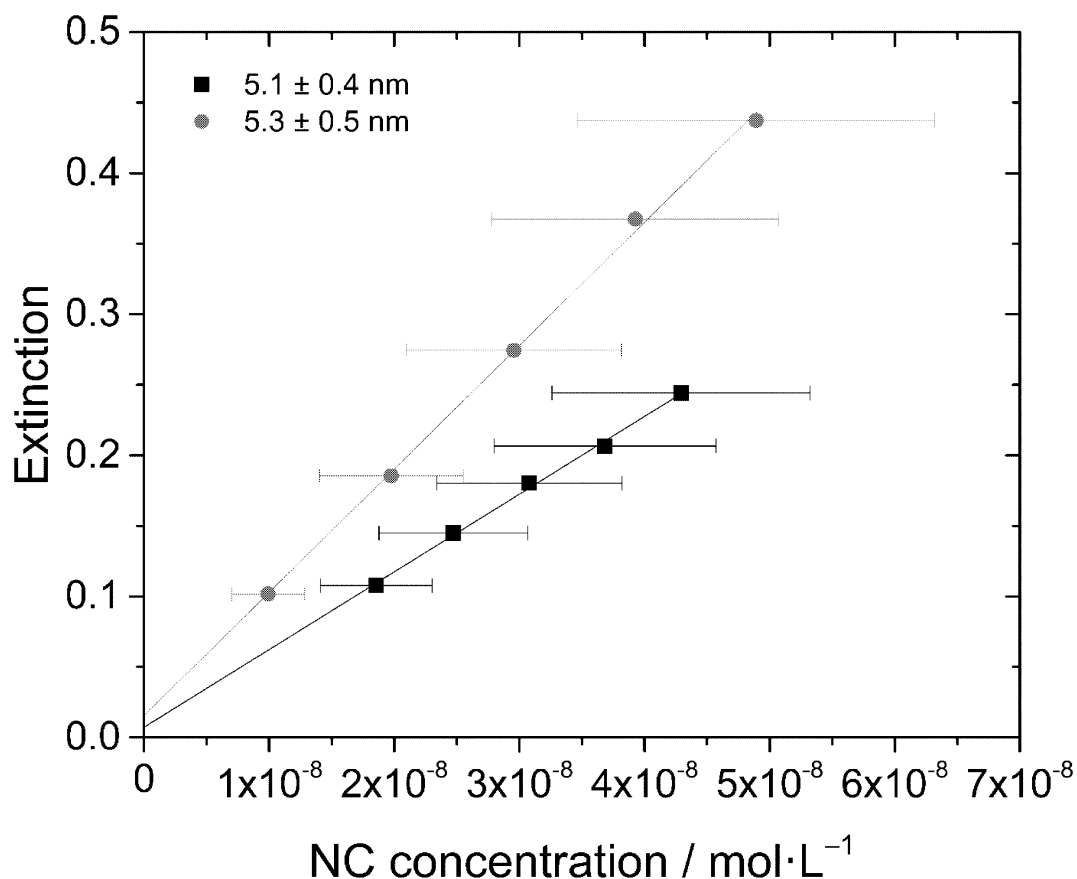

Fig. S2: Extinction values at the Ni_3S_2 LSPR maximum depending on the nanoparticle concentration in toluene. The samples were measured in 10 mm quartz-glass cuvettes. The error bars originate from the influence of the standard deviation of the particle diameter on the NC concentration via the determined Ni mass concentration.

The ε values for the different particle sizes are summarized in Table S1.

Tab. S1: Extinction coefficient of differently sized Ni_3S_2 nanodots in toluene.

d / nm	Δd / nm	λ_{max} / nm	ε / $L \cdot mol^{-1} \cdot cm^{-1}$	$\Delta\varepsilon$ / $L \cdot mol^{-1} \cdot cm^{-1}$
5.1	0.4	452	$5.5102 \cdot 10^6$	161969
5.3	0.5	448	$8.7452 \cdot 10^6$	201154

Au Nanocrystals

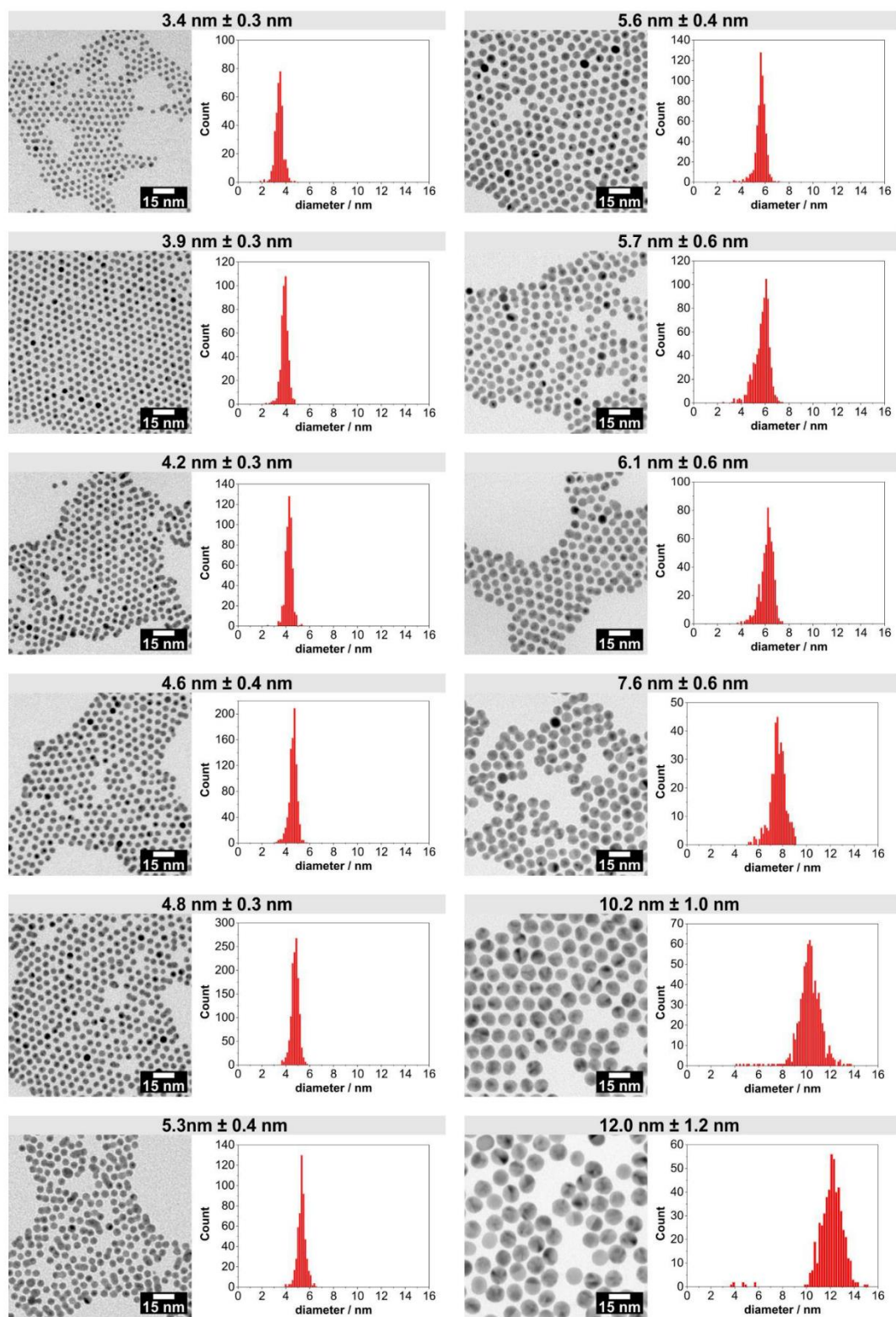TEM overviews and size distributions of the used Au NC samples are shown in Figure S3.

3

Fig. S3: TEM images of the used gold nanocrystals of various sizes in combination with their respective size histograms.

4

The extinctions of the respective LSPR maxima depending on the nanoparticle concentration are presented in Figure S4.
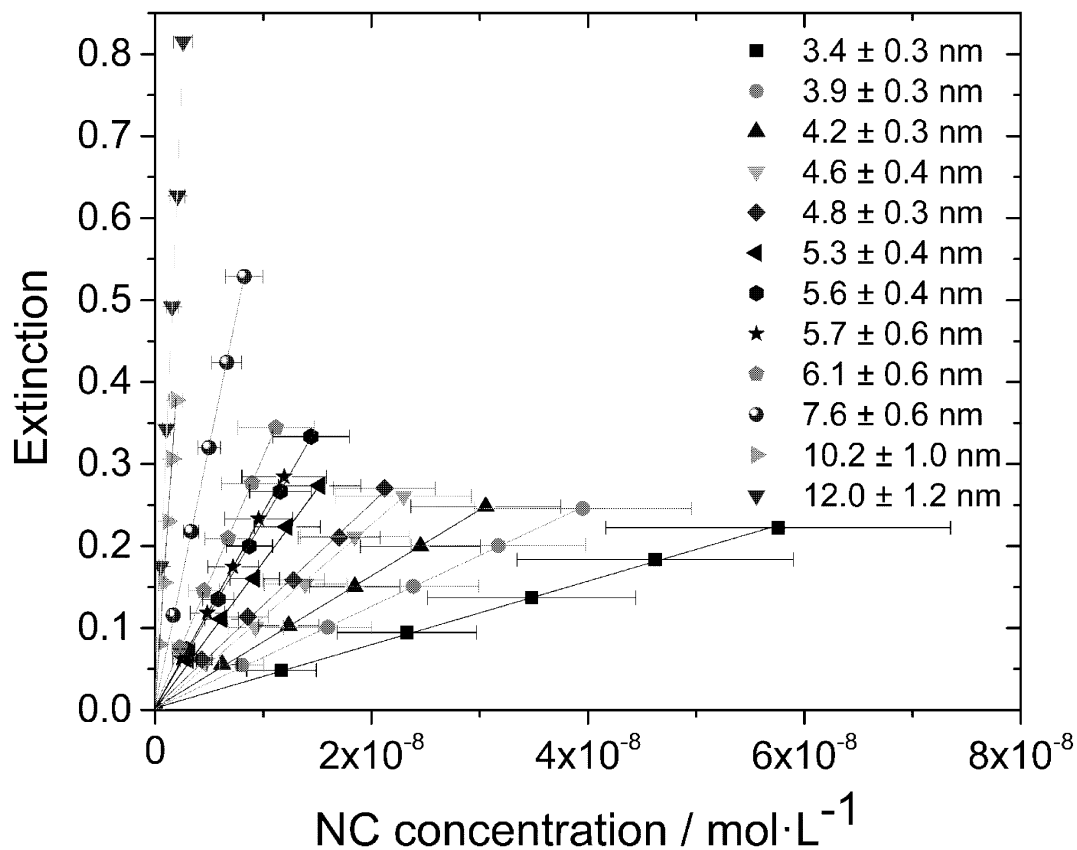

Fig. S4: Extinctions of quasi-spherical oleylamine-stabilized gold nanocrystals of different sizes and nanocrystal concentrations in toluene. The extinctions were measured in quartz-glass cuvettes with 10 mm path length. The error bars originate from the standard deviation of the nanocrystal diameters and the calculated particle concentrations via Au mass concentrations.

The thusly-determined values for ε are summarized in Table S2.

Tab. S2: Values of the experimentally determined diameter, extinction coefficient and the respective standard deviation of quasi-spherical oleylamine-stabilized gold nanocrystals in toluene.

d / nm	Δd / nm	λ_{max} / nm	ε / L·mol^{-1}·cm^{-1}	$\Delta\varepsilon$ / L·mol^{-1}·cm^{-1}
3.4	0.3	511	$3.8731 \cdot 10^6$	50463
3.9	0.3	514	$6.2127 \cdot 10^6$	62522
4.2	0.3	515	$8.052 \cdot 10^6$	84737
4.6	0.4	517	$1.1313 \cdot 10^7$	213139
4.8	0.3	517	$1.2442 \cdot 10^7$	278648
5.3	0.4	518	$1.7919 \cdot 10^7$	314707
5.6	0.4	521	$2.288 \cdot 10^7$	245162
5.7	0.6	521	$2.3845 \cdot 10^7$	258501
6.1	0.6	525	$3.0561 \cdot 10^7$	336926
7.6	0.6	527	$6.8912 \cdot 10^7$	549612
10.2	1.0	529	$1.956 \cdot 10^8$	$1.0386 \cdot 10^6$
12.0	1.2	529	$3.0812 \cdot 10^8$	$6.5007 \cdot 10^6$

5

A comparison of the experimentally identified extinction coefficients of Au NCs of different sizes with existing literature is shown in Figure S5. The new set of data fits in nicely. A linear dependence of the molar extinction coefficient on the particle diameter is found in logarithmic coordinates. The slope of a linear fit to the results of oleylamine-stabilized Au NCs in toluene of this work has a value of 3.53 ($R^2 = 0.9992$) compared to 3.99 for dodecanethiol-stabilized nanoparticles and 3.32 for particles in an aqueous environment in recent literature [1,2].
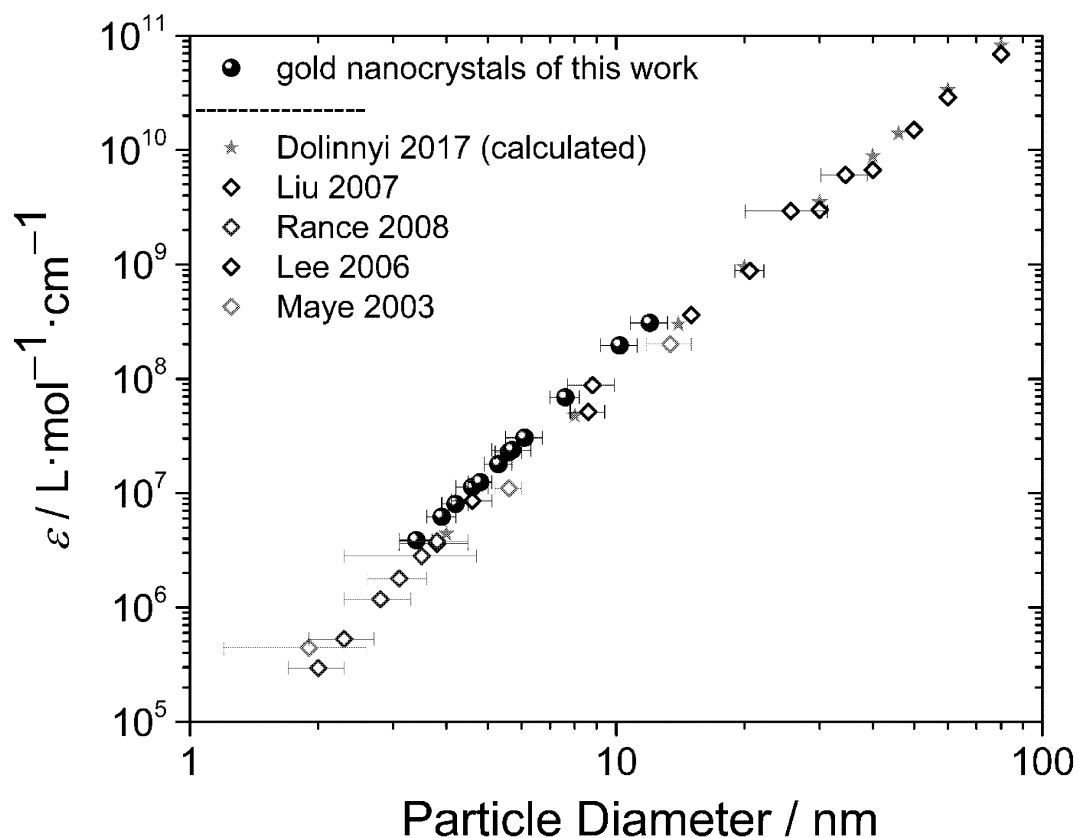
Fig. S5: Comparison of the experimental determined Au extinction coefficient of this work with previously published measured and simulated data [1–5].

Au-Ni$_3$S$_2$ Core-Shell Particles

TEM micrographs and size histograms of the synthesized Au-Ni$_3$S$_2$ core-shell particles are presented in Figure S6.

6
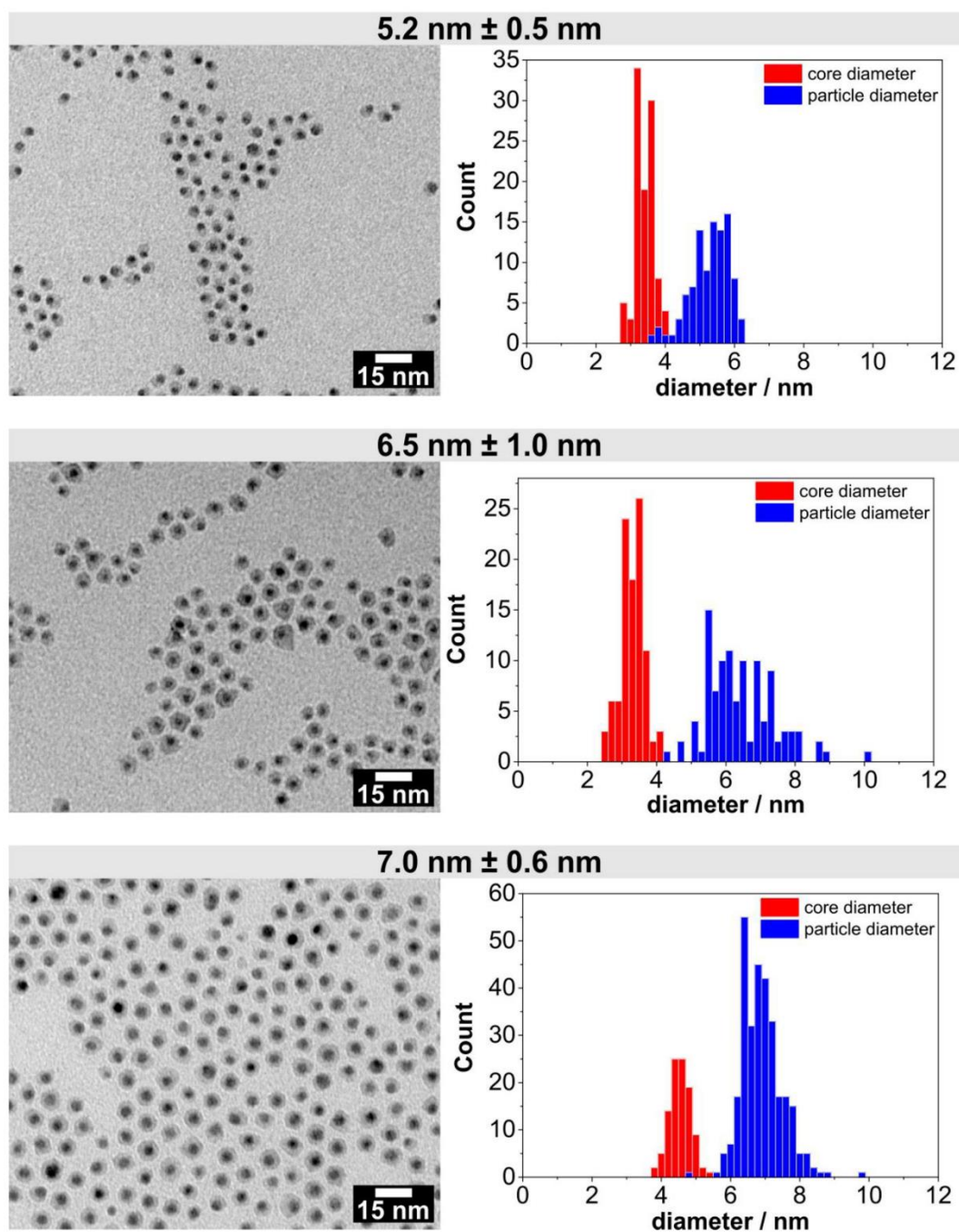
Fig. S6: TEM images and correlating size distributions of the investigated $Au-Ni_3S_2$ core-shell nanoparticles.

The extinction of the respective LSPR maxima depending on the nanoparticle concentration can be seen in Figure S7.
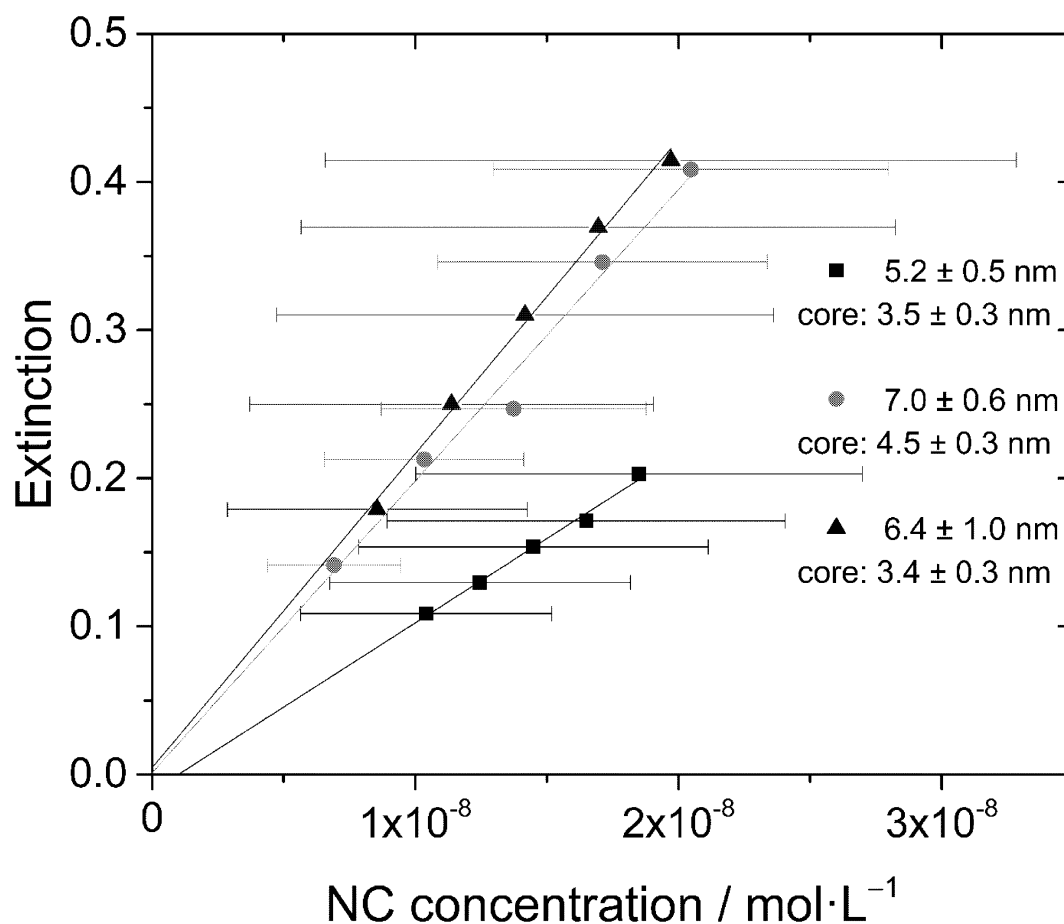
7

Fig. S7: Extinction at the LSPR maximum depending on the core-shell particle concentration in toluene. The measurements were conducted using 10 mm quartz-glass cuvettes while the error bars were determined by considering the influence of the standard deviation of the particle diameter on the particle concentration via the measured Ni mass concentrations.

The values for the molar extinction coefficient of the particles are presented in Table S3.

Tab. S3: Extinction coefficients of the investigated Au-Ni$_3$S$_2$ nanoparticles in toluene.

d / nm	Δd / nm	λ_{max} / nm	ε / L·mol^{-1}·cm^{-1}	$\Delta\varepsilon$ / L·mol^{-1}·cm^{-1}
5.2	0.5	426	1.1375·10^7	604397
6.5	1.0	459	2.1212·10^7	905186
7.0	0.6	471	1.9683·10^7	1.4945·10^6

References

1.   G. A. Rance, D. H. Marsh, A. N. Khlobystov, Chem. Phys. Lett. **460** (2008) 230.

2.   X. Liu, M. Atwater, J. Wang, Q. Huo, Colloids Surfaces B Biointerfaces **58** (2007) 3.

3.   A. I. Dolinnyi, Colloid J. **79** (2017) 611.

4.   K. S. Lee, M. A. El-Sayed, J. Phys. Chem. B **110** (2006) 19220.

5.   M. M. Maye, L. Han, N. N. Kariuki, N. K. Ly, W. Ben Chan, J. Luo, C. J. Zhong, Anal. Chim. Acta **496** (2003) 17.

3 Synthesis of Hollow Nickel Sulfide Nanocrystals

3.1 Summary

After nickel sulfide nanostructures have been established as a promising plasmonic material with similar optical properties to noble metal nanoparticles, the need to further improve the range of obtainable particle geometries and shapes arises. As explained in chapter 1.2.4, hollow plasmonic nanoparticles exhibit optical properties which are ideal for several types of applications. Especially in sensors, the higher sensitivity of the LSPR maximum towards the particles' surroundings is important to achieve an optimal sensing material. Hence, the goal of chapter 3.2 was to synthesize hollow nickel sulfide nanoparticles and to evaluate their optical properties. As mentioned in chapter 1.3.3, there are several ways to obtain hollow nanostructures. However, in the case of nickel sulfide, methods such as chemical etching or galvanic replacement reactions, which are very commonly used to produce hollow noble metal nanoparticles, are not easily applicable. Hence, the chosen route was to first synthesize nickel nanoparticles and then convert them to hollow nickel sulfide structures *via* the nanoscale Kirkendall effect. This was achieved successfully for nickel oxide and nickel phosphide in the literature.

It was quickly found that the results of the chosen nickel synthesis are very dependent on the number of halide ions present in the reaction solution leading to completely amorphous nanoparticles when none are present or fully crystalline particles when a lot of halide ions are used. In between, the size of the crystalline areas inside the nickel nanoparticles can be readily controlled by varying the halide ion concentration. Since the nanoscale Kirkendall effect is only possible in crystals, this way the size of the obtained cavities inside the particles could in turn also be tuned. This could be shown

in great detail in the case of the more commonly known nickel phosphide system. Amorphous nickel particle regions were simply converted to nickel phosphide while crystalline nickel underwent the Kirkendall effect forming cavities. This knowledge was then applied to the nickel sulfide synthesis, resulting in hollow nickel sulfide nanoparticles when fully crystalline nickel precursor particles were used. The obtained sulfide material showed a very narrow LSPR band compared to the one exhibited by the nickel sulfide nanoparticles discussed previously. This was attributed to the improved crystallinity of the Kirkendall product which could be a reason for a smaller damping constant of their respective LSPR. Additionally, it was found that the obtained nickel sulfide phase could be varied by using different sulfur precursors during the synthesis.

3.2 Halide Ion Influence on the Formation of Nickel Nanoparticles and their Conversion into Hollow Nickel Phosphide and Sulphide Nanocrystals

Rasmus Himstedt, Dominik Hinrichs, Joachim Sann, Anica Weller, Georg Steinhauser, and Dirk Dorfs

Nanoscale

Check for updates

Halide ion influence on the formation of nickel nanoparticles and their conversion into hollow nickel phosphide and sulphide nanocrystals†

Rasmus Himstedt,[a] Dominik Hinrichs,[a] Joachim Sann,[b,c] Anica Weller,[d] Georg Steinhauser [ID][d] and Dirk Dorfs [ID] *[a,e]

A dependence of the formation of tri-*n*-octylphosphine-capped Ni nanocrystals on the presence of halide ions during their synthesis is shown. For the application-oriented synthesis of Ni particles, this information can be crucial. Furthermore, Ni nanoparticles can be converted to nickel phosphide or sulphide by heating them up in the presence of a phosphorus or sulphur source, resulting in either solid or hollow nanocrystals, formed *via* the nanoscale Kirkendall effect, depending on the synthesis route. By adjusting the Ni crystallite size in the initial nanoparticles *via* the halide ion concentration the cavity size of the resulting hollow nanocrystals can be tuned, which is otherwise impossible to realise for particles of a similar total diameter by using this process. The synthesised hollow Ni_5S_2 nanocrystals exhibit a much sharper localised surface plasmon resonance (LSPR) band than all previously presented particles of this material, which is known to show molar extinction coefficients at the LSPR maximum similar to Au. This narrow linewidth could be explained by the nanoparticles' high crystallinity resulting from the Kirkendall process and is interesting for various possible optical applications such as surface-enhanced Raman spectroscopy owing to the low cost of the involved materials compared to the widely used noble metals.

Introduction

Nickel nanoparticles are currently attracting considerable interest due to their exceptional mechanical and magnetic properties.[1,2] Since it is important to meticulously control the crystallinity of the produced particles in order to reliably achieve these properties, the typical Ni nanoparticle synthesis procedures have been investigated thoroughly recently.[3,4] It is possible to synthesise various shapes of crystalline Ni nanostructures such as rods, platelets and nanocubes.[5-8] However,

especially when phosphines like tri-*n*-octylphosphine (TOP), which is widely used as a capping agent for Ni nanoparticles, are present during the synthesis it can be observed that the crystallinity of the product varies and an amorphous product, consisting at least partially of nickel phosphide, is obtained depending on the reaction conditions.[9,10] So far it has for example been shown that if hydrogen gas is used as the reducing agent no amorphous particles were obtained even if phosphines were present.[8,11]

The influence of halide ions on the Ni nanocrystal formation in the presence of phosphines has however yet to be studied in detail even though for numerous other types of nanoparticle syntheses this parameter has been found to be crucial in recent years.[12,13] It is, for example, essential for the crystallisation of nanoparticles consisting of elemental metals like iron. Zhang *et al.* obtained either amorphous or crystalline Fe nanoparticles depending on the presence or absence of chloride ions during their synthesis.[14] In this work, using a slightly modified version of the basic synthesis route by Carenco *et al.* a dependence of the Ni crystallisation on the presence of halide ions, which is similar to that of the Fe system, is shown.[15] With this knowledge, it is possible to fine-tune the crystallinity of the produced Ni nanoparticles from amorphous to partially or fully crystalline just by varying the halide ion concentration in the colloidal synthesis. The reason

[a]*Institute of Physical Chemistry and Electrochemistry, Leibniz Universität Hannover, Callinstraße 3A, 30167 Hannover, Germany. E-mail: dirk.dorfs@pci.uni-hannover.de*
[b]*Center for Materials Research (LaMa), Justus Liebig University Giessen, Heinrich-Buff-Ring 16, 35392 Gießen, Germany*
[c]*Institute of Physical Chemistry, Justus Liebig University Giessen, Heinrich-Buff-Ring 17, 35392 Gießen, Germany*
[d]*Institute of Radioecology and Radiation Protection, Leibniz Universität Hannover, Herrenhäuser Straße 2, 30419 Hannover, Germany*
[e]*Cluster of Excellence PhoenixD (Photonics, Optics, and Engineering – Innovation Across Disciplines), Hannover, Germany*

Nanoscale

for the different degrees of crystallinity in this case however is likely a large quantity of phosphorus (up to 15 atomic%) which is incorporated into the amorphous particles during their synthesis resulting in the formation of nickel phosphide.

Furthermore, these nanoparticles can be converted to crystalline nickel phosphide particles by heating them up in the presence of a phosphorus source.[16] Nickel phosphides have recently been intensively studied due to their various possible applications as an electrocatalyst in water-splitting reactions or as the catalyst for upgrading reactions of bio-oil compounds.[17,18] The resulting nanocrystals can turn out solid or hollow depending on the chosen synthesis conditions. This study shows that the cavity size, as well as the obtained nickel phosphide phase, can also be directly controlled *via* the halide ion concentration. Amorphous, phosphorus-containing particles are converted to solid nickel phosphide crystals while previously crystalline Ni nanoparticles form hollow nanocrystals undergoing a nanoscale Kirkendall process. Transferred to heterostructures this control over the diameter of the cavities could also be interesting for applications relying on particle–particle interactions like key-lock processes, which have been demonstrated to happen on the nanoscale recently.[19]

The synthesis of hollow particles *via* the Kirkendall effect has moreover been demonstrated in case of the conversion of Ni nanoparticles to nickel oxide.[20] Thus, in this study, it is investigated whether this can be adapted to the nickel sulphide system as well. Nanostructures of the sulphide phases Ni_3S_2 (heazlewoodite) and Ni_3S_4 (polydymite) have recently been shown to exhibit localised surface plasmon resonances (LSPRs) in the visible regime of the electromagnetic spectrum with considerable molar extinction coefficients, which only a selected group of materials, mostly consisting of noble metal nanoparticles, are known to do.[21,22] The presented results show that it is indeed possible to obtain hollow nanocrystals of the aforementioned nickel sulphide phases by altering the synthesis conditions slightly. Due to their larger size and more importantly their high crystallinity resulting from the Kirkendall process, the LSPR of these nanoparticles has a narrow linewidth compared to the previously known particles of these materials.

Results and discussion

Ni nanoparticles with a diameter of roughly 16–23 nm were produced *via* the thermal decomposition of nickel acetyl-acetonate ($Ni(acac)_2$) in tri-*n*-octylphosphine oxide (TOPO, solvent) in the presence of tri-*n*-octylphosphine (TOP), oleylamine (OLAm) and varying amounts of halide ions. In the following, the used quantity of halide atoms is always noted as a percentage in relation to the number of Ni atoms (20% Cl⁻ for example means that the amount of Cl atoms is 0.2 times the amount of Ni atoms in the synthesis).

Fig. 1 shows high-resolution transmission electron microscopic (HR-TEM) brightfield images of representative nanoparticles produced in the presence of varying quantities of
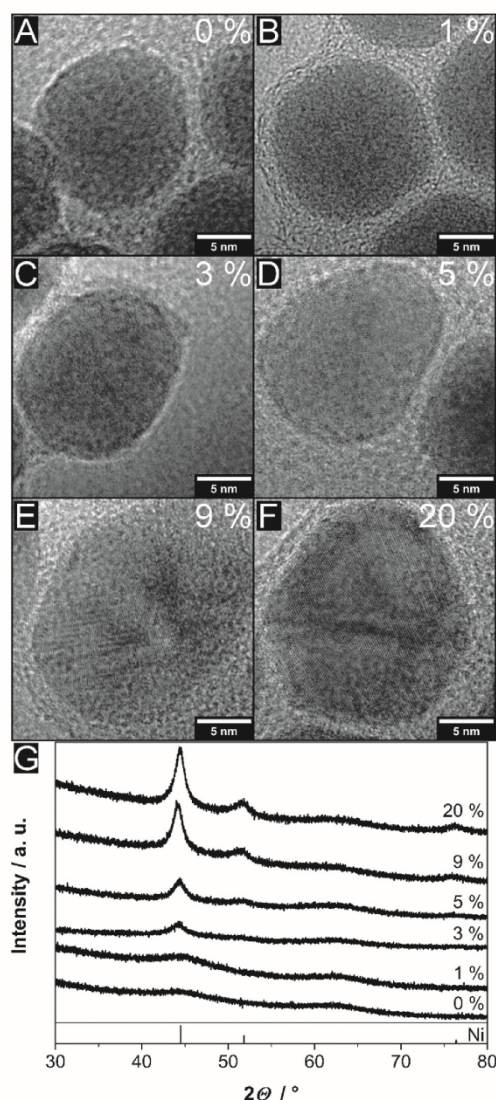

Fig. 1 High resolution TEM micrographs of nanoparticles synthesised by employing (A) 0%, (B) 1%, (C) 3%, (D) 5%, (E) 9% and (F) 20% chlorine atoms relative to nickel during the synthesis. It can be seen how the size of crystalline regions increases with larger amounts of chloride ions present. The average diameters of the shown nanoparticles are 16.3 ± 1.0 nm (A), 16.5 ± 0.7 nm (B), 16.9 ± 2.8 nm (C), 17.6 ± 1.7 nm (D), 20.0 ± 1.8 nm (E) and 22.4 ± 1.8 nm (F), respectively. TEM overview images of the respective samples can be found in Fig. S1 (ESI†). (G) X-ray diffraction patterns of the respective nanoparticle samples. While the particles are almost completely X-ray-amorphous without any chloride ions the nickel (PDF card #: 01-087-0712) crystallite size steadily increases with their concentration.

chloride ions, which are provided *via* the addition of tetradodecylammonium chloride (TDAC) to the synthesis mixture. TEM images with a lower magnification can be found in Fig. S1 in the ESI.† TDAC was chosen as the chloride precursor because it decomposes under the reaction conditions and also due to the size and therefore supposedly inactive nature of the formed cation. It can be seen that with 0% Cl⁻ only spherical and apparently completely amorphous particles are obtained, while with an increasing Cl⁻ amount larger and larger crystalline areas are visible in the nanoparticles until they appear to be fully crystalline at 9% Cl⁻. Additionally, a low contrast shell around the particles, which consists of organic byproducts, can be observed.[23] In order to further investigate the crystallinity and phase of the nanoparticles, X-ray diffraction (XRD) measurements were conducted. The results are shown in Fig. 1G. It is obvious that the produced nanoparticles consist of nickel crystallites with a face-centred cubic lattice which increase in size and therefore induce sharper and more intense X-ray reflections when larger amounts of Cl⁻ ions are present. Additionally, the total diameter of the nanoparticles increases at a much lower rate (see Fig. S1 in the ESI†). In case of the synthesis without any chloride, only a very broad reflection, which corresponds to the Ni (1 1 1) lattice planes, at around 45°2θ can be seen. This confirms the amorphous nature of the respective nanoparticles observed during the TEM analysis. To investigate the composition of the X-ray amorphous particles three additional analysis methods were used. Selected area electron diffraction (SAED) measurements were performed as well as X-ray photoelectron spectroscopy (XPS) and inductively coupled plasma mass spectrometry (ICP-MS, see Fig. S2 in the ESI†). The results of the SAED and Ni 2p XPS experiments are typical for TOP-capped Ni nanoparticles.[23,24] However, a certain level of phosphorus doping in the Ni particles which cannot be detected by these methods is possible.[9,10,25] Indeed, P 2p XPS spectra and ICP-MS measurements show that there is a large amount of P (Ni/P molar ratio of 3.28) present in the sample containing the amorphous particles and that about 60% of the P consists of nickel phosphide, meaning that in this case, 15% of the atoms inside the particles consist of phosphorus. However, the more chloride is present during the synthesis the more the P content and the phosphide fraction thereof decreases (see Table S1 in the ESI†).

Various control experiments prove that the chloride ions are indeed the species which causes the different degree of crystallinity of the synthesised nanoparticles (see Fig. S4, S5 and their discussion in the ESI†).

Another factor which influences the growth process and final size of the obtained nanoparticles is the concentration of phosphines (TOP in this case) in the reaction mixture.[1,11,26,27] In order to ensure good comparability of all the investigated samples the TOP amount was therefore kept constant for all discussed experiments.

Furthermore, TDAC was replaced by tetradodecylammonium bromide (TDAB) to investigate whether the crystallisation of Ni can also be induced by bromide ions. TEM and XRD analysis show, that the results are again very similar (see Fig. S6 in the ESI†). Analogously to the Cl⁻ system, by introducing 5% Br⁻ to the synthesis partly crystalline particles are obtained while in case of 20% Br⁻ completely crystalline Ni nanoparticles are the result. The size of the obtained nanoparticles is also almost identical.

Additionally, OLAm of different purities and therefore different amounts of OLAm (see Fig. S7 and S8 in the ESI†) and a different solvent (1-octadecene instead of TOPO, see Fig. S9 in the ESI†) were employed in reference experiments to provide a better comparability of the presented results to the established literature on this type of synthesis of Ni nanoparticles.[4,15] In all investigated cases the obtained particles turned out to be amorphous without the addition of halide ions during the synthesis, while crystalline Ni nanoparticles were produced in their presence. Compared to the work by Carenco *et al.* who report a crystalline product in the absence of halide ions using pure OLAm as the solvent, the only difference of the synthesis conditions is a dilution of the reactants due to the addition of a solvent.[15] Only this dilution reveals the significant effect of halide ions on the Ni system. Furthermore and in accordance with their results, the total diameter of the Ni nanoparticles produced in this study decreases slightly when more OLAm is used. The difference between the nanoparticles synthesised in 1-octadecene and TOPO, on the other hand, is negligible (see Fig. S9†). The reason for using TOPO, which itself cannot act as a phosphorus source for the formation of nickel phosphide, is the better solubility of the particles in this solvent and the narrower size distribution of the synthesised nanoparticles.[16] Overall, the type of solvent does not seem to have a noticeable influence on the crystallinity of the Ni nanoparticles. The large amount of phosphorus contained in these particles, which leads to their amorphous character, most likely instead originates predominantly from the used TOP which, in contrast to the more stable TOPO, was present in all investigated syntheses.

Thus, it can be concluded that halide ions facilitate the crystallisation of TOP-capped fcc-Ni possibly in a way similar to the Fe nanoparticle system.[14] In the latter case, the presence of halide ions leads to the thermodynamically favoured growth of bcc-Fe nanocrystals instead of the kinetically favoured formation of amorphous Fe particles due to a larger critical radius for the nuclei caused by the ability of the halide to form complexes with metal ions and therefore dissolve the formed clusters.[14] The difference in the Ni system is however that instead of forming pure amorphous Ni nanoparticles, the kinetic control of the reaction leads to the incorporation of large amounts of P into the particles which in turn lead to their amorphous nature due to the emergence of areas of nickel phosphide. Yet, also in this case halide ions are probably able to dissolve these clusters in their *status nascendi* more easily than the presumably more thermodynamically stable crystalline Ni seeds which are therefore preferably formed in their presence. This reduction of the total number of formed stable seeds is most likely also responsible for the

increased size of the nanoparticles synthesised in the presence of halide ions. Alternatively, the halide ions could function as a ligand in a reaction similar to a disproportion reaction as proposed recently.[3] However, in contrast to the tendencies observed in the respective study there does not seem to be a noticeable difference between the outcomes of the additions of chloride and bromide ions in the results presented here.

The as-prepared Ni particles can be converted into nickel phosphide by further heating and annealing at higher temperatures (here 300 °C) with TOP acting as the phosphorus source.[16,28,29] HR-TEM images and XRD patterns of the so treated nanoparticles can be seen in Fig. 2 (for TEM overview images of the shown samples see Fig. S10 in the ESI†). All samples consist of highly crystalline nickel phosphide particles. Yet, it is obvious that solid particles are obtained in the absence of chloride while chloride ions lead to the formation of voids inside the nanocrystals. In combination with the results shown in Fig. 1, it can be concluded that previously crystalline regions in the Ni nanoparticles undergo a Kirkendall process and are therefore forming cavities while this process is impossible in case of amorphous precursor particles. The obtained nickel phosphide phase is $Ni_{12}P_5$ for low chloride amounts while in case of increasing chloride concentrations more and more Ni_2P is formed. One reason for this could be the low energy diffusion of P through Ni_2P.[30] The more efficient diffusion of P through this nickel phosphide phase could compete with the usually faster diffusion of Ni resulting in the preferred formation of Ni_2P compared to other phases such as $Ni_{12}P_5$. Additionally, since the P content of the Ni nanoparticles decreases with an increasing amount of used chloride, the formation of Ni_2P as the phase with a smaller Ni/P ratio could be favoured in these cases. Interestingly, also the type of halide precursor seems to have an influence on the obtained nickel phosphide phase. In the case of CTPM $Ni_{12}P_5$ can be observed exclusively while using TDAB leads to larger amounts of Ni_2P (see Fig. S4 and S6,† respectively). These two phases are generally the most likely products of this kind of synthesis while so far the synthetic lever to obtain phase pure products has been the ratio of P to Ni, the reaction temperature or time and the amount of OLAm used.[18,31,32]

Ultimately, the observed dependence of the phosphide crystallisation on the halide ion amount, which was reproduced via several of the aforementioned reference experiments (see Fig. S4, S6, and S7 in the ESI†), makes it possible to tune the size of the voids via the used halide ion concentration. In Fig. 3 its influence on the particle diameter before and after the crystallisation as well as on the resulting cavity size is summarised. It can be easily seen that while the chloride concentration does also affect the total size of the produced nanoparticles, which is probably due to a larger critical nucleation radius, the respective dependence of the void diameters is much stronger. For low halide concentrations, their size increases drastically while the total diameter of the nanoparticles stays more or less constant. For chloride amounts of above 5%, the Kirkendall process seems to be almost quantitative and the further cavity size increase is likely caused by
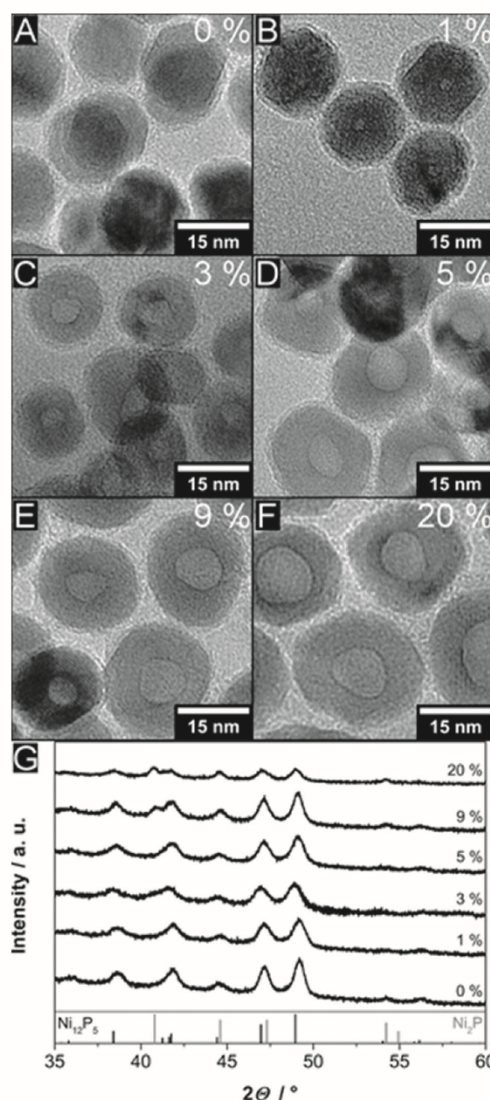

Fig. 2 High resolution TEM images of nickel phosphide nanoparticles produced by heating the previously shown Ni particles to 300 °C in the presence of TOP and (A) 0%, (B) 1%, (C) 3%, (D) 5%, (E) 9% and (F) 20% chlorine atoms relative to Ni. While solid single nanocrystals are obtained without any chloride ions, increasingly large cavities can be seen in case of larger concentrations, resulting from a nanoscale Kirkendall process. (G) X-ray diffraction patterns of the respective nanoparticle samples. The obtained crystal phase for low chloride ion concentrations is the $Ni_{12}P_5$ phase (PDF card #: 01-074-6017), while in case of high chloride amounts an increasing amount of Ni_2P (PDF card #: 00-003-0953) can be observed.
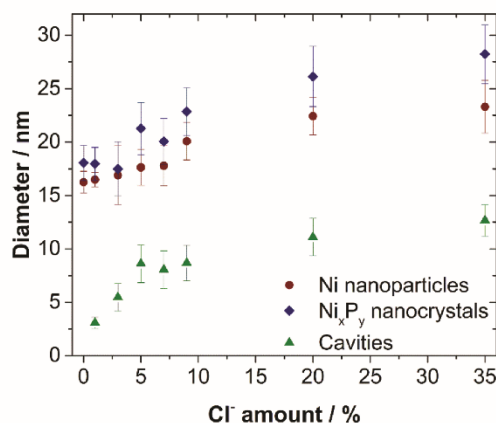
Paper

Nanoscale

Fig. 3 Dependence of the diameter of nickel nanoparticles, the corresponding nickel phosphide nanocrystals and their inner cavity on the number of chloride ions relative to nickel atoms present during their synthesis. The error bars correspond to the standard deviations of the measured diameters. It can be seen that the overall particle size is slightly increased with larger amounts of the halide. Especially in case of low chloride concentrations however, the cavity size shows a much stronger correlation due to the strong dependence of the nickel crystallinity on the presence of the halide.

the accompanying increase in the total Ni nanoparticle diameter.

To investigate whether the above findings are also applicable to the nickel sulphide system, 1-dodecanethiol (DDT) was introduced into the synthesis as a sulphur precursor and the reaction temperature was reduced to 225 °C, which is the usual reaction temperature for the synthesis of Ni_3S_2 (heazlewoodite) and Ni_3S_4 (polydymite) nanoparticles.[21] Crystalline nickel phosphide, on the other hand, is usually not formed at this temperature.[16] In Fig. 4A–C, TEM micrographs of the produced samples are presented. It can be seen that like in the nickel phosphide system solid nanocrystals are formed without halide ions while hollow particles are obtained in their presence. The respective XRD patterns are shown in Fig. 4E. Surprisingly, in the case of 0% chloride $Ni_{12}P_5$ is formed. At this temperature this could not be achieved without adding DDT, indicating that the thiol is somehow able to activate the crystallisation of the nickel phosphide from the amorphous phosphorus-containing precursor particles at a much lower temperature than usual. However, when a chloride precursor is added Ni_3S_2 is obtained as expected. For the sample with 40% chloride, this is proven by the XRD, while in the case of the 5% sample the crystalline areas within the particles are too small to lead to visible reflections. Yet, in a representative HR-TEM image (see Fig. 4D) the Ni_3S_2 lattice planes are clearly visible. However, there is likely still a non-negligible content of nickel phosphide present in the latter particles which could be a reason for the observed small crystallite size. The respective average diameters of the precursor nano-
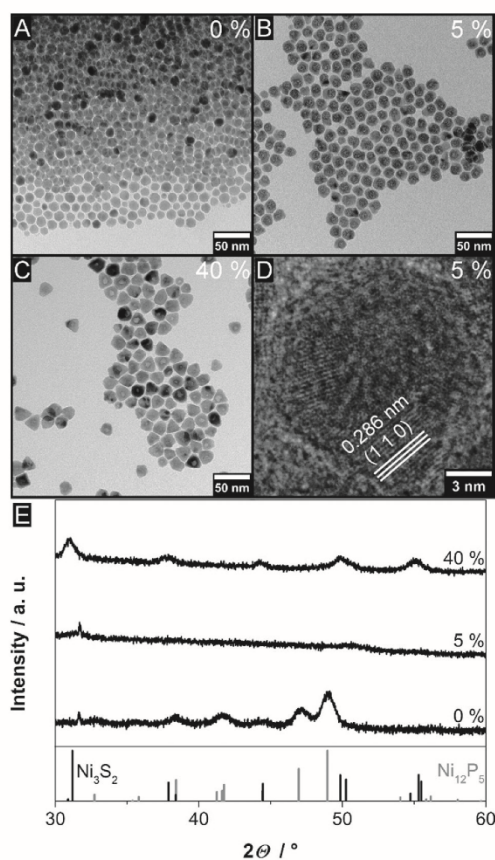

Fig. 4 TEM micrographs of nanoparticles produced by heating Ni particles to 225 °C in the presence of TOP, DDT and (A) 0%, (B) 5%, (C) 40% chlorine relative to Ni. Solid single nanocrystals are obtained without any chloride, while with an increasing amount of the halide the particles undergo a nanoscale Kirkendall effect. (D) High-resolution TEM image of a nanoparticle of the sample shown in (B). Lattice planes can be seen and were identified as the (1 1 0) planes of Ni_3S_2. (E) X-ray diffraction patterns of the presented nanoparticle samples. The obtained crystal phase for low chloride ion concentrations is the $Ni_{12}P_5$ phase (PDF card #: 01-074-6017), while in case of high chloride amounts Ni_3S_2 (PDF card #: 01-073-0698) is found. For the intermediary chloride concentration, no reflections can be observed in the XRD since the formed crystalline areas are too small.

particles as well as of the nickel sulphide nanocrystals and their inner cavities are similar to the previously shown phosphide particles and summarised in Fig. S11 (ESI†).

UV/vis/NIR absorbance spectra of the synthesised particles are shown in Fig. 5. While the spectrum of the solid nickel phosphide nanocrystals shows only a typical shoulder in the absorbance at around 500 nm (for the optical analysis of all the previously presented Ni and Ni_xP_y particles see Fig. S12 and S13,† respectively) the nickel sulphide nanoparticles exhibit an
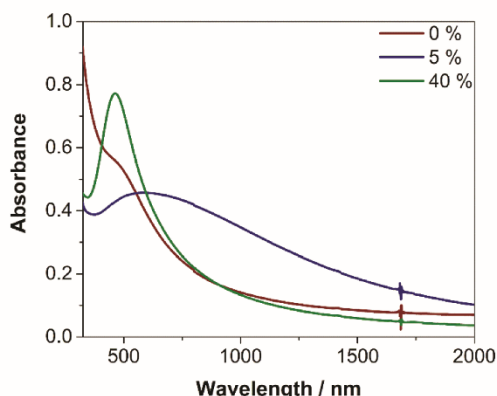
Fig. 5 UV/vis/NIR absorbance spectra of nanoparticles, which were crystallised in the presence of DDT and different chloride concentrations, in colloidal solution (toluene). It can be seen that with an increasing chloride amount an absorbance band at around 463 nm emerges, which can be attributed to the localised surface plasmon resonance of Ni_3S_2. In the case of the sample with 5% chloride, the LSPR experiences strong damping processes due to the polycrystalline nature of the nanoparticles.

absorbance band at around 463 nm which can be attributed to their localised surface plasmon resonance. Compared to previous works on plasmonic Ni_3S_2 nanoparticles the band appears at a longer wavelength and the LSPR linewidth is very narrow (full width at half maximum of roughly 200 nm compared to about 400 nm) which is most likely caused by the high degree of crystallinity of the synthesised particles due to the Kirkendall process and by their slightly larger size.[21,22]

Especially the absorbance feature of the sample with 40% chloride is very sharp. Compared to the polycrystalline 5% sample, which contains particles of a similar total diameter, or smaller Ni_3S_2 nanoparticles there is probably a lot less LSPR damping due to grain boundaries or crystal defects. This, therefore, enables the intense LSPR of the hollow nanocrystals.

It is also possible to produce hollow particles of different nickel sulphide phases by changing the sulphur precursor. If elemental sulphur dispersed in ODE is used instead of DDT hollow Ni_3S_4 nanoparticles are obtained (see Fig. S14 in the ESI†). However, in contrast to the presented Ni_3S_2 nanocrystals, these particles are polycrystalline and tend to agglomerate which leads to much broader LSPR linewidths (for a direct HR-TEM comparison of the different nickel sulphide nanoparticles see Fig. S15 in the ESI†).

Conclusions

It could be shown that the formation of TOP-capped nickel nanocrystals in colloidal solution depends on the presence of halide ions like chloride and bromide during the synthesis. Even in small amounts, the halides lead to the formation of

crystalline areas within otherwise amorphous nanoparticles which also contain a large amount of phosphorus. This knowledge is important for all applications and research involving this kind of colloidal Ni particles since their degree of crystallinity can strongly influence their magnetic or optical properties and also because nickel chlorides are commonly used as precursors. Additionally, this behaviour was used to tune the size of the cavities formed within nickel phosphide and sulphide nanocrystals through a nanoscale Kirkendall effect. By the nature of this process, the diameter of these voids can otherwise not be adjusted without changing the overall size of the whole nanoparticle. This could be interesting for potential applications relying on exact cavity sizes like key–lock interactions between different nanoparticles. Also, the hollow Ni_3S_2 nanoparticles, which were synthesised for the first time on this size scale, show very promising optical properties. Their LSPR linewidth is much narrower than the one of previously known nickel sulphide nanostructures, which already show a molar extinction coefficient at the LSPR maximum, which is comparable to the values of nanoparticles consisting of noble metals like Au.[22] Thus, the presented nickel sulphide material could be a suitable low-cost alternative for the applications of plasmonic nanomaterials active in the visible regime of the electromagnetic spectrum.

Experimental section

Used chemicals

Chloroform (99%), Ni standard for AAS (1 g L^{-1}), 1-octadecene (90%, ODE), oleylamine (70%, OLAm), tetradodecylammonium bromide (99%, TDAB), tetradodecylammonium chloride (97%, TDAC), toluene (99.7%) and tri-n-octylphosphine oxide (99%, TOPO) were purchased from Sigma-Aldrich. Ethanol (99.8%) was purchased from Carl Roth. Nickel 2,4-pentanedionate (95%, $Ni(acac)_2$) was purchased from Alfa Aesar. Chlorotriphenylmethane (98%, CTPM), 1-dodecanethiol (98%, DDT), nickel chloride hexahydrate (99.9%, $NiCl_2 \cdot 6H_2O$) and tri-n-octylphosphine (97%, TOP) were purchased from abcr. Oleylamine (80–90%, OLAm) was purchased from Acros. Nitric acid trace select (69%, HNO_3) and P standard for AAS (1 g L^{-1}) were purchased from Fluka Analytical.

Synthesis of nickel nanoparticles

For the synthesis of Ni nanoparticles we used a modified version of an existing procedure by Carenco et al.[15] $Ni(acac)_2$ (0.1 g), TOPO (2.5 g), OLAm (80–90%, 1 mL), and a varying amount of a halide ion precursor (TDAC unless otherwise specified) were mixed in a 25 mL three-neck round-bottom flask. The mixture was degassed at 80 °C under vacuum for 2 h before TOP (0.175 mL) was added under an argon atmosphere. The reaction solution was subsequently heated up to 220 °C using a 20 °C min^{-1} heating ramp. After different time intervals samples (0.5 mL) were taken via a glass syringe. The usual total reaction time was 30 min. The samples were diluted with toluene (1 mL) and centrifuged (3000g, 10 min) after the

Paper

addition of ethanol (1 mL) before the synthesised nanoparticles were finally redispersed in toluene (1.5 mL).

Crystallisation of nickel phosphide nanoparticles

The produced nanoparticles were crystallised using a procedure similar to the two-step synthesis for nickel phosphide particles by Wang *et al.*[16] After the aforementioned 30 min at 220 °C the previously described reaction mixture was quickly heated up to 300 °C under argon atmosphere. Again samples (0.5 mL) were taken after different time intervals and the reaction was usually stopped after 30 min. The samples were purified by centrifugation (3000g, 10 min) after the addition of toluene (1 mL) and ethanol (1 mL) and the nanocrystals were redispersed and stored in toluene (1.5 mL).

Crystallisation of nickel sulphide nanoparticles

Nickel sulphide nanocrystals were synthesised analogously to the previously described nickel phosphide particles with the important distinctions of different amounts of $NiCl_2\cdot6H_2O$ substituting $Ni(acac)_2$ being the halide ion source and DDT (0.45 mL), which was added to the reaction mixture after heating up. Furthermore, the reaction temperature was reduced from 300 to 225 °C. Again, samples were taken after different times. They were purified in the same way as the nickel phosphide nanoparticles and then stored under inert conditions.

Electron microscopy

Transmission electron microscopy was performed using a Fei Tecnai G2 F20 electron microscope with a field emission gun operated at 200 kV. The nanoparticles were purified by the addition of ethanol and subsequent centrifugation (14 000g, 5 min). Then they were dispersed in chloroform and 10 µL of the resulting solution were drop-casted onto a carbon-coated copper grid (300 mesh) by Quantifoil.

Elemental analysis

In order to determine the mass concentrations and the present element ratios of the particle dispersions inductively coupled plasma mass spectrometry measurements were done using an Agilent 8900 mass spectrometer coupled to an autosampler SPS 4 by Agilent Technologies with the software MassHunter. For this, different aliquots of the nanoparticle samples were taken and the solvent was evaporated. The resulting precipitate was subsequently dissolved in nitric acid, further diluted with Milli-Q water in order to reach suitable mass concentrations for the respective measurement and finally measured against calibration standard solutions with known mass concentrations using a nebuliser type MicroMist. The Ni measurements were done in a collision cell using the gas modus with a helium gas flux of 1 mL min^{-1} due to the high concentrations while P was measured in normal mode.

Optical spectroscopy

UV/vis/NIR absorbance spectra were measured using a Cary 5000 spectrophotometer by Agilent Technologies in transmission mode. The samples were diluted with toluene and placed in a quartz glass cuvette (1 cm path length). In case of the nickel sulphide samples, this was done under an inert atmosphere.

X-ray diffraction

X-ray diffraction measurements were conducted employing a Bruker D8 Advance device in reflection mode. It was operated at 40 kV and 40 mA using Cu K-alpha radiation. The samples were purified analogously to the preparation for the TEM analysis. The nanoparticle dispersions in chloroform were then drop-casted onto and dried on a single crystalline silicon sample holder.

X-ray photoelectron spectroscopy

X-ray photoelectron spectroscopy measurements were conducted in a PHI Versaprobe II Scanning ESCA Microprobe (Physical Electronics) using a monochromatised Al K_α X-ray source (beam diameter 200 µm, X-ray power of 50 W). The analyser pass energy for detail spectra was set to 23.5 eV with a step time of 50 ms and a step size of 0.2 eV. During measurement, the sample was flooded with slow electrons and argon ions using the built-in ion sputter and electron guns in order to compensate surface charging effects. Data evaluation was performed using CasaXPS software. For the charge correction, the energy of the C 1s-line was set to 284.8 eV. The samples were prepared by iterative drop-casting of sample dispersions, which were cleaned analogously to the TEM and XRD sample preparations, on a 4 mm × 4 mm glass substrate.

Conflicts of interest

There are no conflicts to declare.

Acknowledgements

References

1 T. Ishizaki, K. Yatsugi and K. Akedo, *Nanomaterials*, 2016, **6**, 172.

2 A. Sharma, J. Hickman, N. Gazit, E. Rabkin and Y. Mishin, *Nat. Commun.*, 2018, **9**, 1–9.

3 A. Vivien, M. Guillaumont, L. Meziane, C. Salzemann, C. Aubert, S. Halbert, H. Gérard, M. Petit and C. Petit, *Chem. Mater.*, 2019, **31**, 960–968.

4 S. Carenco, S. Labouille, S. Bouchonnet, C. Boissière, X. F. Le Goff, C. Sanchez and N. Mézailles, *Chem. – Eur. J.*, 2012, **18**, 14165–14173.

5 N. Cordente, M. Respaud, F. Senocq, M.-J. Casanove, C. Amiens and B. Chaudret, *Nano Lett.*, 2001, **1**, 565–568.

6 Y. Leng, Y. Zhang, T. Liu, M. Suzuki and X. Li, *Nanotechnology*, 2006, **17**, 1797–1800.

7 Y. Leng, Y. Li, X. Li and S. Takahashi, *J. Phys. Chem. C*, 2007, **111**, 6630–6633.

8 A. P. Lagrow, B. Ingham, S. Cheong, G. V. M. Williams, C. Dotzler, M. F. Toney, D. A. Jefferson, E. C. Corbos, P. T. Bishop, J. Cookson and R. D. Tilley, *J. Am. Chem. Soc.*, 2012, **134**, 855–858.

9 L. M. Moreau, D.-H. Ha, C. R. Bealing, H. Zhang, R. G. Hennig and R. D. Robinson, *Nano Lett.*, 2012, **12**, 4530–4539.

10 L. M. Moreau, D.-H. Ha, H. Zhang, R. Hovden, D. A. Muller and R. D. Robinson, *Chem. Mater.*, 2013, **25**, 2394–2403.

11 A. P. Lagrow, B. Ingham, M. F. Toney and R. D. Tilley, *J. Phys. Chem. C*, 2013, **117**, 16709–16718.

12 F. Gerdes, E. Klein, S. Kull, M. M. Ramin Moayed, R. Lesyuk and C. Klinke, *Z. Phys. Chem.*, 2018, **232**, 1267–1280.

13 S. Ghosh and L. Manna, *Chem. Rev.*, 2018, **118**, 7804–7864.

14 S. Zhang, G. Jiang, G. T. Filsinger, L. Wu, H. Zhu, J. Lee, Z. Wu and S. Sun, *Nanoscale*, 2014, **6**, 4852–4856.

15 S. Carenco, C. Boissière, L. Nicole, C. Sanchez, P. Le Floch and N. Mézailles, *Chem. Mater.*, 2010, **22**, 1340–1349.

16 J. Wang, A. C. Johnston-Peck and J. B. Tracy, *Chem. Mater.*, 2009, **21**, 4462–4467.

17 M. Zhou, Y. Kang, K. Huang, Z. Shi, R. Xie and W. Yang, *RSC Adv.*, 2016, **6**, 74895–74902.

18 S. E. Habas, F. G. Baddour, D. A. Ruddy, C. P. Nash, J. Wang, M. Pan, J. E. Hensley and J. A. Schaidle, *Chem. Mater.*, 2015, **27**, 7580–7592.

19 D. Hinrichs, R. Himstedt and D. Dorfs, *Nanoscale*, 2018, **10**, 9899–9907.

20 J. G. Railsback, A. C. Johnston-Peck, J. Wang and J. B. Tracy, *ACS Nano*, 2010, **4**, 1913–1920.

21 R. Himstedt, P. Rusch, D. Hinrichs, T. Kodanek, J. Lauth, S. Kinge, L. D. A. Siebbeles and D. Dorfs, *Chem. Mater.*, 2017, **29**, 7371–7377.

22 R. Himstedt, D. Hinrichs and D. Dorfs, *Z. Phys. Chem.*, 2018, **233**, 3–14.

23 T. Iwamoto, A. Nagao, K. Kitagishi, S. Honjo and B. Jeyadevan, *J. Phys. Chem. Solids*, 2015, **87**, 136–146.

24 H. Winnischofer, T. C. R. Rocha, W. C. Nunes, L. M. Socolovsky, M. Knobel and D. Zanchet, *ACS Nano*, 2008, **2**, 1313–1319.

25 Y. Tan, D. Sun, H. Yu, B. Yang, Y. Gong, S. Yan, Z. Chen, Q. Cai and Z. Wu, *CrystEngComm*, 2014, **16**, 9657–9668.

26 J. Park, E. Kang, S. U. Son, H. M. Park, M. K. Lee, J. Kim, K. W. Kim, H. J. Noh, J. H. Park, C. J. Bae, J. G. Park and T. Hyeon, *Adv. Mater.*, 2005, **17**, 429–434.

27 K. Mandel, F. Dillon, A. a. Koos, Z. Aslam, K. Jurkschat, F. Cullen, A. Crossley, H. Bishop, K. Moh, C. Cavelius, E. Arzt and N. Grobert, *Chem. Commun.*, 2011, **47**, 4108–4110.

28 H. P. Andaraarachchi, M. J. Thompson, M. A. White, H. J. Fan and J. Vela, *Chem. Mater.*, 2015, **27**, 8021–8031.

29 S. Carenco, Y. Hu, I. Florea, O. Ersen, C. Boissière, N. Mézailles and C. Sanchez, *Chem. Mater.*, 2012, **24**, 4134–4145.

30 J. Contreras-Mora, H. Ariga-Miwa, S. Takakusagi, C. T. Williams and K. Asakura, *J. Phys. Chem. C*, 2018, **122**, 6318–6322.

31 E. Muthuswamy, G. H. L. Savithra and S. L. Brock, *ACS Nano*, 2011, **5**, 2402–2411.

32 D. Li, K. Senevirathne, L. Aquilina and S. L. Brock, *Inorg. Chem.*, 2015, **54**, 7968–7975.

88

Supplementary Information

Halide Ion Influence on the Formation of Nickel Nanoparticles and their Conversion into Hollow Nickel Phosphide and Sulphide Nanocrystals

Rasmus Himstedt,[a] Dominik Hinrichs,[a] Joachim Sann,[bc] Anica Weller,[d] Georg Steinhauser [d] and Dirk Dorfs *[ae]

[a] Institute of Physical Chemistry and Electrochemistry, Leibniz Universität Hannover, Callinstraße 3A, 30167

Hannover, Germany.

[b] Center for Materials Research (LaMa), Justus Liebig University Giessen, Heinrich-Buff-Ring 16, 35392 Gießen,

Germany.

[c] Institute of Physical Chemistry, Justus Liebig University Giessen, Heinrich-Buff-Ring 17, 35392 Gießen, Germany.

[d] Institute of Radioecology and Radiation Protection, Leibniz Universität Hannover, Herrenhäuser Straße 2, 30419

Hannover, Germany.

[e] Cluster of Excellence PhoenixD (Photonics, Optics, and Engineering Innovation Across Disciplines), Hannover,

Germany.
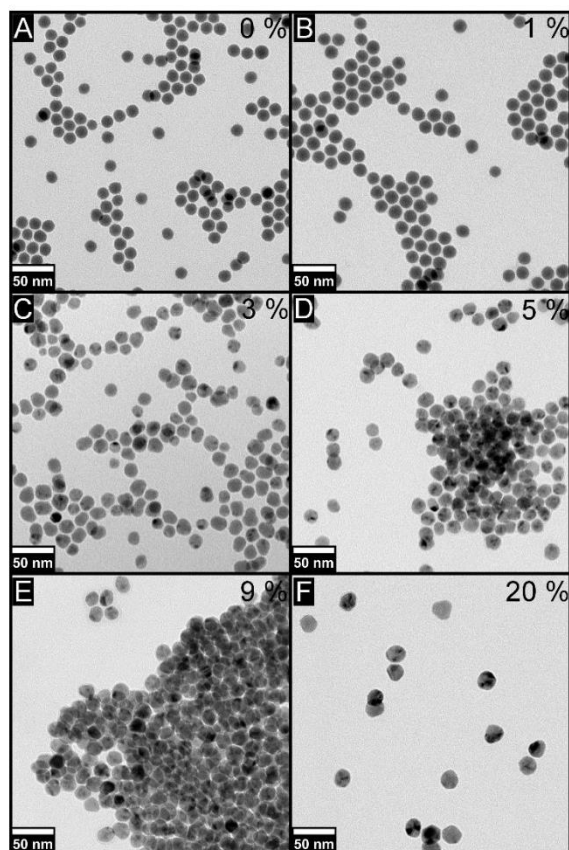
1. TEM Overview Images of Ni Nanoparticles

Fig. S1 TEM overview images of Ni nanoparticles synthesised in the presence of different concentrations of chloride ions. The influence of the chloride ions on the average particle diameter is negligible in the investigated concentration range. Only for high concentrations, a small increase is visible.

2. Investigation of the Phosphorus Content of Nanoparticles Synthesised in the Presence of Different Amounts of Cl⁻

Selected area electron diffraction (SAED) measurements were conducted in case of the amorphous nanoparticles and revealed only fcc-Ni reflections (see Fig. S2A). This means small Ni crystallites are present in the particles. However, the content of the largely amorphous areas cannot be determined by this method. In order to investigate this, inductively coupled plasma mass spectrometry (ICP-MS) and X-ray photoelectron spectroscopy (XPS) measurements were performed in case of samples synthesised in the presence of different amounts of chloride. The XPS results show that phosphorus is present in form of nickel phosphates which most likely are located in the ligand shell of the nanoparticles or inside the organic layer surrounding them and also as nickel phosphide which could also have formed in the bulk of the particles. The ratio of phosphide to phosphate is decreasing with an increasing amount of used chloride (see Fig. 2B-G). The ICP-MS analysis, on the other hand, shows a large amount of phosphorus in the sample containing amorphous particles which is strongly decreased when chloride is used. Additionally, an attempt was made to measure the residual amount of chlorine in the samples but in case of all measured particle concentrations, the chlorine mass concentration was below the

detection limit of the device. Overall, these results, which are summarised in Tab. S1, show that while the amorphous nanoparticles contain a large amount of nickel phosphide (15 %), the presence of chloride during the particle synthesis stops the incorporation of P resulting in crystalline Ni nanoparticles. Also, the removal of chloride via the washing steps seems to be quantitative. Additionally, Fig. S3 shows the behaviour of the respective particle dispersions when confronted with a strong permanent magnet. While the meniscus of the solution containing the amorphous nanoparticles does not visibly change, the ones of the other solutions do react to the magnetic field. This is also indicative of the formation of nickel phosphide in the absence of chloride since the phosphorus incorporation likely severely alters the magnetic properties of the particles.
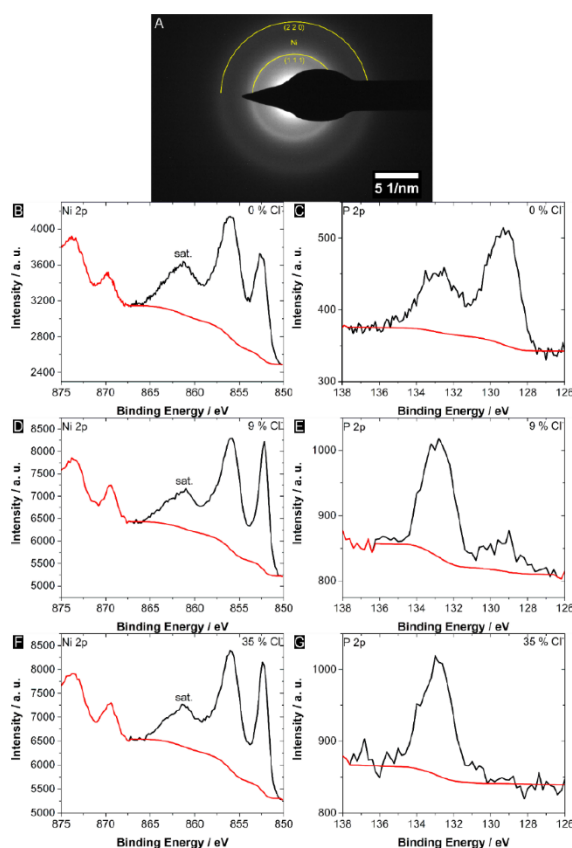

Fig. S2 (A) SAED image of a sample of X-ray-amorphous nanoparticles synthesised without any addition of halide ions to the reaction mixture. Very broad reflections, which correspond to the Ni (1 1 1) and (2 2 0) lattice planes, are visible. This result leads to the conclusion that very small Ni crystallites exist within the particles. (B), (D), (F) Ni 2p XPS spectra (black) of samples synthesised in the presence of 0, 9 and 35 % Cl⁻, respectively. The background is shown as a red line. In addition to a satellite peak at 862 eV, two relevant peaks are visible. According to previous studies on TOP-capped Ni nanoparticles, which present very similar Ni 2p spectra, the peak at 856 eV corresponds to $Ni(OH)_2$ which forms on the particle surface.[1,2] However, the existence of nickel phosphate could also be responsible in this case.[3] The peak at 853 eV, on the other hand, is probably due to elemental Ni. It can be seen that compared to the X-ray amorphous particles the relative intensity of the latter peak is increased in case of the samples where chloride was used. (C), (E), (G) P 2p XPS spectra of the same samples. Again, two peaks are visible in case of the amorphous particles. The one at 133 eV corresponds to P in a high oxidation state like it is the case in phosphates while the peak at 129 eV is caused by nickel phosphides. It is obvious that while the majority of the phosphorus in the amorphous nanoparticles consists of phosphide (58.5 %), the addition of chloride to the nanoparticle synthesis leads to a continuous decrease of the phosphide fraction (22.6 % and 7.1 % for the samples with 9 and 35 % Cl⁻, respectively).

Tab. S1 Total P and Ni contents of samples synthesised in the presence of different amounts of Cl⁻ determined by ICP-MS experiments as well as phosphide percentage of the P fraction measured via XPS. Using these results, the atomic percentage of phosphorus (as phosphide) inside the nickel nanoparticles could be calculated.

Used Cl⁻ amount / %	Ni/P Atom Ratio by ICP-MS	Fraction of Phosphide / %	P in Ni Particles / %
0	3.28	58.5	15.1
9	21.27	22.6	0.7
35	34.50	7.1	0.3
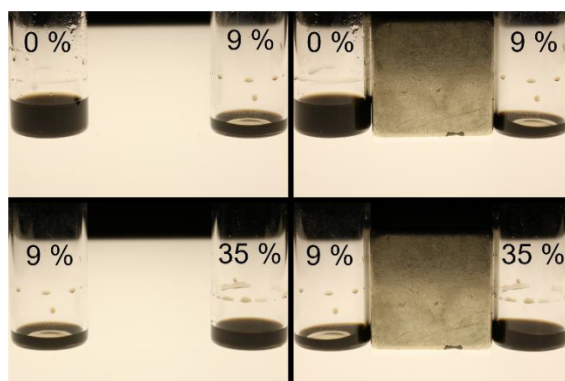
Fig. S3 Photographs of nanoparticle dispersions produced using different amounts of chloride during the synthesis without (left side) and in (right side) the presence of a neodymium magnet. It can be seen that the meniscus of the dispersion containing the amorphous particles does not visibly change while the others strongly react to the magnetic field.

3. TEM and XRD Analysis of Samples Synthesised with Different Cl⁻ Precursors

Different chloride ion precursors were used instead of TDAC. Like TDAC, chlorotriphenylmethane (CTPM) is decomposing under the reaction conditions and chloride ions are released. If it is added to the synthesis mixture the resulting nanoparticles look very similar. The crystallites grow larger the more chloride is present as shown by TEM and XRD analysis (see Fig. S4). In order to directly introduce solved chloride ions into the synthesis from the very beginning, the usual Ni precursor was also partly substituted by $NiCl_2 \cdot 6H_2O$. In this case, the trend is also the same and crystalline particles are obtained (see Fig. S5). Thus, except for little differences in the particle diameters, which could be due to a different solubility and therefore reactivity of the chloride sources in the used solvent, the nature of the precursor does not seem to have an important influence on the behaviour of the Ni nanoparticle system.
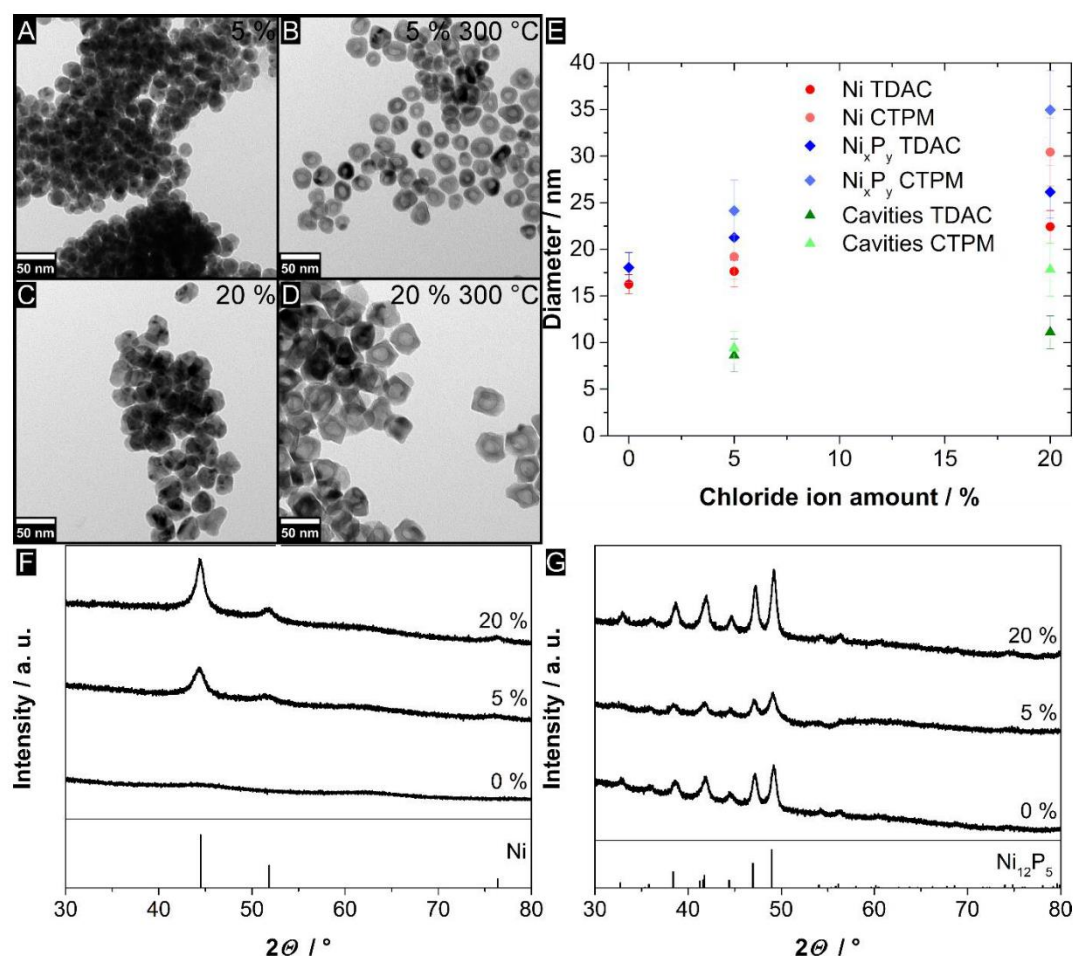
Fig. S4 TEM images of nanoparticles before and after crystallisation using different amounts of chlorotriphenylmethane (CTPM) as chloride ion precursor (A-D). The size of the particles and their shape anisotropy increases in case of the larger chloride ion concentration resulting in slightly different hollow nanoparticles after a subsequent crystallisation step at 300 °C when compared to the particles crystallised in the presence of tetradodecylammonium chloride (TDAC). (E) Dependence of the diameter of the shown nickel and nickel phosphide nanoparticles and their inner cavity on the type of chloride precursor present during their synthesis. The error bars correspond to the standard deviations of the measured diameters. It can be seen that the overall particle size is slightly increased with larger amounts of the halide. If CTPM is present the particles seem to grow larger than when the standard precursor TDAC is used, especially in case of larger amounts. (F) X-ray diffraction patterns of Ni nanoparticles synthesised with different amounts of CTPM as chloride ion precursor present. With an increasing chloride concentration, the Ni reflections (PDF card #: 01-087-0712) become more pronounced. (G) X-ray diffraction patterns of the corresponding nickel phosphide nanocrystals. In case of all the investigated chloride ion concentrations, the obtained nickel phosphide phase is $Ni_{12}P_5$ (PDF card #: 01-074-6017).
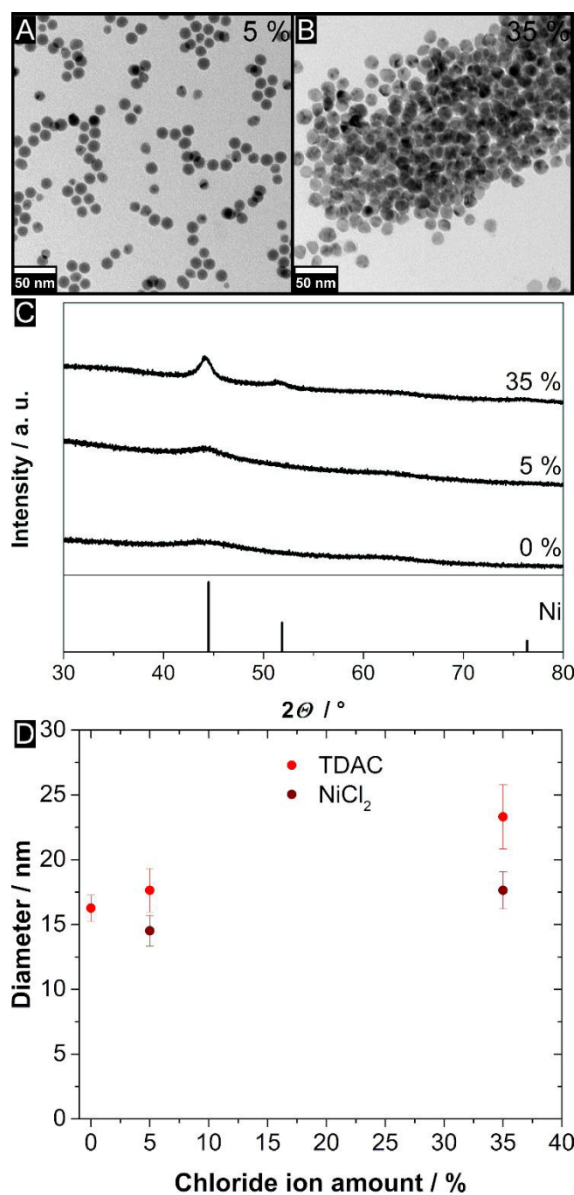
Fig. S5 TEM images of Ni nanoparticles synthesised by replacing different percentages of Ni(acac)$_2$ by NiCl$_2\cdot$6H$_2$O. With 2.5 % nickel chloride (5 % Cl$^-$) partially crystalline spherical Ni nanoparticles are obtained (A), while by using 17.5 % nickel chloride (35 % Cl$^-$) as Ni precursor fully crystalline particles are formed (B). (C) X-ray diffraction patterns of the respective particles. With an increasing chloride concentration, the Ni reflections (PDF card #: 01-087-0712) become more pronounced. They are, however, noticeably broader than the reflections of nanoparticles synthesised using different chloride sources, which could be explained by the smaller overall size of the nanocrystals. (D) Dependence of the diameter of the shown nickel nanoparticles on the type of chloride precursor present during their synthesis. The error bars correspond to the standard deviations of the measured diameters. It can be seen that the overall particle size is slightly increased with larger amounts of the halide. If NiCl$_2\cdot$6H$_2$O is present the particles seem to turn out smaller than when the standard precursor tetradodecylammonium chloride (TDAC) is used, especially in case of larger amounts.
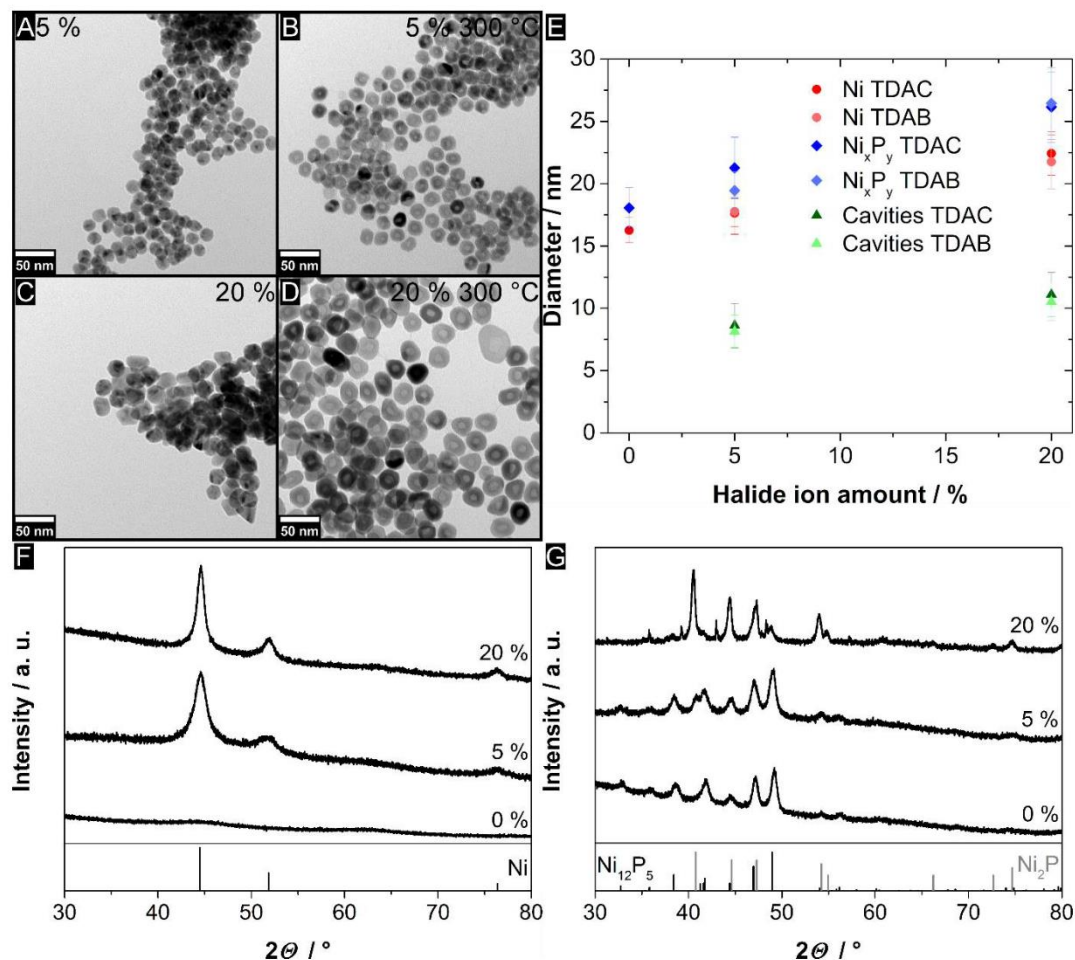
4. TEM and XRD Analysis of Samples Synthesised in the Presence of Br⁻

Fig. S6 TEM brightfield images of nickel nanoparticles synthesised in the presence of 5 % (A) and 20 % (C) bromine relative to nickel and of the resulting nickel phosphide nanocrystals after crystallisation at 300 °C (B and D, respectively). The size of the initial particles increases slightly with the larger bromide concentration. Hollow particles are obtained in both cases. (E) Dependence of the diameter of the shown nickel and nickel phosphide nanoparticles and their inner cavity on the number of bromide ions relative to nickel atoms present during their synthesis. The error bars correspond to the standard deviations of the measured diameters. It can be seen that the overall particle size is slightly increased with larger amounts of the halide. There is no noticeable difference between the resulting particle sizes from syntheses with tetradodecylammonium chloride (TDAC) or tetradodecylammonium bromide (TDAB). Potentially, the nanoparticles formed in the presence of bromide ions tend to be slightly smaller. (F) X-ray diffraction patterns of the nanoparticle samples synthesised in the presence of different amounts of bromide ions. The resulting nickel (PDF card #: 01-087-0712) crystallite size increases with the amount of bromide. (G) X-ray diffraction patterns of the corresponding nanoparticle samples after crystallisation at 300 °C. The obtained nickel phosphide crystal phase is a mixture of $Ni_{12}P_5$ (PDF card #: 01-074-6017) and Ni_2P (PDF card #: 00-003-0953), while in case of larger halide amounts Ni_2P is found almost exclusively.

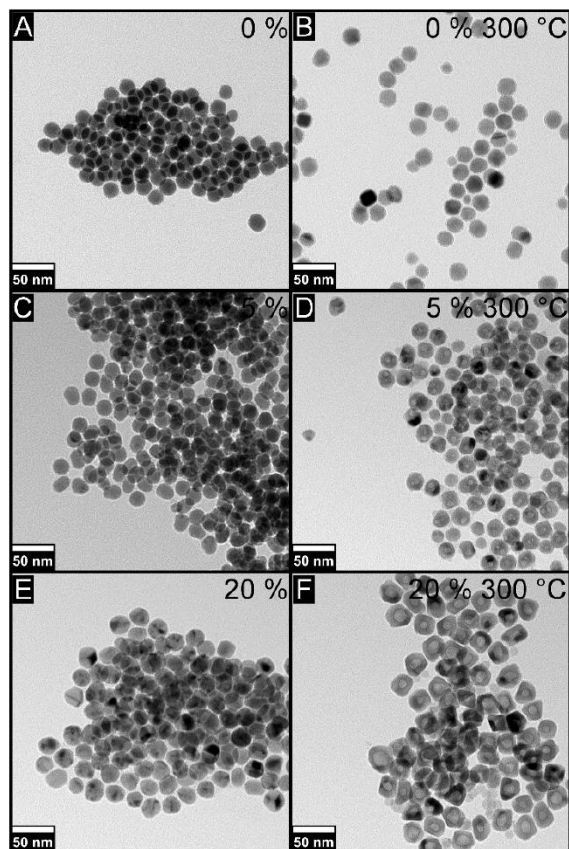**5. TEM and XRD Analysis of Samples Synthesised with Oleylamine of Different Purity**

Fig. S7 TEM micrographs of Ni/Ni$_x$P$_y$ particles synthesised using oleylamine of 70 % purity in the presence of different amounts of chloride ions. The usual trend of more crystalline nickel particles and hollower resulting nickel phosphide nanocrystals with increasing halide concentration can be observed.
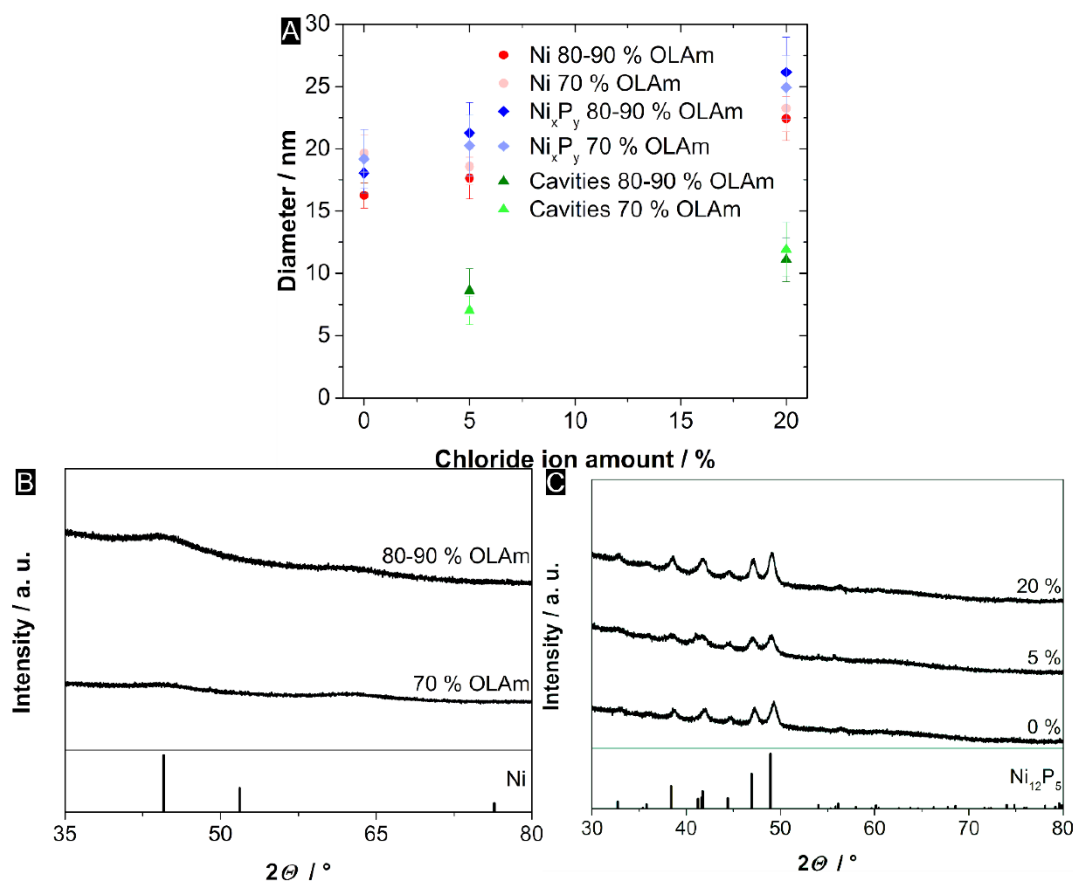
Fig. S8 (A) Dependence of the diameter of nickel nanoparticles, the corresponding nickel phosphide nanocrystals, and their inner cavity on the amount/purity of oleylamine (OLAm) present during their synthesis. The error bars correspond to the standard deviations of the measured diameters. It can be seen that in case of both OLAm purities the overall particle size is slightly increased with larger amounts of the halide. While the particles synthesised without any chloride are expectedly larger in case of the less pure OLAm, no large difference for the other samples can be seen. (B) X-ray diffraction patterns of the nanoparticle samples synthesised in the presence of oleylamine (OLAm) of different purity. The resulting nickel (PDF card #: 01-087-0712) crystallite size seems to be slightly larger in case of the purer OLAm. (C) X-ray diffraction patterns of the respective nanoparticle samples crystallised in the presence of less pure OLAm (70 %) and different amounts of TDAC. The obtained nickel phosphide crystal phase for all halide ion concentrations is $Ni_{12}P_5$ (PDF card #: 01-074-6017).

6. TEM and XRD Analysis of Samples Synthesised in Different Solvents
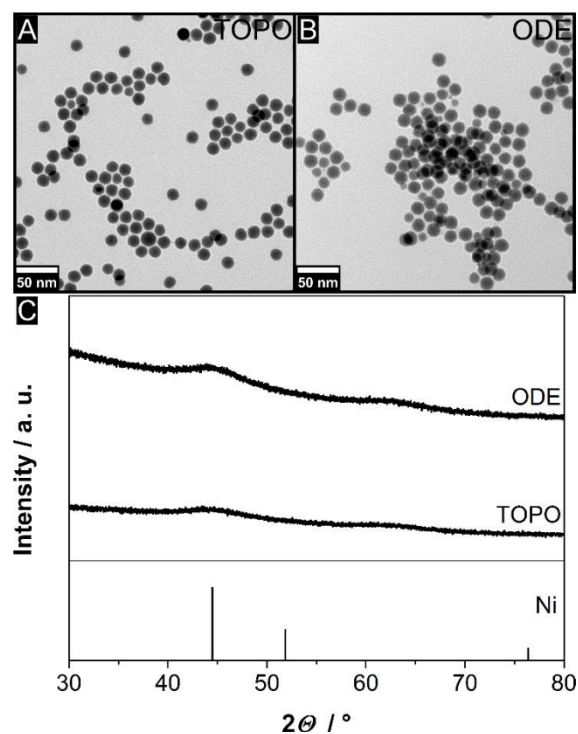

Fig. S9 TEM micrographs of Ni particles synthesised with TOPO (A, average particle diameter of 16.3 ± 1.0 nm) and ODE (B, average particle diameter of 15.2 ± 1.5 nm) used as the solvent for the synthesis. (C) X-ray diffraction patterns of the corresponding samples. Both nanoparticle batches are mostly amorphous but in case of the ODE, the very broad Ni (1 1 1) reflection (PDF card #: 01-087-0712) at around 45 °2ϑ is possibly slightly more pronounced. However, these results strongly suggest that the observed incorporation of phosphorus into the nanoparticles leading to their amorphous nature is mainly due to the presence of TOP and not caused by the usage of TOPO as the solvent for the reaction.

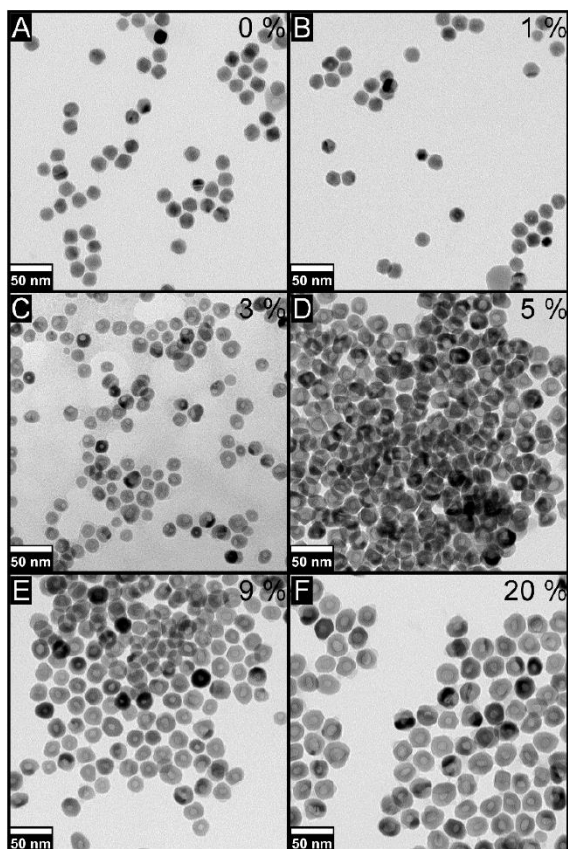**7. TEM Overview Images of Nickel Phosphide Nanoparticles**

Fig. S10 TEM overview images of nickel phosphide nanoparticles crystallised in the presence of different concentrations of chloride ions (TDAC). With an increasing amount of chloride present the size of the particle cavities, formed via the nanoscale Kirkendall effect, is growing and hollow nanocrystals are obtained. Interestingly, in case of low chloride concentrations, the nanoparticles often have multiple cavities owing to small Ni crystallites in the precursor nanoparticles, which were probably located at a certain distance apart from each other.

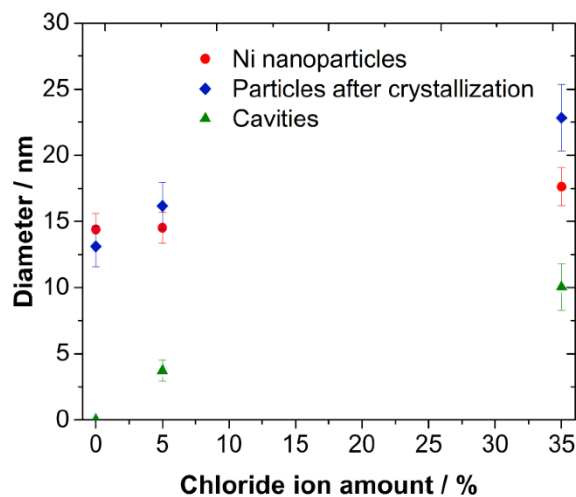**8. Diameters of Particles Crystallised in the Presence of 1-dodecanethiol**

Fig. S11 Dependence of the diameter of nickel nanoparticles, the corresponding nickel phosphide or nickel sulphide nanocrystals, and their inner cavity on the number of chloride ions present during their synthesis after the addition of 1-dodecanethiol (DDT). The error bars correspond to the standard deviations of the measured average diameters. It can be seen that similar to the system without DDT the diameter of the cavities formed via the nanoscale Kirkendall effect is dependent on the chloride concentration. However, it should be noted that in the case of the sample with 5 % chloride multiple cavities often exist within a single particle and it is quite difficult to measure their actual size correctly.

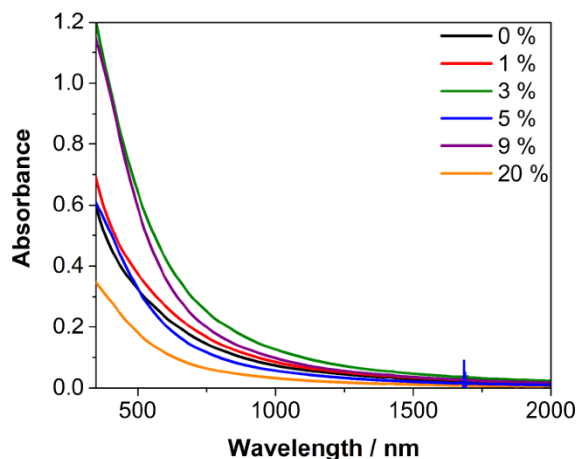**9. Optical Spectroscopy of Nickel and Nickel Phosphide Nanoparticles**

Fig. S12 UV/vis/NIR absorbance spectra of Ni particles in colloidal solution (toluene) synthesised in the presence of different amounts of chloride ions. In all cases, the absorbance rises towards shorter wavelengths due to the localised surface plasmon resonance of Ni which is located in the UV regime of the electromagnetic spectrum and outside of the possible measuring range for toluene.
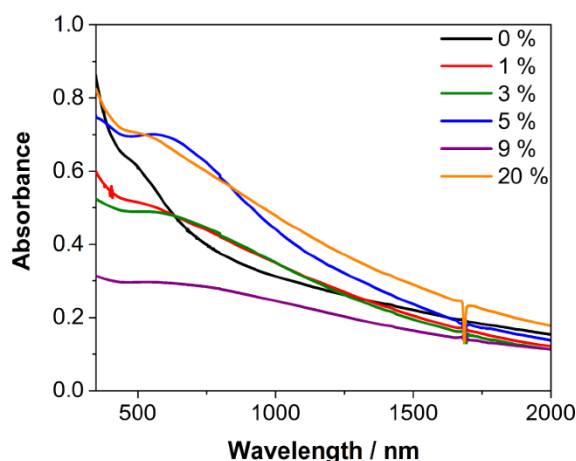

Fig. S13 UV/vis/NIR absorbance spectra of Ni_xP_y particles in colloidal solution (toluene) crystallised in the presence of different amounts of chloride ions. An absorbance shoulder can be seen at around 500 nm in case of the sample synthesised in the absence of halides while especially the nanoparticles produced with higher amounts of chloride in the synthesis show stronger absorbance at longer wavelengths. Due to the size of the particles, this cannot be explained exclusively by light scattering. However, since both $Ni_{12}P_5$ and Ni_2P show metallic behaviour at room temperature a possible explanation is the existence of a localised surface plasmon resonance with a very broad absorbance band like it is the case for small nickel sulphide nanoparticles.[4-8] Further experiments would be needed to confirm this theory.

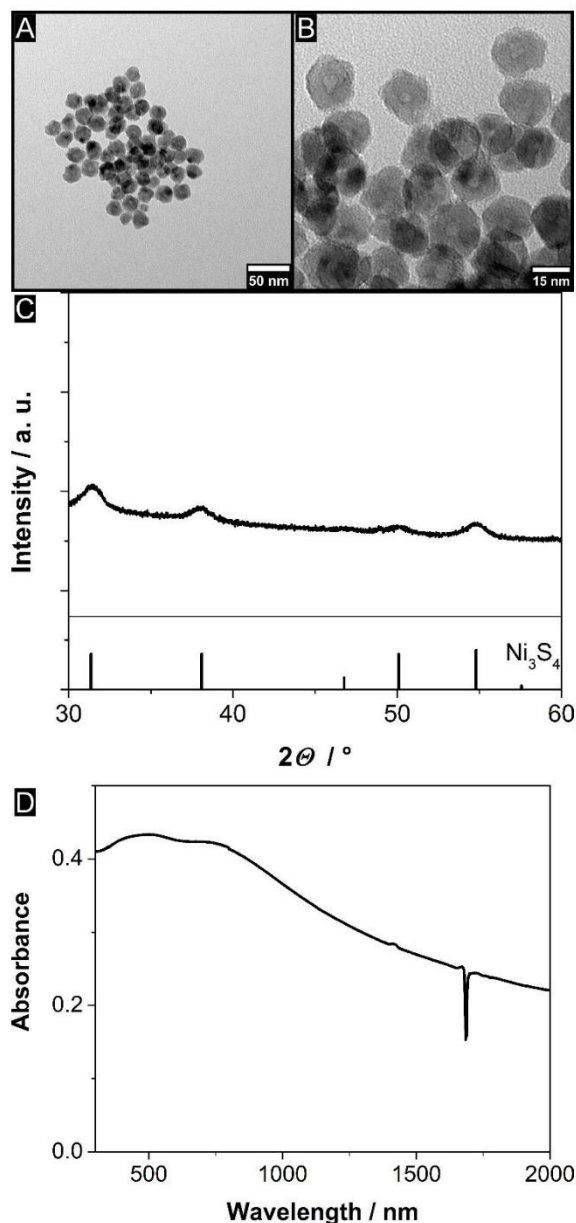**10. Particles Crystallised in the Presence of Elemental S**

Fig. S14 TEM overview image (A) and HR-TEM micrograph (B) of nanoparticles crystallised in the presence of S and 40% chloride. Hollow and polycrystalline nanoparticles with a tendency to agglomerate are obtained. In the XRD pattern of the sample (C) it is visible that the formed phase is Ni_3S_4 (PDF card #: 00-008-0106). The UV/vis/NIR absorbance spectrum (D) of the particles shows a LSPR band at slightly below 500 nm which is typical for Ni_3S_4 and a shoulder at longer wavelengths which could be due to plasmonic coupling in nanoparticle aggregates. Additionally to aggregation, the broader linewidth of these particles compared to the Ni_3S_2 nanocrystals could be explained by the polycrystalline nature of the obtained Ni_3S_4 which leads to stronger damping processes. The only synthetic differences to the Ni_3S_2 procedure are a change of the solvent from TOPO to ODE and the substitution of DDT by 5 mL of a mixture of S dispersed in ODE (0.2 M).
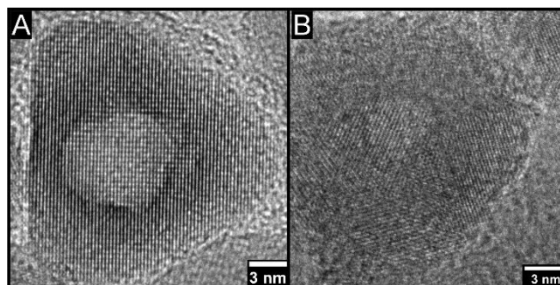
11. HR-TEM Comparison of Hollow Ni₃S₂ and Ni₃S₄ Nanoparticles

Fig. S15 HR-TEM images of representative hollow Ni_3S_2 (A) and Ni_3S_4 (B) nanoparticles crystallised in the presence of 40% chloride. It can be seen that while the Ni_3S_2 particle is single-crystalline the Ni_3S_4 pendant consists of multiple smaller crystallites.

References

1   T. Iwamoto, A. Nagao, K. Kitagishi, S. Honjo and B. Jeyadevan, *J. Phys. Chem. Solids*, 2015, **87**, 136–146.

2   H. Winnischofer, T. C. R. Rocha, W. C. Nunes, L. M. Socolovsky, M. Knobel and D. Zanchet, *ACS Nano*, 2008, **2**, 1313–1319.

3   J.-J. Li, M.-C. Liu, L.-B. Kong, D. Wang, Y.-M. Hu, W. Han and L. Kang, *RSC Adv.*, 2015, **5**, 41721–41728.

4   I. Shirotani, E. Takahashi, N. Mukai, K. Nozawa, M. Kinoshita, T. Yagi, K. Suzuki, T. Enoki and S. Hino, *Jpn. J. Appl. Phys.*, 1993, **32**, 294.

5   S. Ishida, Y. Sugizaki, T. Nakamura, K. Edamoto, M. Matsunami, T. Hajiri and S. Kimura, *e-Journal Surf. Sci. Nanotechnol.*, 2015, **13**, 93–98.

6   J. S. Chen, C. Yu, H. Lu and J. M. Chen, *Phase Transitions*, 2016, **89**, 1078–1089.

7   Q. Yuan, H. Ariga and K. Asakura, *Top. Catal.*, 2015, **58**, 194–200.

8   R. Himstedt, P. Rusch, D. Hinrichs, T. Kodanek, J. Lauth, S. Kinge, L. D. A. Siebbeles and D. Dorfs, *Chem. Mater.*, 2017, **29**, 7371–7377.

4 Nickel Sulfide Nanoparticles with Temperature-Switchable Plasmon Resonances

4.1 Summary

Since metallic nickel sulfide nanoparticles have been established as a viable alternative to noble metal particles, it is also interesting to investigate if there are specific properties of certain nickel sulfide phases that could pose an additional opportunity to create novel plasmonic materials. The α-NiS phase, which is metastable at room temperature (see chapter 1.4), for example, shows a reversible Mott-transition (see chapter 1.5) at about 265 K in the bulk. Because the electronic properties of the material are heavily altered with this change, the LSPR of nanoparticles consisting of α-NiS should also be drastically influenced. Therefore, in this chapter, α-NiS nanoparticles and Au-α-NiS (Au-NiS) core-shell particles were synthesized and their plasmonic properties were examined using temperature-dependent optical spectroscopy. The obtained results were then compared to those of Au nanocrystals which served as reference material.

It could be shown that the optical density of the α-NiS particles' LSPR band is strongly tunable by varying the temperature in a range from 235-295 K in toluene. Below a temperature of about 240 K, the LSPR is completely switched off and can be switched on again by reheating the particle sample. This reversal shows a slight hysteresis (the optical density only starts to increase again at temperatures above 250 K) as can be expected for a first-order phase transition. In the case of the Au-NiS core-shell particles, the change in absorbance is much smaller. This could be due to the remaining charge carrier density of the Au cores in combination with different amounts of uncompensated magnetic moments present inside the particles which were revealed by

magnetic susceptibility measurements. However, also in this system, a reversible switching behavior at similar temperatures was observed. Hence, nanoparticles consisting of α-NiS could be an exciting subject for applications that benefit from a temperature-switchable plasmonic material.

4.2 Temperature-Sensitive Localized Surface Plasmon Resonance of α-NiS Nanoparticles

Rasmus Himstedt, Dirk Baabe, Christoph Wesemann, Patrick Bessel, Dominik Hinrichs, Anja Schlosser, Nadja C. Bigall, and Dirk Dorfs

Article

Temperature-Sensitive Localized Surface Plasmon Resonance of α-NiS Nanoparticles

Published as part of The Journal of Physical Chemistry virtual special issue "Marie-Paule Pileni Festschrift".

Rasmus Himstedt, Dirk Baabe, Christoph Wesemann, Patrick Bessel, Dominik Hinrichs, Anja Schlosser, Nadja C. Bigall, and Dirk Dorfs*

Cite This: *J. Phys. Chem. C* 2021, 125, 26635−26644

Read Online

ACCESS | Metrics & More | Article Recommendations | Supporting Information

ABSTRACT: The presented work shows a synthesis route to obtain nanoparticles of the hexagonal α-NiS phase and core−shell particles where the same material is grown onto previously prepared Au seeds. In the bulk, this nickel sulfide phase is known to exhibit a metal−insulator type phase transition (MIT) at 265 K which drastically alters its electrical conductivity. Since the produced nanoparticles show a localized surface plasmon resonance (LSPR) in the visible range of the electromagnetic spectrum, the development of their optical properties depending on the temperature is investigated. This is the first time an LSPR of colloidal nanoparticles is monitored regarding such a transition. The results of UV−vis absorbance measurements show that the LSPR of the particles can be strongly and reversibly tuned by varying the temperature. It can be switched off by cooling the nanoparticles and switched on again by reheating them above the transition temperature. Additional to the phase transition, the temperature-dependent magnetic susceptibility of α-NiS and Au-NiS nanoparticles suggests the presence of different amounts of uncompensated magnetic moments in these compounds that possibly affect the optical properties and may cause the observed quantitative differences in the LSPR response of these materials.
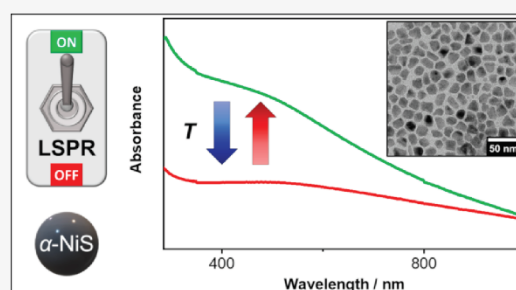
INTRODUCTION

At room temperature, α-NiS ($Ni_{1−x}S$) is a metastable metallic nickel sulfide phase crystallizing in the hexagonal NiAs structure.[1] By cooling the material to temperatures below 260−270 K, a reversible first-order phase transition can be triggered.[1] Along with this transition, the electrical conductivity of the sample is drastically reduced (the specific resistivity changes from about $10^{−5}$ to $10^{−3}$ Ω cm), and the magnetism of the bulk material changes from paramagnetic to antiferromagnetic, whereas the structure of the hexagonal system is only slightly altered.[2] The *a* and *c* lattice parameters are increasing by 0.3 and 1%, respectively, while the volume of the unit cell increases by 1.3%.[1,3] In contrast to most other metal−insulator transition materials (e.g., Ti_2O_3, V_2O_3, and VO_2),[4] the low-temperature phase of α-NiS is not an electrical insulator or semiconductor but a poorly conducting metal instead.[2] Since the high-temperature phase is a well-conducting metal, nanoparticles of this material should show a localized surface plasmon resonance (LSPR). This has already been shown for different metallic nickel sulfide phases such as Ni_3S_2 and Ni_3S_4.[5] It is therefore interesting to investigate the LSPR of α-NiS nanoparticles and its dependence on the temperature. In this work, a synthesis to produce α-NiS as well as Au-α-NiS

(Au-NiS) core−shell nanoparticles is developed and the obtained particles are characterized in colloidal solution using temperature-dependent optical spectroscopy. In the case of α-NiS, only optical reflectivity measurements on the bulk material have been conducted so far.[6] To the best of the authors' knowledge, an optical investigation of an LSPR in the visible regime of the electromagnetic spectrum in combination with a metal−insulator type transition or an analysis of a plasmonic material showing such a transition in colloidal solution has not been reported yet. The only other studies of this type, which were conducted very recently, were working with films of VO_2 particles with diameters larger than 70 nm, showing infrared LSPR signals.[7−9]

26635
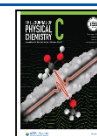
METHODS

Materials. Hydrogen tetrachloroaurate trihydrate ($HAuCl_4 \cdot 3H_2O$, 99.99%) and nickel chloride hexahydrate ($NiCl_2 \cdot 6H_2O$, 99.9%) were obtained from abcr. Borane *tert*-butylamine complex (BBA, 97%), methanol (MeOH, 99.9%), and 1,2,3,4-tetrahydronaphthalene (97%) were obtained from Alfa Aesar. Acetone (99.7%), chloroform (99.8%), eicosane (99.5%), ethanol (EtOH, >98%), hydrochloric acid (HCl, 37%), nitric acid (HNO_3, 69%), 1-octadecene (ODE, 90%), oleylamine (OLAm, 70%), thiobenzoic acid (TBA, 90%), and toluene (99.7%) were obtained from Sigma-Aldrich. Sodium carbonate (Na_2CO_3, 98%) was purchased from VWR Chemicals.

Synthesis of Nickel Thiobenzoate ($NiTB_2$). The synthesis of $NiTB_2$ was done according to a previous study.[10] Briefly, Na_2CO_3 (1.06 g) was dissolved in distilled water (20 mL) before TBA (2.35 mL) was added to the solution, which turned yellow and was stirred for 30 min afterward. Then $NiCl_2 \cdot 6H_2O$ (2.38 g) dissolved in distilled water (20 mL) was added to the reaction mixture, which was subsequently stirred for 60 additional min. The dark red product was precipitated by centrifugation (1 min, 3773g) and washed several times with distilled water and EtOH before it was dried under vacuum and finally stored under inert conditions.

Synthesis of α-NiS Nanoparticles. The synthesis was adapted and modified from a known procedure.[11] $NiTB_2$ (82 mg) was dissolved in OLAm (0.8 mL) by stirring at 40 °C for 2 h. The resulting solution was then injected into OLAm (4 mL), which was previously degassed under vacuum for 2 h at 100 °C, at 200 °C under an Ar flow. After 1 min of reaction time, the mixture was cooled down and toluene (5 mL) was injected. The nanoparticles were precipitated once via the addition of MeOH (5 mL) and subsequent centrifugation (10 min, 3773g). They were then redispersed and stored in toluene (8 mL). The whole process was conducted under inert conditions.

Synthesis of Small Au Nanocrystals (AuNCs). The synthesis of small quasi-spherical gold nanocrystals was carried out via the reduction of tetrachloroaurate in the presence of OLAm.[12] $HAuCl_4 \cdot 3H_2O$ (0.2 g) was dissolved in a mixture of 1,2,3,4-tetrahydronaphthalene (10 mL) and OLAm (10 mL). The solution was cooled to 0 °C. A freshly prepared solution of BBA (87 mg) in 1,2,3,4-tetrahydronaphthalene (1 mL) and OLAm (1 mL) was injected into the reaction mixture. The solution was stirred for two additional hours. Afterward, the AuNCs were precipitated by the addition of acetone (≈ 140 mL), centrifuged (5 min, 5000g), and dispersed in toluene. This cleaning step was repeated. Finally, the product was redispersed and stored in toluene. The average diameter of the AuNCs in the obtained highly monodisperse samples varies from batch to batch and usually lies between 4 and 6 nm. Smaller AuNCs can be produced using increased reaction temperatures (e.g., 40 °C for diameters <3 nm).

Synthesis of Large AuNCs (>6 nm). For the preparation of larger AuNCs, a seed-mediated growth approach was used and modified.[13] For the synthesis of 10 nm gold nanocrystals, a solution of previously prepared AuNCs (≈ 6 nm diameter, 30 mg) was dispersed in a solution of $HAuCl_4 \cdot 3H_2O$ (100 mg) in ODE (10 mL) and OLAm (10 mL). The temperature was increased to 80 °C within 10 min and was held for an additional two hours. The product was precipitated by the addition of acetone, centrifuged (5 min, 5000g), and dispersed in toluene. This solution was used for a consecutive second growing step in $HAuCl_4 \cdot 3H_2O$ (320 mg) in ODE (27 mL) and OLAm (27 mL). After cleaning via precipitation with acetone and centrifugation (5 min, 5000g), the particles were collected in toluene. For the preparation of AuNCs with different diameters, the amount of gold precursor and/or the number of growing steps can be varied.

Synthesis of Au-NiS Core−Shell Particles (Exemplary Amounts for 6.1 nm Cores with a 4.6 nm Shell). The solvent of the AuNC dispersion (600 μL, particle concentration: 6.8×10^{-7} mol/L) was evaporated, the nanoparticles were redispersed in toluene (100 μL) and OLAm (0.5 mL), and the resulting solution was transferred into a syringe. Meanwhile, $NiTB_2$ (15 mg) was dissolved in OLAm (250 μL) by stirring at 40 °C for 2 h. This mixture was filled into a second syringe. Then, the content of the first syringe was injected into OLAm (4 mL), which was previously degassed under vacuum for 2 h at 100 °C, at 150 °C under an Ar flow. Subsequently, the solution inside the second syringe was added to the reaction mixture in a dropwise manner. After 1 min of further reaction time, the solution was cooled down and toluene (5 mL) was added. The product was precipitated via the addition of MeOH (5 mL) and centrifugation (10 min, 3773g) and finally redispersed and kept in toluene (8 mL). All steps during the synthesis were done under inert conditions. The thickness of the shell can be tuned by varying the amount of the seed particles or the $NiTB_2$ depending on the diameter of the chosen core nanocrystals.

Electron Microscopy. Transmission electron microscopy (TEM) measurements were conducted using a FEI Tecnai G2 F20 employing a field emission gun operated at 200 kV. The nanoparticles were cleaned by precipitation with methanol and redispersion in chloroform. The resulting solution was then drop-casted onto carbon-coated copper grids (300 mesh) by Quantifoil.

Elemental Analysis. The gold and nickel mass concentrations of the particle dispersions were determined via atomic absorption spectroscopy (AAS) using a Varian AA 140 spectrometer. Aliquots of the stable dispersions were taken, the solvent was evaporated, and the resulting residue was dissolved in aqua regia. The resulting solution was diluted with deionized water, and the atomic absorption was measured and related to the values of separately prepared calibration solutions with known Au or Ni mass concentrations. In the case of the Au-NiS nanoparticles, only the Ni mass concentration was used since the presence of Ni disturbs the measurement of Au with this device.

Optical Spectroscopy. For the acquisition of optical absorbance spectra, a Cary 5000 UV−vis/NIR spectrophotometer by Agilent Technologies was used in transmission mode. The sample dispersions were diluted with additional toluene and measured in high-performance quartz glass cuvettes with a path length of 1 cm by Hellma Analytics. In the case of the low-temperature measurements, a cryostat OptistatCF by Oxford Instruments was mounted into the device to enable the necessary temperature control via cooling with liquid nitrogen. After reaching each measurement temperature, a waiting time of 10 min was implemented in order to obtain a stable temperature in the cuvette. The dispersions were kept under an inert atmosphere during the whole process.

SQUID Magnetometry. Solid-state magnetic susceptibility measurements on polycrystalline powders of α-NiS and Au-NiS nanoparticles were performed on a Cryogenic Ltd. closed-
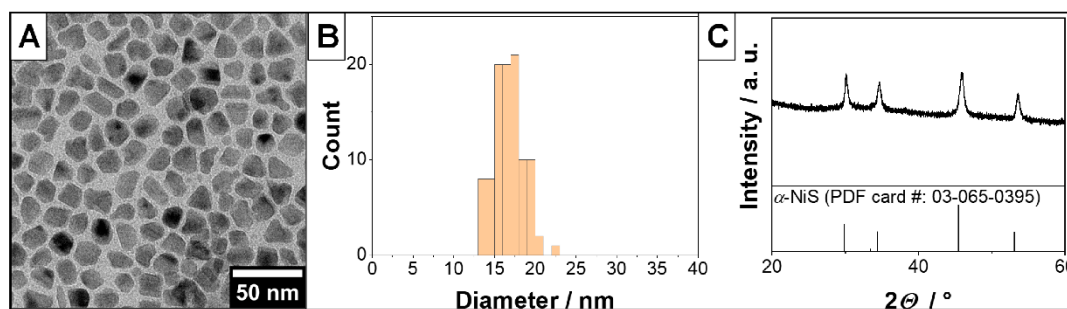
Figure 1. TEM overview image (A) of an exemplary sample of α-NiS nanoparticles and the corresponding size distribution (B). The average diameter of the particles is 16.8 nm $\pm$1.8 nm. (C) X-ray diffraction pattern of the same sample. The obtained crystal phase is hexagonal NiS (α-NiS, PDF card no. 03-065-0395) with no observable impurities.

cycle SQUID magnetometer at temperatures between $T = 4$ and 300 K with external magnetic fields of $H_{ext} = 1$ and 5 kOe. The measurements were executed with a field warming sequence starting at $T = 4$ K after zero-field or field cooling to the base temperature. Additional isothermal magnetization measurements on both compounds with external magnetic fields up to $H_{ext} = 70$ kOe were also executed at selected temperatures. The samples were prepared in gelatin capsules (size 4) by Plano. Before and after the addition of the sample a droplet of Eicosan ($\sim$10 mg each) was filled into the capsules to prevent movement or orientation of the material in the magnetic field. The particle synthesis had to be scaled up drastically ($\times$7 and $\times$10 for the α-NiS and Au-NiS synthesis, respectively) in order to produce enough material for the measurements. To remove the organic ligands, the obtained nanoparticle dispersions were washed once by precipitating them with methanol and afterward redispersed in chloroform. The resulting solution was then added dropwise into the capsule, while the chloroform evaporated over time and was therefore removed from the sample. In this way, amounts of 21.9 and 18.6 mg of the α-NiS and Au-NiS sample could be deposited in the capsules, respectively. The Au-NiS sample contained approximately 17.3 mg of α-NiS and 1.3 mg of Au according to a combined AAS and TEM analysis. The diamagnetic background signal of a gelatin capsule including a droplet Eicosan (19.0 mg) and mounted in a straw was experimentally determined ($\chi_0 = -3.10 \times 10^{-8}$ emu G^{-1}) and subtracted from the raw magnetization data. The experimental data were further corrected for the overall diamagnetism of the investigated molecules using an approximation for this contribution, i.e., $\chi_D = -0.5M \times 10^{-6}$ cm^3 mol^{-1}, with M describing the (unitless) molar mass of the given molecule.[14]

X-ray Diffraction (XRD). XRD measurements were performed with a Bruker D8 Advance device in reflection mode. It was operated at 40 kV and 40 mA using Cu K-alpha radiation. The sample preparation was done analogously to the preparation for the TEM measurements. The nanoparticle dispersions in chloroform were drop-casted onto single crystalline silicon sample holders.

■ **RESULTS AND DISCUSSION**

Nickel sulfide nanoparticles were synthesized from a single-source precursor (NiTB$_2$) in an organic medium (oleylamine), which also provided the surface ligands for the particles. Figure 1A shows an exemplary TEM overview image of the obtained nanocrystals. They have a quasi-spherical shape, which tends to

be somewhat elongated in one axis due to the hexagonal crystal structure of the nickel sulfide. The average diameter of the particles is 16.8 nm $\pm$1.8 nm, and the corresponding narrow size distribution is displayed in Figure 1B. To confirm that the correct nickel sulfide phase has been synthesized, XRD measurements were conducted. The results are shown in Figure 1C, and it is obvious that nanocrystals of the hexagonal α-NiS phase have been obtained.

Previous studies have shown that other nickel sulfide materials tend to easily grow onto gold seed particles to form core–shell nanostructures.[5,15] Since gold nanoparticles shall be used as plasmonic reference material in this work and these kinds of plasmonic core–shell structures tend to have optical properties, which are dominated by the shell material,[5,16] this was also tested in the case of α-NiS in order to diversify the used materials. Gold nanocrystals (AuNCs) of varying sizes were therefore synthesized. TEM overview images and absorbance spectra of these can be found in Figure S1 of the Supporting Information. Using the AuNCs as seed material, a method to grow Au-NiS core–shell structures was developed and resulted in the nanoparticles shown in Figure 2. It can be seen that core–shell nanoparticles with narrow size-distributions can be obtained for various different seed diameters. The thickness of the α-NiS shell can be readily controlled by changing the amount of NiTB$_2$ used in the synthesis. The XRD pattern in Figure 2E shows that both Au and α-NiS are present in the respective sample of large core–shell particles. In the case of the smaller nanoparticles, only Au could be found in the XRD analysis due to its larger scattering cross-section if any reflections could be detected at all. This is due to the small size of the nanocrystals and in line with the results of previous studies on nanoparticles of different nickel sulfide phases.[5,17] The results of these XRD measurements and a general optical analysis of these samples can be found in Figures S2 and S3 of the Supporting Information, respectively.

In order to investigate the temperature-dependent optical properties of the successfully synthesized α-NiS nanostructures, UV–vis absorbance measurements of diluted samples in toluene were conducted using a cryostat to cool the dispersions down to 235 K, which is well below the transition temperature of bulk α-NiS (265 K).[2] Spectra at different temperatures during the cooling and subsequent reheating of the samples are shown in Figure 3. AuNCs were used as a plasmonic reference material (Figure 3A,B). It can be observed that with decreasing temperature, the absorbance of their LSPR maximum at 523 nm is rising, which is the expected outcome.[18] Due to the
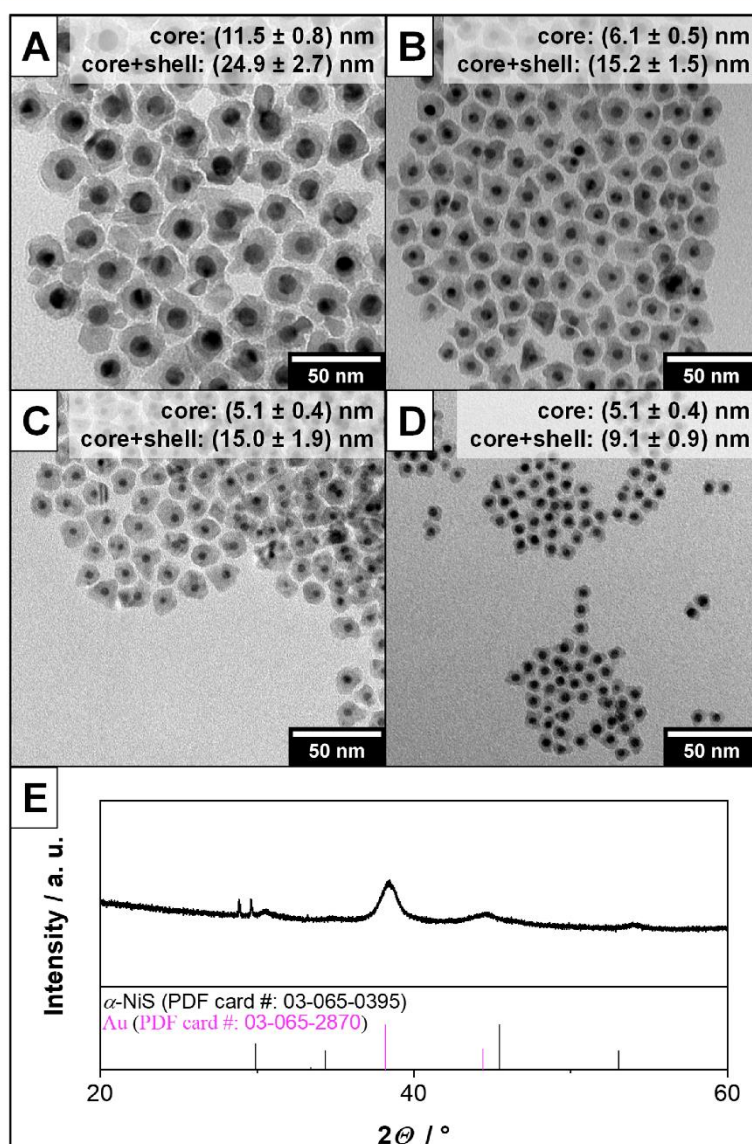
Figure 2. TEM overview image of different Au-NiS core−shell nanoparticle samples (A−D). It can be seen that the synthesis works using different core sizes and also that it is possible to tune the thickness of the α-NiS shell around the same Au cores (C and D). (E) XRD pattern of the sample depicted in part A. Reflections of the large gold cores can be observed as well as reflections that are attributed to the nickel sulfide shell.

smaller influence of lattice phonons at low temperatures (less electron−phonon scattering), the damping of the plasmon is weaker, which in turn leads to a more pronounced band in the absorbance spectrum.[18] This process is reversible, and the original LSPR intensity is retained upon reheating the sample to room temperature. In the case of Au-NiS core−shell nanoparticles where the same AuNCs were used as seed particles for the growth of a 4.5 nm α-NiS shell (Figure 3C,D), the LSPR maximum is broader and hypsochromically shifted compared to the pure AuNCs. This can be explained by the fact that the plasmonic properties of the particles are dominated by the shell material, whose LSPR maximum is

located further toward the UV regime as it is also the case for a few other metallic nickel sulfide phases (cf., the spectra of pure α-NiS in Figure 3E,F).[5,15] Upon cooling the Au-NiS sample, a similar behavior (i.e., a slight increase of the LSPR absorbance with decreasing temperature) is observed until a temperature below 250 K is reached. Then a sudden drop of absorbance at short wavelengths and an increase at long wavelengths are visible. This trend is also reversible upon reheating the dispersion, but the reversal of the change below 250 K happens here at higher temperatures. The 240 K spectrum is identical to the one taken at 250 K during reheating (this hysteresis will be investigated in Figure 4 in more detail). For pure α-NiS
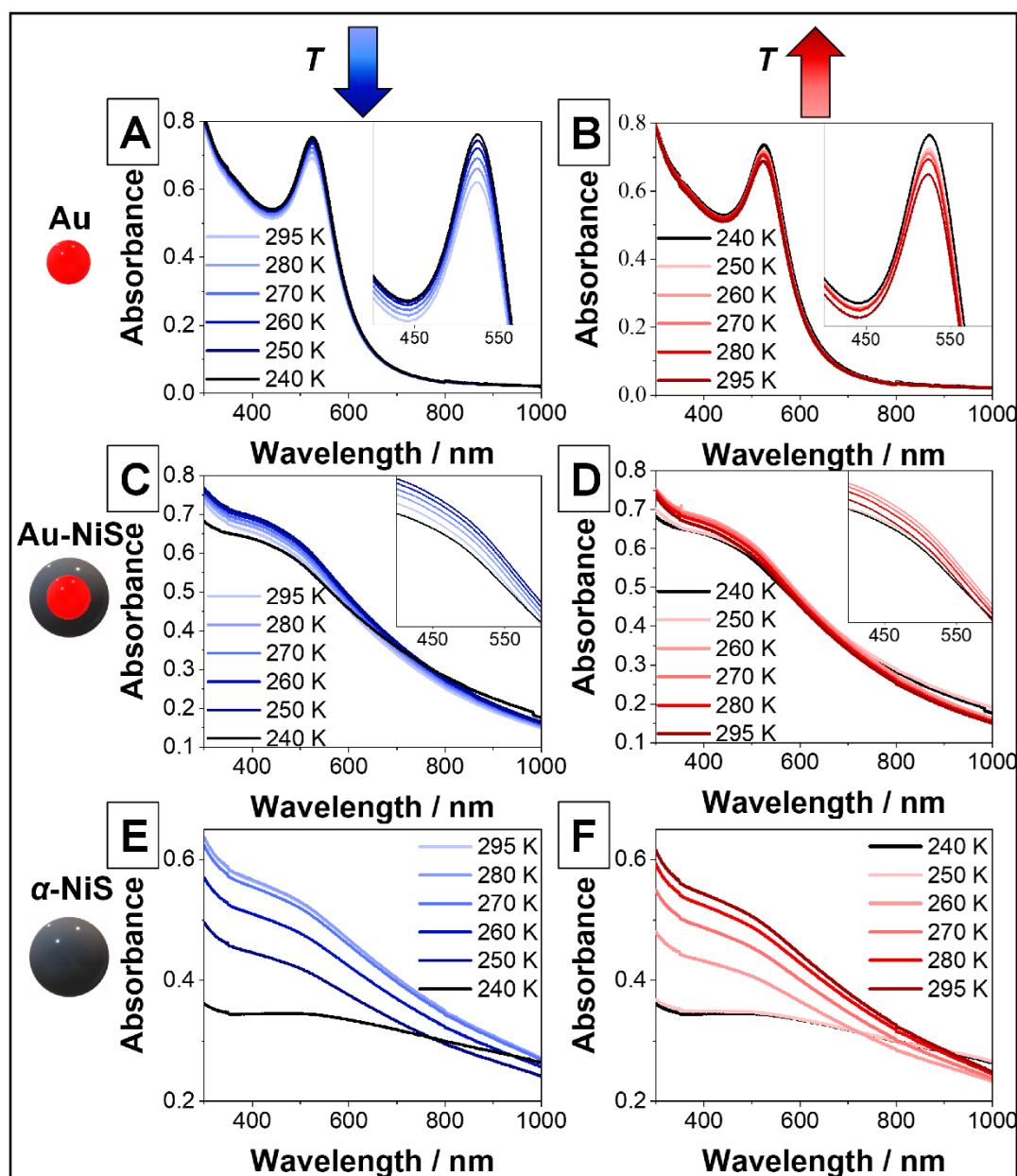
Figure 3. UV–vis absorbance spectra of (A,B) Au nanocrystals, diameter 6.1 nm ±0.6 nm; (C,D) Au-NiS core–shell particles, diameter 15.2 nm ±1.5 nm; and (E,F) α-NiS nanoparticles, diameter 16.8 nm ±1.8 nm at different temperatures. The panels on the left show the evolution of the spectra while the samples are cooled down, while on the right, the absorbance during the reheating of the nanoparticle solutions is observed.

particles of a similar diameter compared to the core–shell structures (16.8 nm ±1.8 and 15.2 nm ±1.5 nm, respectively), a different temperature dependence of the spectra is observed (Figure 3E,F). At room temperature, the LSPR, which is very similar to that of the Au-NiS particles, shows a broad absorbance shoulder reaching into the UV regime. It drops in intensity when the sample is cooled. Here, the change is a lot larger than the usual temperature dependence of an LSPR,

which can be seen by comparing the spectra to the respective ones of Au and Au-NiS nanocrystals. This trend continues until temperatures below 250 K are reached and no further change is observable. Yet, at these temperatures, the behavior of the LSPR is similar to the one of the core–shell particles since the pure nanoparticles also show a hysteresis where the 250 K spectrum during the reheating is identical to the 240 K spectrum. Also, in this case, if the temperature is raised even
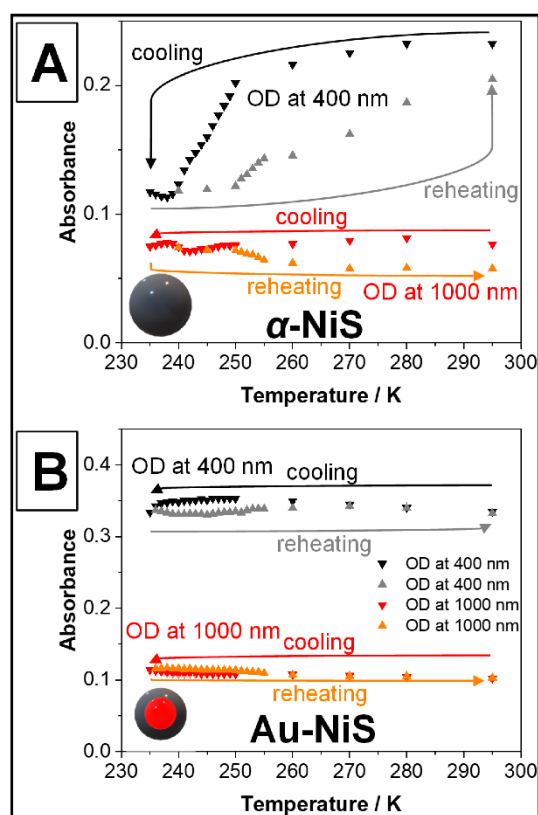
Figure 4. Optical density (OD) of dispersions of pure α-NiS nanoparticles (A) and Au-NiS core−shell particles (B) at 400 and 1000 nm during the cooling and reheating of the respective samples. It can be seen that during cooling, the OD at 400 nm decreases drastically in the case of the pure particles. The process seems to be reversible and also shows a hysteresis. For the Au-NiS particles, this hysteresis also exists but the OD does not drop (it increases instead) until a temperature below 245 K is reached. In both cases, the OD at 1000 nm increases at lower temperatures while also displaying a hysteresis. 235 K was the lowest achievable temperature with the used setup limited by the used solvent toluene.

further, the LSPR band is almost completely regained. It is possible that waiting for a longer time and measuring again would lead to a full recovery of the spectrum. Alternatively, it is also possible that a small part of the sample precipitated during the cooling and subsequent reheating processes, which each took several hours, and was therefore permanently removed from the optical path in the spectrometer resulting in the reduced absorbance at 295 K. Either way, the optical density of the pure α-NiS sample is apparently strongly and reversibly tunable in this manner.

To shine further light on the development of the spectra at lower temperatures, Figure 4 shows the absorbance of α-NiS and Au-NiS particles (equivalent to the respective samples displayed in Figure 3) at 400 and 1000 nm measured for a larger number of temperatures. It is obvious that the optical density (OD) of α-NiS at a wavelength of 400 nm drops significantly faster at temperatures below 250 K than above until a minimum is reached at about 240 K. The OD at 1000 nm also decreases at first, but once 242 K are reached it starts to increase again slightly. This leads to the conclusion that the phase transition of α-NiS starts at 250 K and is completed at around 240 K. Since the metallic character of the material is drastically reduced with the transition, the LSPR vanishes. If the low-temperature phase of α-NiS, which can be characterized as a very poorly conducting metal,[2] still displays an LSPR, it could theoretically be expected to appear deep in the IR part of the electromagnetic spectrum between wavelengths of 2000 and 10000 nm due to its low free charge carrier density of $10^{20}-10^{21}/cm^3$.[19] However, the investigation of these wavelengths was unfortunately not possible with the setup used in this work.

The determined temperature range for the transition could be due to the size distribution of the particles or different amounts of defects present in the particles (presumably due to a small Ni deficit). Generally, the reason why the transition temperature is slightly lower than in the bulk material (265 K) is the larger amount of defects present in the nanocrystals, which by their nature have a large surface-to-volume ratio where surface atoms can be treated as defects too. According to the literature, a transition temperature between 240 and 250 K would still correspond to a composition of $Ni_{0.99}S$ or an even smaller Ni deficit.[20] At both investigated wavelengths, the change of the absorbance starts to turn back once a temperature of 250 K is reached during the reheating of the sample, which likely means the phase transition is being reversed as well. The decrease in absorbance accompanying a decreasing temperature above 250 K should therefore be caused by something else (see the discussion of the magnetic susceptibility measurements).

In the case of the Au-NiS core−shell particles, the absorbance at 400 nm rises with decreasing temperature until a temperature of 245 K is reached and it starts to drop. Along with this change, the absorbance at 1000 nm starts to increase. Both processes are only reversed once a temperature of 250 K is reached during the reheating of the sample. Above 260 K, the optical densities at both wavelengths are completely identical to the ones measured during the cooling of the particle dispersion. The change is therefore 100% reversible.

Thus, it can be assumed that both particle types show a phase transition at 240−250 K displaying a slight hysteresis between the values determined by the cooling and reheating steps of the experiment. The difference in the total decrease of the LSPR signal compared to the pure α-NiS particles could partly be explained by the remaining charge carrier density provided by the gold cores of the Au-NiS core−shell nanoparticles.

It has been shown for bulk α-NiS that the metal−insulator transition at $T_c \approx 265$ K is attended by a sharp magnetic phase transition from an (itinerant-electron) antiferromagnet below and a Pauli-paramagnetic metal above T_c, indicated by the observation of a small and only slightly temperature-dependent magnetic susceptibility in both regimes.[20,21] Therefore, to further characterize the physical and optical properties of the different α-NiS systems, complementary magnetic suscepti-bility measurements were conducted at temperatures between $T = 4$ and 300 K with an external magnetic field of $H_{ext} = 1$ kOe. The syntheses of the samples used for these magnetic measurements were identical as for the samples used for the optical spectroscopy (*vide supra*); however, the syntheses had to be scaled up 7−10 times (for a full characterization of the thusly obtained particles, see Figure S4 in the Supporting

Information). In contrast to the bulk α-NiS material, the magnetic susceptibility of the α-NiS and Au-NiS nanoparticles studied here revealed a Curie-like temperature dependence (see Figure 5), suggesting that the magnetic susceptibility is
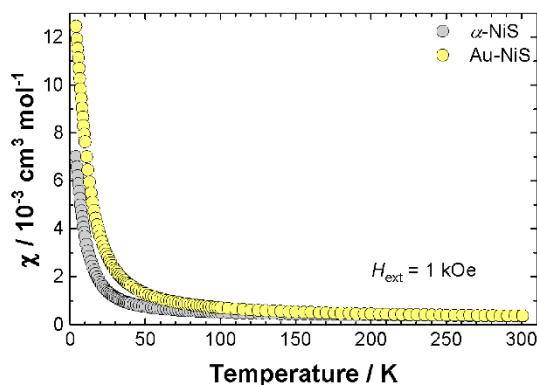

Figure 5. Molar magnetic susceptibility versus temperature of α-NiS (gray symbols) and Au-NiS (yellow symbols) nanoparticles recorded between $T = 4$ and 300 K with an external magnetic field of $H_{ext} = 1$ kOe. The measurements were conducted with a field warming sequence after zero-field cooling.

now predominantly related to a paramagnetic contribution. This qualitative result, and in particular the collapse of the antiferromagnetically long-range ordered state, is in accord with similar measurements on other nanoscale α-NiS systems where no antiferromagnetically long-range ordered state was achieved, and predominant paramagnetic contributions to the magnetic susceptibility were observed.[22−24]

However, it should be noted here that the measurement of the magnetic susceptibility is an integral measurement of the magnetization of a macroscopic sample, and hence, it cannot be safely ruled out that for parts of the sample an antiferromagnetically ordered state is also formed but superimposed by a larger and strongly temperature-dependent paramagnetic contribution. Therefore, to further confirm the presence of predominating paramagnetic contributions on the magnetic susceptibility, supplementary isothermal magnetization measurements on α-NiS were conducted at temperatures of $T = 50$, 235, and 300 K (cf. Figure S5 in the Supporting Information), consistently exhibiting a decreasing magnetic susceptibility ($\chi = \partial M/\partial H$) with increasing temperature. Contrarily, for an antiferromagnetically long-range ordered state (with external magnetic fields below the spin-flip transition), an increasing $\partial M/\partial H$ progression with rising temperature would be expected, while the Pauli spin-susceptibility is temperature independent in first order.

For a qualitative discussion of the magnetic properties of the α-NiS and Au-NiS nanoparticles, the temperature-dependent effective magnetic moment (μ_{eff}) per Ni atom was determined (using a simple Curie approximation with $\mu_{eff} \sim \sqrt{\chi T}$) and plotted in Figure 6. The displayed measurements were conducted starting at $T = 4$ K with a field-warming sequence after field or zero-field cooling to the base temperature, respectively.

Both compounds show similar behavior. Compared with the spin-only value of $\mu_{eff} = 2.83\mu_B$ (which is expected for a single ion $S = 1$, Ni(2+), 3d^8 paramagnetic high-spin center), the

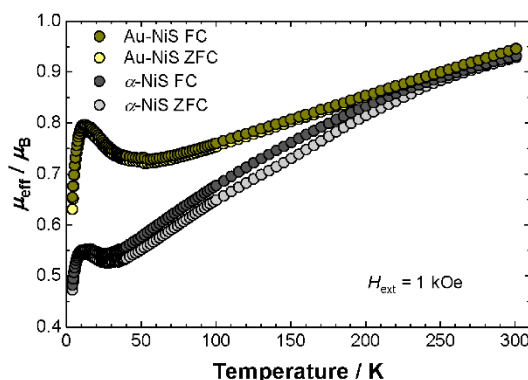**Figure 6.** Effective magnetic moment (per Ni atom) versus temperature of α-NiS and Au-NiS nanoparticles recorded between $T = 4$ and 300 K with an external magnetic field of $H_{ext} = 1$ kOe. The measurements were conducted with a field warming sequence after field cooling (FC, dark gray and dark yellow symbols) or zero-field cooling (ZFC, gray and yellow symbols), respectively.

effective magnetic moment at $T = 300$ K of $\mu_{eff} \approx 0.94\mu_B$ per Ni atom is considerably reduced, indicating that strong antiferromagnetic (AF) correlations are still acting between an unknown number of (paramagnetic) Ni centers. These AF correlations are attributed to the strong AF ($<90°$) super-exchange interaction along the c-axis of hexagonal α-NiS, which was also discussed to explain the magnetic structure of the antiferromagnetically long-range ordered state in the bulk α-NiS material.[2,21] Consistently, a declining effective magnetic moment with decreasing temperature is observed for both investigated compounds; however, the progression with temperature is more pronounced for α-NiS, leading to a low-temperature ($T \rightarrow 0$) value for Au-NiS of $\sim 0.7\mu_B$ and for α-NiS of $\sim 0.5\mu_B$. Regarding the larger surface-to-volume ratio for the Au-NiS nanoparticles, it can be speculated that uncompensated magnetic (Ni) moments located in the (surface) shell of the nanoparticles are the source of this (temperature-independent) paramagnetic moment, while the magnetic moments that are located deeper in the shell (or in the core volume of pure α-NiS) exhibit stronger AF correlations and do not contribute to the magnetic susceptibility at low temperatures ($T \rightarrow 0$).

Another difference between both investigated α-NiS systems is visible in the field cooled (FC) and zero-field cooled (ZFC) measurements. While for Au-NiS particles (that carry a gold core), both curves are superimposed, the FC and ZFC curves markedly differ for pure α-NiS below $T \approx 250$ K, suggesting the presence of uncompensated magnetic moments that are located in the core volume of the α-NiS nanoparticles. To find further experimental evidence, the magnetic susceptibility measurements on α-NiS and Au-NiS particles were repeated with a larger external magnetic field of $H_{ext} = 5$ kOe. The results are shown in Figure S6 in the Supporting Information and revealed only a weak magnetic field dependence for the FC and ZFC curves (i.e., $\mu_{eff}^{FC} - \mu_{eff}^{ZFC} \approx$ constant for $H_{ext} = 1$ and 5 kOe), indicating that a magnetic field-induced spin canting effect can be ruled out as the major source for the different FC and ZFC behavior of α-NiS and Au-NiS. However, a spin canting due to magnetic anisotropy[25] and, alternatively, interparticle interactions[23] may also contribute to thermal

hysteresis effects, but unfortunately a reliable conclusion appears not yet possible based on the available data.

Finally, at low temperatures ($T \approx 10$ K), a distinct maximum of the temperature-dependent effective magnetic moment is observed for both investigated materials, indicating that ferromagnetic (FM) correlations become relevant at these temperatures. Again, regarding the magnetic structure of hexagonal bulk α-NiS, the increasing low-temperature magnetic susceptibility can be attributed to the weak ferromagnetic (nearly 90°) superexchange interaction along the ab-plane of α-NiS (leading to the ferromagnetic alignment of Ni atoms within the ab-plane of bulk α-NiS).[2] Alternatively, a similar "low-temperature anomaly" was also reported for the magnetic susceptibility of other nanoscale α-NiS systems, and spin-frustration (or a spin-glass phase) associated with uncompensated magnetic moments located in the surface shell of the nanoparticles[23] and/or superparamagnetic blocking behavior together with a considerable magnetic field hysteresis[23,24] were discussed. The isothermal magnetization measurements of α-NiS and Au-NiS nanoparticles recorded at $T = 4$ K are shown in Figure S7 in the Supporting Information, revealing that for α-NiS a clearly resolved hysteresis is not achieved. However, indications of a small FM contribution can be anticipated and in particular also for the isothermal magnetization at an elevated temperature of $T = 300$ K (cf. Figure S5 in the Supporting Information). Together with a considerable magnetic field dependence of the effective magnetic moment of α-NiS (cf. Figure S6 in the Supporting Information), this anticipated FM contribution is probably associated with a small ferromagnetic impurity (presumably Ni metal) and not with the α-NiS nanoparticles. For the Au-NiS sample, the isothermal magnetization at $T = 300$ K exhibits the expected (paramagnetic) linear $M(H)$ progression (cf. Figure S5 in the Supporting Information), while at $T = 4$ K a small magnetic field hysteresis (with a low coercitivity field of ~185 Oe) is found, which is in accord with similar measurements on other nanoscale α-NiS systems.[22−24]

In conclusion, the magnetic susceptibility of the investigated compounds revealed some similarities, i.e., (1) a Curie-like magnetic susceptibility (suggesting the presence of uncompensated magnetic moments in these materials), (2) the presence of AF correlations that are observed over the full temperature range, and (3) a low-temperature anomaly (at $T \approx 10$ K) that is attributed to weak FM correlations or spin-frustration. Some differences are also obvious, i.e., (1) a marked discrepancy of the field and zero-field cooled temperature-dependent magnetic susceptibility, which is relevant only for the α-NiS compound (suggesting that uncompensated magnetic moments in the core volume of the nanoparticles are involved), (2) a larger value of the magnetic susceptibility in the low-temperature limit ($T \to 0$) for Au-NiS, indicating a larger number of uncompensated magnetic moments located in the surface shell of Au-NiS than for α-NiS nanoparticles, and (3) a small magnetic field hysteresis that was observed for Au-NiS at $T = 4$ K, while a clearly resolved hysteresis was not achieved at the same temperature for α-NiS. Since the spectroscopic measurements revealed a significant change of the optical properties at characteristic temperatures between $T = 240$ and 250 K associated with a metal−insulator-like transition, the investigation of the magnetic properties was insofar surprising that the magnetic susceptibility revealed a paramagnetic regime in first order without a distinct anomaly in the relevant temperature range. However, assuming that the presence of uncompensated magnetic moments, and in the case of α-NiS presumably those that are located in the core volume of the individual nanoparticles, also impairs the mobility of the free charge carriers and therefore the intensity of the LSPR, it could possibly explain the decline of the optical absorbance spectra of the α-NiS particles above their (optical) transition temperature.

■ CONCLUSIONS

Synthesis procedures to obtain monodisperse α-NiS and Au-NiS core−shell nanoparticles, which show an LSPR in the visible regime of the electromagnetic spectrum, were developed. When the particles are cooled down to 240−250 K, a reversible change to the optical spectra, likely associated with the phase transition of α-NiS, is triggered. In the case of the pure nickel sulfide, there is an additional effect which, according to the measurements of the magnetic susceptibility, could be due to the presence of uncompensated magnetic moments that are presumably located in the core volume of the individual nanoparticles. Here, the observed change in optical density is quite drastic making this an interesting switchable material for various plasmonic applications (e.g., fluorescence enhancement applications or sensory applications). In the future, the temperature of the transition could be raised (possibly even above room temperature) or decreased in accordance with the specific demands of an application by doping the α-NiS with other metals like iron or cobalt, respectively.[26]

■ ASSOCIATED CONTENT

Ⓢ Supporting Information

The Supporting Information is available free of charge at https://pubs.acs.org/doi/10.1021/acs.jpcc.1c08412.

> TEM analysis and UV−vis absorbance spectra of AuNCs, XRD and UV−vis analysis of Au-NiS core−shell nanoparticles, full characterization of particles obtained by upscaled syntheses, and magnetic susceptibility measurements on α-NiS and Au-NiS nanoparticles (PDF)

■ AUTHOR INFORMATION

Corresponding Author

Dirk Dorfs − *Institute of Physical Chemistry and Electrochemistry, Leibniz Universität Hannover, 30167 Hannover, Germany; Laboratory of Nano and Quantum Engineering, Leibniz Universität Hannover, 30167 Hannover, Germany; Cluster of Excellence PhoenixD (Photonics, Optics, and Engineering−Innovation Across Disciplines), Leibniz Universität Hannover, 30167 Hannover, Germany;* orcid.org/0000-0001-6175-4891; Email: dirk.dorfs@pci.uni-hannover.de

Authors

Rasmus Himstedt − *Institute of Physical Chemistry and Electrochemistry, Leibniz Universität Hannover, 30167 Hannover, Germany; Laboratory of Nano and Quantum Engineering, Leibniz Universität Hannover, 30167 Hannover, Germany;* orcid.org/0000-0003-0793-5258

Dirk Baabe − *Institut für Anorganische und Analytische Chemie, Technische Universität Braunschweig, 38106 Braunschweig, Germany*

Christoph Wesemann − *Institute of Physical Chemistry and Electrochemistry, Leibniz Universität Hannover, 30167 Hannover, Germany; Laboratory of Nano and Quantum Engineering, Leibniz Universität Hannover, 30167 Hannover, Germany;* orcid.org/0000-0003-1240-7257

Patrick Bessel − *Institute of Physical Chemistry and Electrochemistry, Leibniz Universität Hannover, 30167 Hannover, Germany; Laboratory of Nano and Quantum Engineering, Leibniz Universität Hannover, 30167 Hannover, Germany;* orcid.org/0000-0002-8658-6190

Dominik Hinrichs − *Institute of Physical Chemistry and Electrochemistry, Leibniz Universität Hannover, 30167 Hannover, Germany; Laboratory of Nano and Quantum Engineering, Leibniz Universität Hannover, 30167 Hannover, Germany*

Anja Schlosser − *Institute of Physical Chemistry and Electrochemistry, Leibniz Universität Hannover, 30167 Hannover, Germany; Laboratory of Nano and Quantum Engineering, Leibniz Universität Hannover, 30167 Hannover, Germany;* orcid.org/0000-0001-9669-8383

Nadja C. Bigall − *Institute of Physical Chemistry and Electrochemistry, Leibniz Universität Hannover, 30167 Hannover, Germany; Laboratory of Nano and Quantum Engineering, Leibniz Universität Hannover, 30167 Hannover, Germany; Cluster of Excellence PhoenixD (Photonics, Optics, and Engineering−Innovation Across Disciplines), Leibniz Universität Hannover, 30167 Hannover, Germany;* orcid.org/0000-0003-0171-1106

Complete contact information is available at:
https://pubs.acs.org/10.1021/acs.jpcc.1c08412

Notes
The authors declare no competing financial interest.

■ ACKNOWLEDGMENTS

■ REFERENCES

(1) White, R. M.; Mott, N. F. The Metal-Non-Metal Transition in Nickel Sulphide (NiS). *Philos. Mag.* **1971**, *24*, 845−856.

(2) Panda, S. K.; Dasgupta, I.; Sasıoglu, E.; Blugel, S.; Sarma, D. D. NiS - An Unusual Self-Doped, Nearly Compensated Antiferromagnetic Metal. *Sci. Rep.* **2013**, *3*, 2995.

(3) Trahan, J.; Goodrich, R. G. Heat Capacity of Hexagonal NiS: Metal-Nonmetal Transition. *Phys. Rev. B* **1972**, *6*, 199−203.

(4) Mott, N. F. *Metal-Insulator Transitions*, 2nd ed.; CRC Press: London, 1990.

(5) Himstedt, R.; Rusch, P.; Hinrichs, D.; Kodanek, T.; Lauth, J.; Kinge, S.; Siebbeles, L. D. A.; Dorfs, D. Localized Surface Plasmon Resonances of Various Nickel Sulfide Nanostructures and Au-Ni₃S₂ Core-Shell Nanoparticles. *Chem. Mater.* **2017**, *29*, 7371−7377.

(6) Okamura, H.; Naitoh, J.; Nanba, T.; Matoba, M.; Nishioka, M.; Anzai, S.; Shimoyama, I.; Fukui, K.; Miura, H.; Nakagawa, H.; et al. Optical Study of the Metal−Nonmetal Transition in NiS. *Solid State Commun.* **1999**, *112*, 91−95.

(7) Bercea, A. I.; Champeaux, C.; Constantinescu, C. D.; Dumas-Bouchiat, F. Vanadium Dioxide−Iridium Composite Development: Specific Near Infrared Surface Plasmon Resonance. *J. Compos. Sci.* **2021**, *5*, 193.

(8) Ke, Y.; Zhang, B.; Wang, T.; Zhong, Y.; Vu, T. D.; Wang, S.; Liu, Y.; Magdassi, S.; Ye, X.; Zhao, D.; et al. Manipulating Atomic Defects in Plasmonic Vanadium Dioxide for Superior Solar and Thermal Management. *Mater. Horiz.* **2021**, *8*, 1700−1710.

(9) Nishikawa, K.; Kishida, Y.; Ito, K.; Tamura, S.; Takeda, Y. Near-Infrared Localized Surface Plasmon Resonance of Self-Growing W-Doped VO₂ Nanoparticles at Room Temperature. *Appl. Phys. Lett.* **2017**, *111*, 193102.

(10) Savant, V. V.; Gopalakrishnan, J.; Patel, C. C. Studies on Some Metal Monothiobenzoates. *Inorg. Chem.* **1970**, *9*, 748−751.

(11) Tat, K. W. *Design and Characterization of Some Novel Magnetic Nanomaterials.* Ph.D. Dissertation, National University of Singapore, Singapore, 2007.

(12) Peng, S.; Lee, Y.; Wang, C.; Yin, H.; Dai, S.; Sun, S. A Facile Synthesis of Monodisperse Au Nanoparticles and Their Catalysis of CO Oxidation. *Nano Res.* **2008**, *1*, 229−234.

(13) Zhu, W.; Michalsky, R.; Metin, Ö.; Lv, H.; Guo, S.; Wright, C. J.; Sun, X.; Peterson, A. A.; Sun, S. Monodisperse Au Nanoparticles for Selective Electrocatalytic Reduction of CO₂ to CO. *J. Am. Chem. Soc.* **2013**, *135*, 16833−16836.

(14) Bain, G. A.; Berry, J. F. Diamagnetic Corrections and Pascal's Constants. *J. Chem. Educ.* **2008**, *85*, 532−536.

(15) Himstedt, R.; Hinrichs, D.; Dorfs, D. Extinction Coefficient of Plasmonic Nickel Sulfide Nanocrystals and Gold-Nickel Sulfide Core-Shell Nanoparticles. *Z. Phys. Chem.* **2018**, *233*, 3−14.

(16) Rodríguez-González, B.; Burrows, A.; Watanabe, M.; Kiely, C. J.; Liz Marzán, L. M. Multishell Bimetallic AuAg Nanoparticles: Synthesis, Structure and Optical Properties. *J. Mater. Chem.* **2005**, *15*, 1755−1759.

(17) Himstedt, R.; Hinrichs, D.; Sann, J.; Weller, A.; Steinhauser, G.; Dorfs, D. Halide Ion Influence on the Formation of Nickel Nanoparticles and Their Conversion into Hollow Nickel Phosphide and Sulphide Nanocrystals. *Nanoscale* **2019**, *11*, 15104−15111.

(18) Yeshchenko, O. A.; Bondarchuk, I. S.; Gurin, V. S.; Dmitruk, I. M.; Kotko, A. V. Temperature Dependence of the Surface Plasmon Resonance in Gold Nanoparticles. *Surf. Sci.* **2013**, *608*, 275−281.

(19) Luther, J. M.; Jain, P. K.; Ewers, T.; Alivisatos, A. P. Localized Surface Plasmon Resonances Arising from Free Carriers in Doped Quantum Dots. *Nat. Mater.* **2011**, *10*, 361−366.

(20) Sparks, J. T.; Komoto, T. Metal-to-Semiconductor Transition in Hexagonal NiS. *Rev. Mod. Phys.* **1968**, *40*, 752−754.

(21) Coey, J. M. D.; Brusetti, R.; Kallel, A.; Schweizer, J.; Fuess, H. Nickel Sulfide—an Itinerant-Electron Antiferromagnet. *Phys. Rev. Lett.* **1974**, *32*, 1257−1260.

(22) Zhang, H. T.; Wu, G.; Chen, X. H. Synthesis and Magnetic Properties of NiS₁₊ₓ Nanocrystallines. *Mater. Lett.* **2005**, *59*, 3728−3731.

(23) Barry, L.; Holmes, J. D.; Otway, D. J.; Copley, M. P.; Kazakova, O.; Morris, M. A. Unusual Magnetism in Templated NiS Nanoparticles. *J. Phys.: Condens. Matter* **2010**, *22*, 076001.

(24) Tang, C.; Zang, C.; Su, J.; Zhang, D.; Li, G.; Zhang, Y.; Yu, K. Structure and Magnetic Properties of Flower-like α-NiS Nanostructures. *Appl. Surf. Sci.* **2011**, *257*, 3388−3391.

(25) Carlin, R. L. *Magnetochemistry;* Springer Berlin Heidelberg: Berlin, Heidelberg, Germany, 1986.

(26) Nakamura, M.; Fujimori, A.; Sacchi, M.; Fuggle, J. C.; Misu, A.; Mamori, T.; Tamura, H.; Matoba, M.; Anzai, S. Metal-Nonmetal

Transition in NiS Induced by Fe and Co Substitution: X-Ray-Absorption Spectroscopic Study. *Phys. Rev. B: Condens. Matter Mater. Phys.* **1993**, *48*, 16942−16947.

Supporting Information:

Temperature-Sensitive Localized Surface Plasmon

Resonance of α-NiS Nanoparticles

Rasmus Himstedt[a,b], Dirk Baabe[c], Christoph Wesemann[a,b], Patrick Bessel[a,b], Dominik Hinrichs[a,b], Anja Schlosser[a,b], Nadja C. Bigall[a,b,d], and Dirk Dorfs[a,b,d]*

[a]R. Himstedt, C. Wesemann, P. Bessel, D. Hinrichs, A. Schlosser, N. C. Bigall, and D. Dorfs

Institute of Physical Chemistry and Electrochemistry, Leibniz Universität Hannover, Callinstraße 3A, 30167 Hannover, Germany

[b]R. Himstedt, C. Wesemann, P. Bessel, D. Hinrichs, A. Schlosser, N. C. Bigall, and D. Dorfs

Laboratory of Nano and Quantum Engineering, Leibniz Universität Hannover, Schneiderberg 39, 30167 Hannover, Germany

[c]D. Baabe

Institut für Anorganische und Analytische Chemie, Technische Universität Braunschweig, Hagenring 30, 38106 Braunschweig, Germany

[d]N. C. Bigall and D. Dorfs

Cluster of Excellence PhoenixD (Photonics, Optics, and Engineering – Innovation Across Disciplines), Leibniz Universität Hannover, 30167 Hannover, Germany

E-Mail: dirk.dorfs@pci.uni-hannover.de

S1

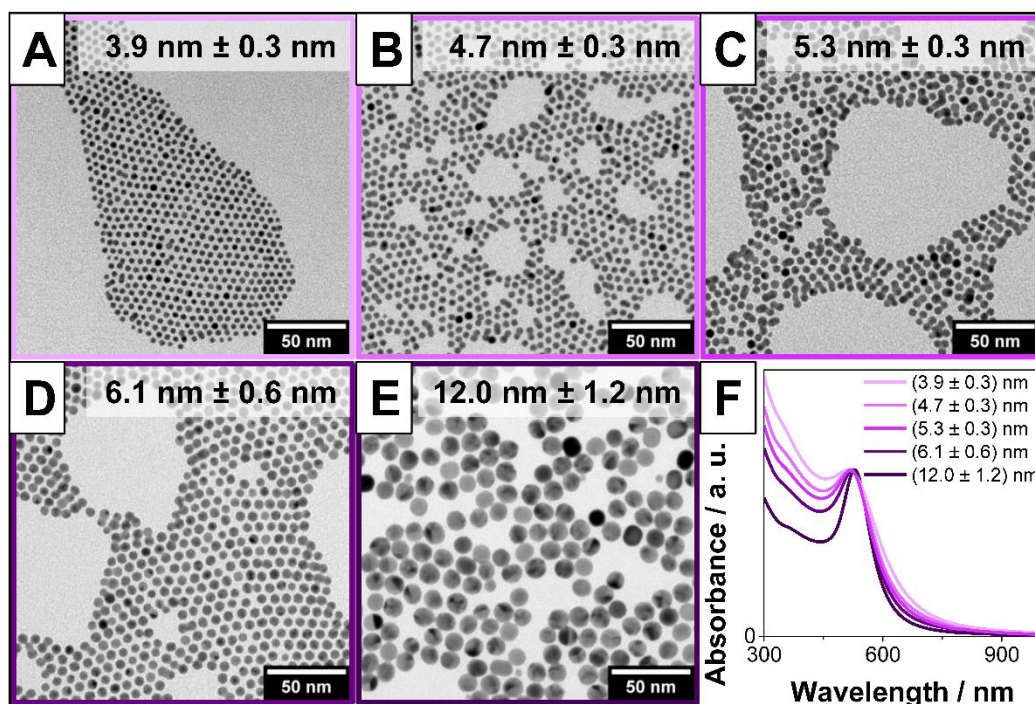**TEM analysis and UV-Vis absorbance spectra of Au nanocrystals (AuNCs)**

Figure S1. TEM overview images showing Au nanocrystals of different sizes (A-E) and the corresponding UV-Vis absorbance spectra of the same samples. The spectra have been normalized to the respective localized surface plasmon resonance (LSPR) maximum. Monodisperse particles could be obtained in all cases, while the LSPR maximum is slightly shifted towards longer wavelengths and gets sharper with an increasing diameter of the AuNCs.
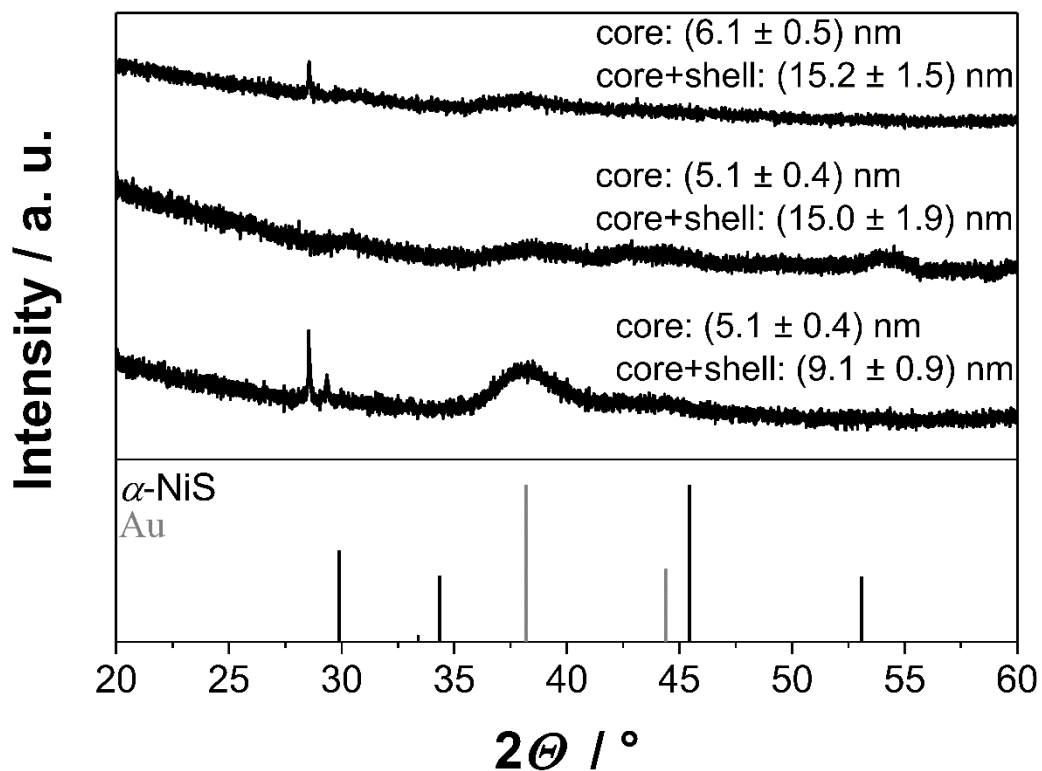
XRD analysis of Au-NiS core-shell nanoparticles

Figure S2. X-ray diffractograms of different Au-NiS samples. The α-NiS and Au references are PDF card # 03-065-0395 and 03-065-2870, respectively. The obtained reflections are significantly broadened due to the small size of the crystallites. The small and rather sharp reflections visible below 30° (2θ) are due to a slight contamination of the measurement device and are not caused by the sample.

S3

119

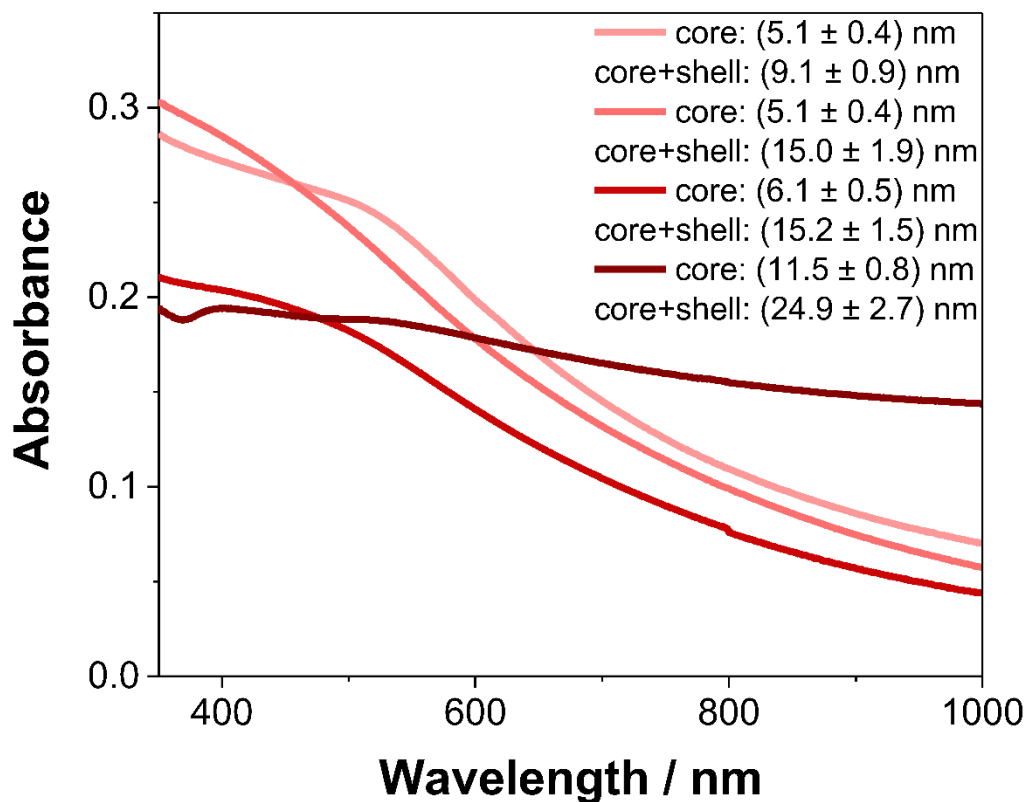**Optical analysis of Au-NiS core-shell nanoparticles**

Figure S3. UV-Vis absorbance spectra of the different Au-NiS samples. Compared to the spectra of the core particles in Figure S1 the LSPR maximum of the core-shell nanoparticles is hypsochromically shifted towards the LSPR position of pure α-NiS particles (see Figure 3 in the main text) and also broadened significantly due to the stronger damping in the nickel sulfide. The hypsochromic shift is smaller when a thinner shell is grown onto the same cores, which is in line with expectations. The largest investigated core-shell particles show a very broad absorbance, which next to increased scattering is at least in part due to an imperfect colloidal stability of this specific sample. In this case, the very broad spectrum is therefore probably caused by significant aggregation of the large particles in the dispersion.

Full characterization of particles obtained by upscaled syntheses

To obtain enough material for the magnetic susceptibility measurements, the usual synthesis process had to be scaled up seven and ten times for the α-NiS and Au-NiS synthesis, respectively. While the core-shell particles are very similar to the result of the normally scaled synthesis in size and size distribution, the pure α-NiS nanoparticles are slightly larger, less spherical, and more polydisperse (Figure S4 A&C). They are however of the correct NiS phase as can be seen in the XRD pattern (Figure S4 D, the α-NiS and Au references are PDF card # 03-065-0395 and 03-065-2870, respectively). In the case of the core-shell particles, there are, as usual, only very broad and small reflections visible (see Figure S2). The UV-Vis spectra (Figure S4 C) show an LSPR maximum slightly below 500 nm for both particle samples instead of a shoulder at shorter wavelengths as is usually the case (see Figure 3 in the main text). This is most likely caused by aggregation since the particles obtained in the upscaled syntheses are much more concentrated and less colloidally stable in their stock solutions. The very broad absorbance of the α-NiS sample is also in accord with this conclusion since the absorbance at longer wavelengths is probably caused by light scattering processes. Another factor contributing to this could be longitudinal LSPR modes from the strongly elongated particles in the sample visible in the TEM image.
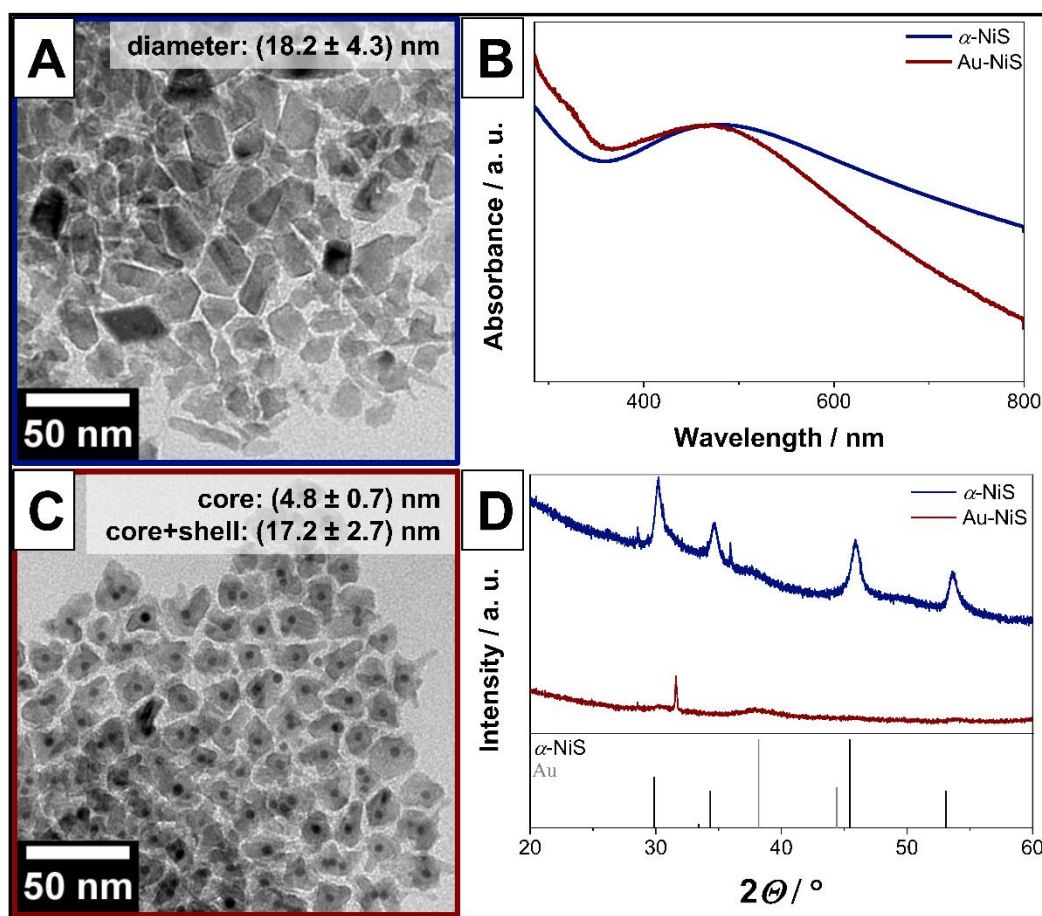
Figure S4. TEM overview images (A&C), UV-Vis absorbance spectra (B), and X-ray diffractograms (D) of α-NiS (blue) and Au-NiS (red) nanoparticles synthesized for the magnetic susceptibility measurements.
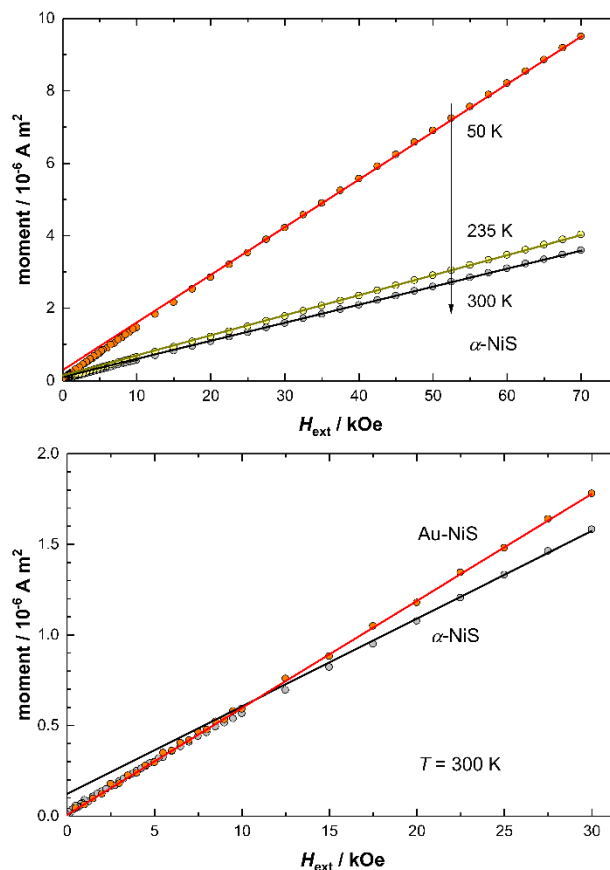
Magnetic susceptibility measurements on α-NiS and Au-NiS nanoparticles

Figure S5. (Upper panel:) Isothermal magnetization (*i.e.*, the total magnetic moment of the sample after correction of the diamagnetic contribution of the sample holder) of α-NiS nanoparticles recorded with external magnetic fields between $H_{ext} = 0$ and 70 kOe at $T = 50$, 235 and 300 K. The solid lines are to guide the eye. **(Lower panel:)** Isothermal magnetization (*vide supra*) of α-NiS and Au-NiS particles recorded with external magnetic fields between $H_{ext} = 0$ and 70 kOe, where only the data points with $H_{ext} < 30$ kOe are shown to emphasize the low magnetic field region and to support the discussion in the main text (regarding a possible ferromagnetic impurity in our α-NiS sample). The α-NiS data shown here are the same data points that are also shown in the upper panel of this figure. The solid lines are to guide the eye.
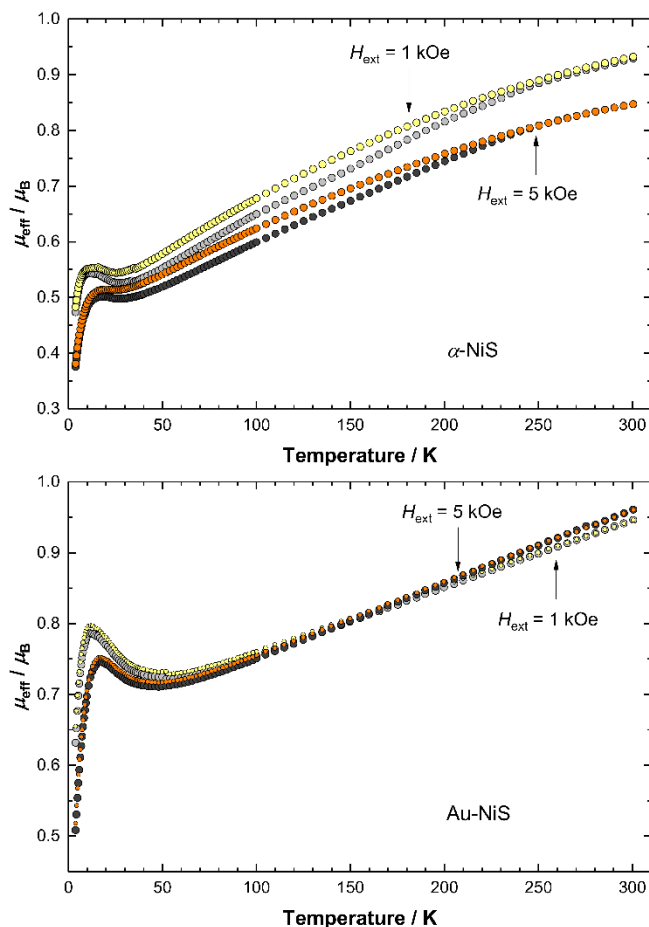
Figure S6. (Upper panel:) Effective magnetic moment (per Ni atom) versus temperature of α-NiS nanoparticles recorded between $T = 4$ and 300 K with external magnetic fields of $H_{ext} = 1$ and 5 kOe. The measurements were conducted with a field warming sequence after field cooling (yellow and orange symbols) or zero-field cooling (gray and dark gray symbols), respectively. **(Lower panel:)** Effective magnetic moment (per Ni atom) versus temperature of Au-NiS particles recorded between $T = 4$ and 300 K with external magnetic fields of $H_{ext} = 1$ and 5 kOe. The measurements were conducted with a field warming sequence after field cooling (yellow and orange symbols) or zero-field cooling (gray and dark gray symbols), respectively.
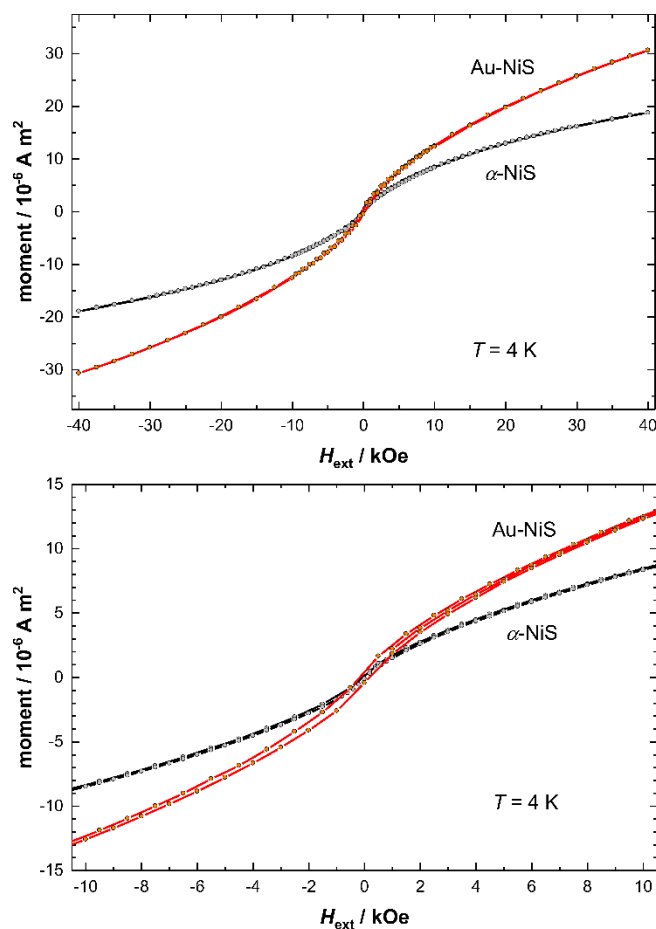
Figure S7. (Upper panel:) Isothermal magnetization (*i.e.*, the total magnetic moment of the sample after correction of the diamagnetic contribution of the sample holder) of α-NiS and Au-NiS nanoparticles recorded with external magnetic fields between H_{ext} = -40 and 40 kOe (5 section loop) at T = 4 K. The solid lines are to guide the eye. (**Lower panel:**) The same data as shown in the upper panel of this figure, where only the data points with H_{ext} > -10 kOe and H_{ext} < 10 kOe are shown to emphasize the low magnetic field region and to support the discussion in the main text (regarding the presence of a magnetic field hysteresis in the Au-NiS sample). The solid lines are to guide the eye.

5 Conclusion

5.1 Summary

One of the main goals of this thesis was to investigate the optical properties of colloidal, metallic nickel sulfide nanostructures and to examine if they could be a potential alternative to the widely used plasmonic noble metal nanoparticles. Absorbance spectra of prismatic Ni_3S_4 nanorods and novel Ni_3S_2, as well as Au-Ni_3S_2 core-shell nanostructures, which were synthesized for the first time, were therefore collected. In all cases, absorbance bands, located in the visible regime of the electromagnetic spectrum, could be found. According to the results of several different experiments, these can indeed be attributed to an LSPR.

To be able to directly compare the absorbance properties of the nickel sulfide particles to those of noble metal nanocrystals, molar extinction coefficients of Ni_3S_2, Au, and Au-Ni_3S_2 nanoparticles with equivalent diameters were determined using the same technique. It was found that the extinction coefficient of the nickel sulfide plasmon at the LSPR maximum wavelength is about 0.5 times as large as the one of Au nanocrystals. However, due to the much larger plasmon damping in the Ni_3S_2 material, its respective absorbance band is much broader than the comparably sharp Au band. Hence, when comparing the total amount of absorbed light in the visible part of the electromagnetic spectrum the nickel sulfide material could offer a more similar value. Yet, a direct comparison is difficult due to inter-band transitions occurring in the Au nanocrystals that result in significant additional absorbance in the respective spectrum. Additionally, the cost of the precursors used in the Ni_3S_2 synthesis is much lower. In order to synthesize the same number of particles of an identical diameter, the gold

precursor is about 47 times more expensive than the nickel and sulfur precursors combined.[1] Consequently, plasmonic nickel sulfide nanoparticles could be a much cheaper alternative to Au nanocrystals.

For specific uses like sensory applications, it is also useful to be able to control the shape and geometry of the nanoparticles. In addition to the previously investigated nanorods, hollow nanoparticles should therefore be synthesized because of their more sensitive reaction to changes to their dielectric surroundings. This could be achieved by fine-tuning a known Ni nanoparticle synthesis with different amounts of halide ions, which were added to the reaction solution. Depending on the used sulfur precursor, fully crystalline Ni nanoparticles could then be converted to hollow Ni_3S_2 or Ni_3S_4 particles *via* the nanoscale Kirkendall effect. These hollow particles showed a much sharper LSPR band than their conventionally synthesized counterparts. For applications as plasmonic sensors, this band sharpening leads to a direct increase in sensitivity.

Finally, the Ni-S system offers special material properties which can be examined in combination with the LSPR. α-NiS nanoparticles and Au-α-NiS core-shell particles were synthesized and investigated using temperature-dependent optical spectroscopy. A strongly temperature-dependent absorbance behavior of the colloidally dispersed particles caused by a reversible metal-insulator type phase transition was revealed. Hence, these α-NiS nanoparticles represent the first temperature-switchable plasmonic material active in the visible regime of the electromagnetic spectrum. Exploring this further could be interesting for various applications.

---

[1] Calculated using the prices for $HAuCl_4\cdot3H_2O$ (>99.99% purity), $NiCl_2\cdot6H_2O$ (>99.9% purity) and 1-dodecanethiol (>98% purity) at http://www.sigmaaldrich.com looking at quantities of 5 g (762.00 €), 5 g (30.70 €), and 500 mL (51.10 €), respectively. Visited on the 26.11.2021.

5.2 Outlook

Based on the discoveries presented in this thesis, metallic nickel sulfide nanomaterials could be implemented in applications and devices where plasmonic noble metal nanoparticles are used. Examples of this are sensorics, plasmon-enhanced fluorescence, and, to name a more specific example, surface-enhanced Raman spectroscopy (SERS). This should be done in order to examine if this new material class suffers from drawbacks that are unknown at this point or if it is able to act as a cheaper substitute for the commonly used and more expensive noble metal particles.

To further improve the suitability of the nickel sulfide for specific applications, the presented syntheses should be improved and adapted further in order to gain a wider spectrum of obtainable particle sizes. This is necessary because many applications favor larger particles than those discussed in this thesis. Additionally, nanoparticles of different metallic nickel sulfide phases such as β-NiS could be synthesized and investigated.

Regarding the study on hollow nanoparticles shown in chapter 3, it could also be worthwhile to examine the optical properties of the presented nickel phosphide particles in more detail. As shown in the supporting information of the paper, they exhibit absorbance bands in the visible regime of the electromagnetic spectrum which could also be caused by an LSPR.

The α-NiS synthesis should be adapted or a new experimental procedure needs to be found which permits the doping of the material with other transition metals like cobalt or iron. A possible alternative route to achieve this could be cation exchange reactions. Through the doping, the transition temperature of the nanoparticles could be finetuned and switching temperatures at or above room temperature should be possible making

the system even more interesting for potential applications since optical spectroscopy at temperatures below 0 °C is a very tenuous process. Alternatively, the $NiS_{2-x}Se_x$ system could be investigated since the temperature of the respective metal-insulator transition can also be tuned *via* the composition of the material.

6 Appendix

6.1 Curriculum Vitae

Personal Details:

Name:	Rasmus Himstedt
Date of Birth:	27.08.1989
Place of Birth:	Bremen

Education:

2016-present:	**Ph.D.** Candidate
	Leibniz Universität Hannover
2016:	**M.Sc.** in Materials Chemistry and Nanochemistry
	Leibniz Universität Hannover
2014:	**B.Sc.** in Chemistry
	Leibniz Universität Hannover
2008:	**Abitur**
	Kooperative Gesamtschule Leeste

6.2 List of Publications

Publications included in this thesis:

1. <u>R. Himstedt</u>, P. Rusch, D. Hinrichs, T. Kodanek, J. Lauth, S. Kinge, L. D. A. Siebbeles, and D. Dorfs, Localized Surface Plasmon Resonances of Various Nickel Sulfide Nanostructures and Au-Ni_3S_2 Core-Shell Nanoparticles, *Chemistry of Materials* **2017**, *29*, 7371-7377.

2. <u>R. Himstedt</u>, D. Hinrichs, and D. Dorfs, Extinction Coefficient of Plasmonic Nickel Sulfide Nanocrystals and Gold-Nickel Sulfide Core-Shell Nanoparticles, *Zeitschrift für Physikalische Chemie* **2018**, *233*, 1, 3-14.

3. <u>R. Himstedt</u>, D. Hinrichs, J. Sann, A. Weller, G. Steinhauser, and D. Dorfs, Halide Ion Influence on the Formation of Nickel Nanoparticles and their Conversion into Hollow Nickel Phosphide and Sulphide Nanocrystals, *Nanoscale* **2019**, *11*, 15104-15111.

4. <u>R. Himstedt</u>, D. Baabe, C. Wesemann, P. Bessel, D. Hinrichs, A. Schlosser, N. C. Bigall, and D. Dorfs, Temperature-Sensitive Localized Surface Plasmon Resonance of α-NiS Nanoparticles, *Journal of Physical Chemistry C* **2021**, *125*, 48, 26635-26644.

Publications not included in this thesis:

1. I. Strauss, A. Mundstock, D. Hinrichs, <u>R. Himstedt</u>, A. Knebel, C. Reinhardt, D. Dorfs, and J. Caro, The Interaction of Guest Molecules with Co-MOF-74: A Vis/NIR and Raman Approach, *Angewandte Chemie International Edition* **2018**, *57*, 7434.

2. D. Hinrichs, <u>R. Himstedt</u>, and D. Dorfs, The Size-Selective Interaction of Key and Lock Nanocrystals Driven by Depletion Attraction at the Nanoscale, *Nanoscale* **2018**, *10*, 9899.

3. F. Lübkemann, T. C. Gusenburger, D. Hinrichs, <u>R. Himstedt</u>, D. Dorfs, and N. C. Bigall, Synthesis of InP/ZnS Nanocrystals and Phase Transfer by Hydrolysis of Ester, *Zeitschrift für Physikalische Chemie*, **2018**, *233*, 1, 55-67.